CONTROL OF TURBINE-BASED ENERGY CONVERSION SYSTEMS

Marios Michas

School of Engineering

Cardiff University, Wales, UK

A thesis submitted for the degree of

Doctor of Philosophy

Cardiff, 2018

To my family

DECLARATION

This work has not been submitted in substance for any other degree or award at this or any other university or place of learning, nor is being submitted concurrently in candidature for any degree or other award.

Signed ……(candidate) Date……...……

STATEMENT 1

This thesis is being submitted in partial fulfillment of the requirements for the degree of ……(insert MCh, MD, MPhil, PhD etc, as appropriate).

Signed ……(candidate) Date……...……

STATEMENT 2

This thesis is the result of my own independent work/investigation, except where otherwise stated, and the thesis has not been edited by a third party beyond what is permitted by Cardiff University's Policy on the Use of Third Party Editors by Research Degree Students. Other sources are acknowledged by explicit references. The views expressed are my own.

Signed ……(candidate) Date……...……

STATEMENT 3

I hereby give consent for my thesis, if accepted, to be available online in the University's Open Access repository and for inter-library loan, and for the title and summary to be made available to outside organisations.

Signed ……(candidate) Date……...……

Contents

Acknowledgments

First and foremost, I would like to express my sincere gratitude to both my supervisors Dr Carlos E. Ugalde-Loo and Prof Nick Jenkins for their continuous advice, support and guidance during every step of my PhD.

I would like to thank Dr Wenlong Ming for his considerable help and for sharing his passion for power electronics with me. Many thanks also go to Mr Stefan Runge and Prof Thorsten Stoesser for the great collaboration and the fruitful discussions.

I would like to acknowledge the support of the CIREGS team at Cardiff University and especially the Power Electronics and HVDC group for all the helpful contributions to my work.

Special thanks go to my dear friend and colleague Dr Babis Marmaras for his help, support and encouragement especially during the first period of my PhD. My thanks are extended to all my friends for always being there for me.

Most importantly, I would like to acknowledge the support of my family all these years. My uncle Dimitris and my aunt Anastasia have always supported and encouraged me. My parents and my sister been an undying source of love, concern, support and strength. Their unfailing support and continuous encouragement made this accomplishment possible.

Abstract

This thesis investigated the modelling and control of wind and hydrokinetic turbine-based energy conversion systems. Wind turbines are a mature technology and the technical challenges are associated with their connection to the grid. However, hydrokinetic energy conversion systems are fairly new and their design is usually based on knowledge transferred from the wind industry.

Variable-speed wind turbines are either fully or partially decoupled from the frequency of the grid. Therefore, as conventional plants are decommissioned, wind turbines have to comply with requirements issued by the transmission system operator of each country. To investigate this, vector control schemes of a doubly fed induction generator (DFIG) and of a fully rated converter (FRC)-based wind turbine were modelled using MATLAB/Simulink. Simulations showed that in case of a fault at the point of connection to the grid there is a larger impact on the torque of a DFIG than a FRC-based wind turbine. In addition, the FRC-based wind turbines can increase their output to contribute to the restoration of the grid frequency.

Technical knowledge from the design, control and the modelling of variable-speed wind turbines was used for the design of an electrical subsystem for a hydrokinetic energy conversion system for man-made waterways. An FRC-based configuration based on a dc-dc converter was used for the control of the laboratory prototype of a hydrokinetic energy conversion system and the derivation of its characteristic power curves. Very high efficiencies of the system were observed due to the restricted flow conditions.

Similarly to wind turbines, the variable-speed operation of the hydrokinetic energy conversion system enabled its maximum power point tracking (MPPT). A gradient-based method was analysed and a ‘perturb and observe’ algorithm-based control scheme was used for the maximum power extraction. The technical challenges are associated with the selection of the sampling time of the algorithm according to the inertia of the system and the convergence speed coefficient according to the voltage constant of the generator. The laboratory prototype and the projected full-scale system were modelled and simulated. Simulation and experimental results show good agreement on achieving the MPPT of the hydrokinetic energy conversion system. These findings are very important for the future design of heuristic MPPT control schemes for hydrokinetic energy conversion systems.

Abbreviations

DFIG	Doubly fed induction generator
DSP	Digital signal processing
FFT	Fast Fourier transformation
FRC	Fully rated converter
FSIG	Fixed speed induction generator
HSS	High-speed shaft
IGBT	Insulated-gate bipolar transistors
LSS	Low-speed shaft
MOSFET	Metal–oxide–semiconductor field–effect transistor
MPP	Maximum power point
MPPT	Maximum power point tracking
OWF	Offshore wind farms
P&O	Perturb and observe
PI	Proportional–integral
PLL	Phase locked loop
PMSG	Permanent magnet synchronous generator
PWM	Pulse width modulation
TSO	Transmission system operator
VSC	Voltage source converter

List of Symbols

C_P	Power coefficient
λ	Tip speed ratio
β	Pitch angle
ρ	Air/water density
A	Cross-sectional area of the turbine
R	Radius of the turbine
N	Gearing ratio
τ_{aero}	Aerodynamic torque developed by the wind turbine
ω_{rot}	Rotational speed of the wind turbine
P_t	Power captured by a turbine
P_{fl}	Power available in the wind/water
i_d	Actual *d*-axis current
i_q	Actual *q*-axis current
i_q^*	Reference *q*-axis current
i_d^*	Reference *d*-axis current
λ_m	Magnetic flux of a permanent magnet synchronous generator
τ_{em}	Electromagnetic torque (PMSG)
v_d	Actual *d*-axis voltage
v_q	Actual *q*-axis voltage
v_d^*	Reference *d*-axis voltage
v_q^*	Reference *q*-axis voltage
L_d	*d*-axis self-inductance of the stator (PMSG)
L_q	*q*-axis self-inductance of the stator (PMSG)
θ_r	Rotor angle
θ_e	Electrical angle
V_{dc}^*	Reference dc (rectifier) voltage
V_{dc}	Actual dc (rectifier) voltage
f	Frequency of the grid
s	Slip (DFIG)

v_s	Actual stator voltage (DFIG)
v_s^*	Reference stator voltage (DFIG)
v_r	Rotor voltage (DFIG)
ψ_r	Rotor flux linkage (DFIG)
ψ_s	Stator flux linkage (DFIG)
L_m	Mutual inductance between stator and rotor windings (DFIG)
L_{ls}	Stator leakage reactance (DFIG)
L_{lr}	Rotor leakage reactance (DFIG)
ω_s	Synchronous speed
ω_b	Base speed
T_e	Electromagnetic torque (DFIG)
V_b	Voltage of the batteries
P	Active power
Q	Reactive power
I_{dc}	Current flowing from the rectifier to the dc-dc converter
I_b	Current flowing into the batteries
V_b	Voltage of the batteries
D	Duty cycle of the dc-dc converter
T_s	Sampling time of the MPPT algorithm
S	Convergence speed coefficient
T	Time constant
ω_{csh}	Rotational speed of the common shaft of the hydrokinetic energy conversion system
ω_t	Rotational speed of one turbine of the hydrokinetic energy conversion system
V_{fl}	Water speed
ω_e	Electrical frequency of the PMSG of the hydrokinetic energy conversion system
T_{hyd}	Hydrodynamic torque developed by the hydrokinetic energy conversion system
p	Number of pole pairs
J_{total}	Total inertia of the hydrokinetic energy conversion system
J_{2t}	The inertias of the two turbines of the hydrokinetic energy conversion system
J_{gen}	Inertia of the generator

List of Figures

List of Tables

Chapter 1
Introduction

1.1 Background

Renewable energy technologies have been deployed over the recent years to meet a considerable share of the total demand of electricity. The incentive to shift towards these technologies is the reduction of the environmental impact conventional plants have, such as the global warming [1]. Figure 1.1 shows the power generation by technology according to the New Policies Scenario of the World Energy Outlook issued by the International Energy Agency[2]. Based on this scenario, of electricity generation will increase significantly over the next twenty years with a restricted commissioning of conventional plants. The surplus electricity will be generated mainly by hydro, wind, solar and new renewable technologies.

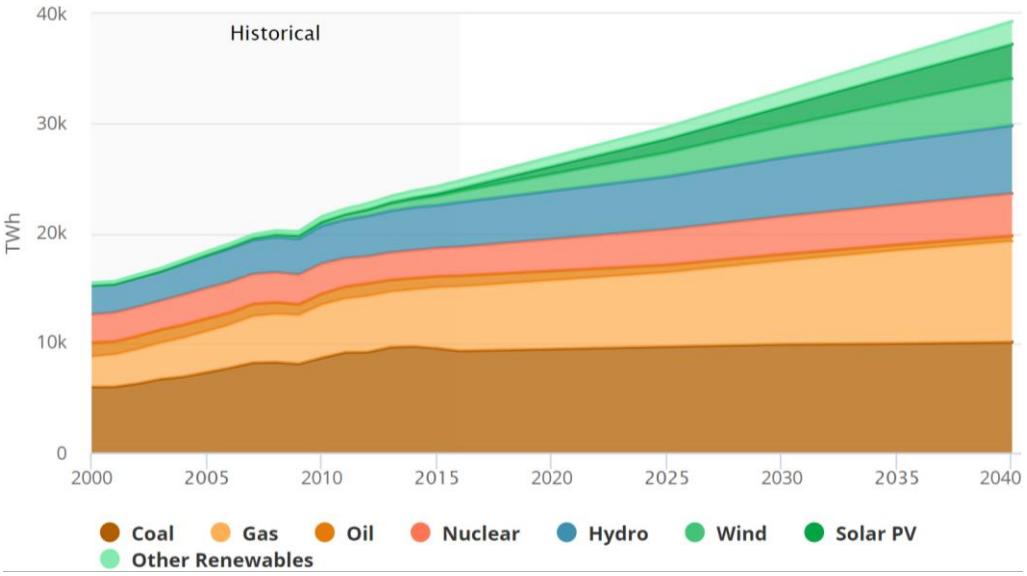

Figure 1.1. Power generation by technology according to New Policies Scenario (NPS) [2].

Wind turbines are already a mature technology and the dominant type of turbine-based energy conversion systems in the energy market. During the last three decades, the size of wind turbines has increased significantly, as shown in Figure 1.2. The first wind turbines were rated at a few kW. Since then, the diameter and hub dimensions increased to capture larger amounts of power from the wind. At present, the largest

installed wind turbines are rated at 8 MW with the latest developed wind turbine rated at 12MW [3].

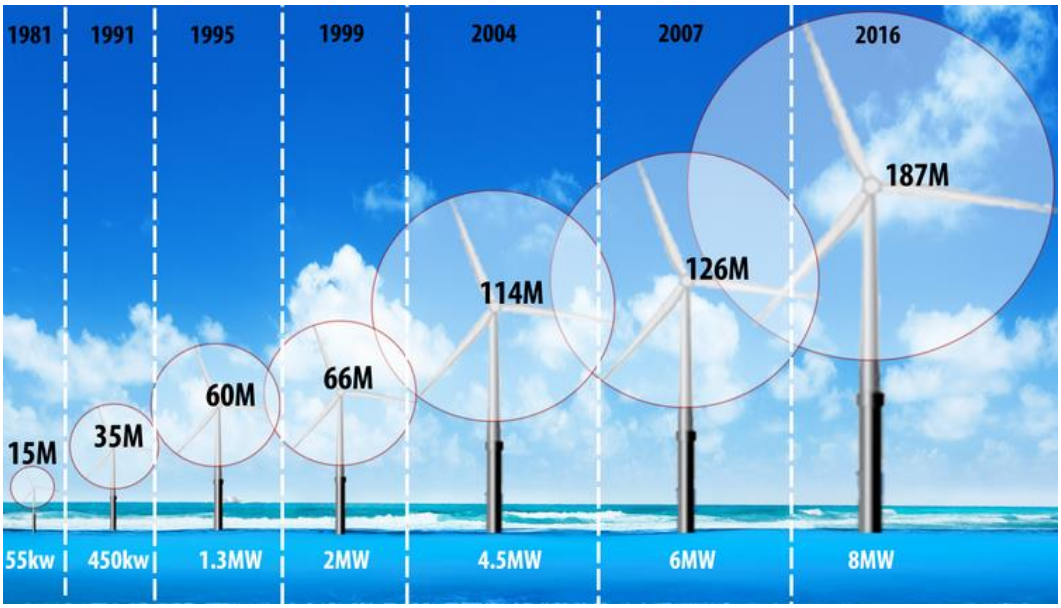

Figure 1.2. Size evolution of wind turbines [4].

As the size of wind turbines increased, the development of power electronics enabled a variable-speed operation. Various designs and control strategies have been employed depending on the generator type. This way, the power extraction below rated speed was increased.

Nowadays, large onshore and offshore wind farms are connected to the electricity grids and the advancements in the wind industry are mainly focused on the increase of the size of the turbines so that the cost of energy is reduced. A percentage of the total electricity demand is met by wind turbines instead of conventional fossil fuel plants. The main challenge now is in the design and the control of the wind turbines in order to comply with the requirements of the transmission system operator of each country.

Apart from wind, turbine-based energy conversion systems are used or considered for capturing the energy available in tidal currents, river streams or other man-made waterways. Although conventional hydroelectric plants require an artificial water-head for their operation, hydrokinetic energy conversion systems capture the power available in free flowing water streams [5]. Several tidal projects are under development around the world and in the UK, such as the SeaGen turbine [6]. On the

contrary, turbines considered for river stream and man-made waterways are still in a premature stage.

A promising technology for harvesting the energy available in the water flowing into canals is developed by Emrgy, in Atlanta, USA. Instead of using the gravity drop and head pressure like conventional hydroplants do, this hydrokinetic energy conversion system captures the kinetic energy of the water flowing in a canal. The main principle of this incentive is to generate electricity using a predictable untapped resource of power and either feed it to the grid or use it to meet the local power demand. Currently, ten turbines have been installed in a 9-mile-long canal in Colorado. Once the research stage is completed, there are prospects for expanding this technology to a water collection, treatment and distribution system [7]. As there are thousands of miles of waterways around the world, this could potentially be a new renewable energy technology that extends the current hydroelectric capacity.

Figure 1.3 shows the hydrokinetic energy conversion system developed by Emrgy for a shallow, slow-moving waterway in Colorado. It consists of a set of two identical vertical-axis turbines driving a generator through a common shaft. The use of two turbines leads to higher efficiencies than a single turbine. A rectangular concrete structure is used to assemble the hydrokinetic energy conversion system and this makes its installation simple and effective as no changes to the existing civil structures are needed.

Figure 1.3. The hydrokinetic energy conversion system developed by Emrgy [7].

This is a new technology developed towards the generation of sustainable electricity using a continuous and reliable source of power. It is based on the first-ever use of turbines to capture the excess energy in shallow waterways. The generated electricity can be used either locally for on-site operations (pumps, back-up power) or interconnect with the grid. The hydrokinetic energy conversion system can be delivered on-site fully assembled and easily installed and removed without any permanent anchoring.

This is a fairly new technology compared to wind industry and the main difference is the installation of the turbines inside a man-made waterway. Channels like the man-made waterway shown in Figure 1.3, induce pressure within a constrained area. This way the flow velocity is increased and therefore, the flow speed around a turbine is higher compared to a free rotor. Thus, the turbines installed inside such canals can capture higher amounts of power [5].

However, the use of turbines inside man-made waterways comes with some technical challenges. The main challenge currently is the efficient control for the maximum power extraction, so that the efficiency of the system is maximised and the payback period of the installation costs is reduced. The maximum power point tracking (MPPT) becomes challenging, though, due to the fact that hydrokinetic energy turbines are located in constrained and turbulent water flows. In addition, although the use of vertical-axis turbines maximises the efficinency of the hydrokinetic energy conversion system inside the canal, it induces ripple in the generated torque. As a result, the control of the system becomes more challenging and the integration of the system to the grid poses challenges regarding the voltage stability and the power quality of the grid.

1.2 Research objectives

This thesis investigated control schemes for the Grid Code compliance of wind turbines with the GB Transmission System Operator (TSO) requirements and the MPPT of a hydrokinetic energy conversion system for man-made waterways. The main objectives of this research are to:

- Investigate the Grid Code compliance and the inertia support capabilities for current wind turbine technologies modelled using MATLAB/Simulink.

- Design the electrical subsystem of the laboratory prototype of a hydrokinetic energy conversion system and obtain the characteristic curves of the system.
- Design and experimentally validate a control scheme for the maximum power extraction from the hydrokinetic energy conversion system.
- Investigate the performance of the MPPT control scheme for the anticipated full-scale hydrokinetic energy conversion system.

1.3 Thesis outline

The thesis consists of 6 chapters.

Chapter 2 – Literature review

The current wind and hydrokinetic energy conversion systems are overviewed. Horizontal and vertical-axis turbines are reviewed and their suitability for wind and hydrokinetic energy conversion systems is discussed. The topologies and the power converters used for the variable-speed operation of the turbine-based energy conversion systems are reviewed. MPPT techniques are critically reviewed with particular focus on heuristic methods.

Chapter 3 – Modelling of grid connected renewables

Wind turbines are modelled as an example of grid connected renewables. Dynamic models and control schemes for doubly-fed induction generator (DFIG) and fully rated converter (FRC)-based wind turbines, rated at the same level, are discussed. Simulations for the below rated variable-speed operation are conducted using MATLAB/Simulink. The dynamic responses and the fault ride-through capabilities of both wind turbine technologies are assessed and compared. The inertia support capabilities of FRC-based wind turbines in the GB system are also investigated. The impact of the ratings of the converters on the inertia support capabilities is also investigated.

Chapter 4 – Control of a hydrokinetic energy conversion system

The laboratory prototype of a hydrokinetic energy conversion system is described and an electrical interface is designed. A test-rig is used for the investigation of the suitability of a dc-dc converter for control purposes. The final configuration of the laboratory prototype is used for the experimental characterisation of the system.

Chapter 5 – MPPT of the hydrokinetic energy conversion system

A heuristic method for the MPPT of the hydrokinetic energy conversion system is analysed. Experimental validation using the laboratory prototype follows. Simulations of the laboratory prototype and the anticipated full-scale system are conducted. The impact of the design parameters on the performance of the MPPT is investigated.

Chapter 6 – Conclusions and future work

This chapter concludes and summarises the thesis. Recommendations for future work are also listed.

1.4 Contributions of the research work

Through the PhD study, the contributions of this thesis are:

- Modelling a DFIG and a PMSG-based wind turbine to simulate the Grid Code compliance of these technologies. This knowledge can be transferred to new turbine-based technologies, such as the hydrokinetic energy conversion system.
- Design of the electrical interface of a hydrokinetic energy conversion system for man-made waterways based on existing technologies for the variable-speed operation of wind turbines and obtained the power curves using a laboratory prototype. It is shown that the use of two vertical-axis turbines under restricted flow conditions leads to very high efficiencies of the system and thus the profitable operation of the system.
- Analysis and experimental validation of a gradient-based method for the MPPT of the hydrokinetic energy conversion system. With the MPPT, the efficiency of the system is maximised and the payback period minimised.
- Modelling and simulation the laboratory prototype and the anticipated full-scale hydrokinetic energy conversion system to demonstrate the dependence of the MPPT method on the inertia of the system and the voltage constant of the generator. This is particularly important for the future design of similar systems of any scale.

1.5 List of publications

During the doctorate study, two documents have been written for publication. The publications are given below:

1. Marios Michas, Carlos E. Ugalde-Loo and Nick Jenkins, "Grid code compliance and ancillary services provision from DFIG and FRC-based wind turbines," *51st International Universities Power Engineering Conference (UPEC)*, Coimbra, Portugal, 6-9 September 2016, pp. 1-6.
2. Marios Michas, Carlos E. Ugalde-Loo, Wenlong Ming, Nick Jenkins and Stefan Runge, "Maximum power extraction from a hydrokinetic energy conversion system", *IET Renewable Power Generation*, 2018 (Under Review).

CHAPTER 2

LITERATURE REVIEW

2.1 Wind energy conversion systems

2.1.1 Aerodynamic energy conversion

According to actuator disc theory, the power available in the wind P_{wind} (W) is given by [8],[9]

$$P_{wind} = \frac{1}{2}\rho A V_w^3 \tag{2.1}$$

where ρ is the air density ($1.225\ \mathrm{kg/m^2}$), A is the cross-sectional area ($\mathrm{m^2}$) and V_w is the free wind speed (m/s).

The power available in the wind cannot be completely extracted by a wind turbine. The power transferred to the turbine rotor, P_t, is reduced by the power coefficient, C_P, defined by [10]

$$C_P = \frac{P_t}{P_{fl}} \tag{2.2}$$

The maximum theoretical value of C_P is 0.593. This is known as the Betz limit and it means that a turbine can never extract more than 59.3% of the power available in a free air stream. The power coefficient is a function of two variables: the pitch angle of the blade, β, (wherever applicable) and the tip speed ratio, λ. The tip speed ratio is defined by [8]

$$\lambda = \frac{\omega R}{V_w} \tag{2.3}$$

where ω is the rotational speed of the rotor (rad/s) and R is the radius of the rotor (m). Both the power coefficient and the tip speed ratio are dimensionless quantities and are used to describe the performance of turbines of any size. For a specific wind speed and a fixed pitch angle, there is only one tip speed ratio at which the maximum power coefficient occurs [11]. The variation of the power coefficient as a function of the tip speed ratio is shown in Figure 2.1.

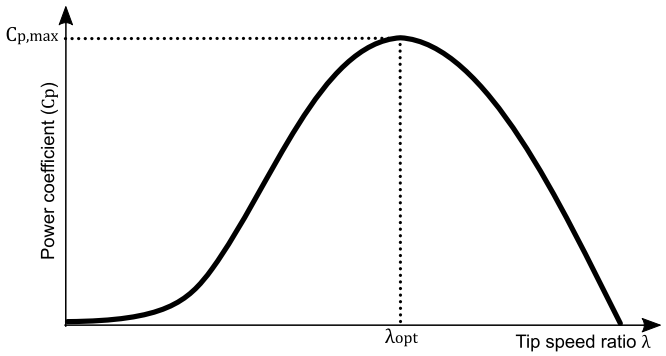

Figure 2.1. Variation of the power coefficient as a function of the tip speed ratio.

2.1.2 Horizontal-axis turbines

Horizontal-axis turbines are the dominant technology for wind turbine applications. A horizontal-axis turbine consists of a nacelle mounted on the top of a tower. The nacelle contains the rotor of the turbine, the gearbox and the generator [12].

The main variable for the design of a horizontal-axis turbine is the number of the blades. The number of the blades has an impact on the tip speed ratio and the starting torque. Wind turbines with two or three blades have a high tip speed ratio. A high tip speed ratio leads to a smaller and lighter gearbox to achieve the high speed required for the generator used. The main drawback of turbines with small number of blades is that the starting torque is low. Therefore, these turbines may need to be started using a starting motor for very low wind speeds [13].

The dominant design for grid connected wind turbines is based on a three-bladed turbine, as shown in Figure 2.2(a). Multiple bladed turbines, as shown in Figure 2.2(b), are not used widely for electricity generation; however, they are often used for mechanical water pumping [14].

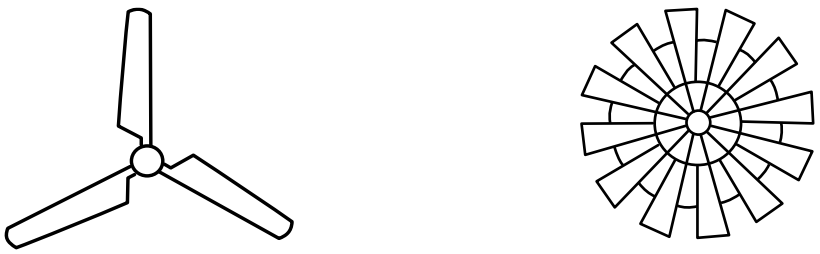

(a) (b)

Figure 2.2. Horizontal-axis turbines: (a) high speed and (b) low speed [14].

Apart from the typical designs of horizontal-axis turbines, considerable research is being done on new designs using power augmentation. However, these designs have not been employed in the wind industry due to the increased cost of the structure [15].

2.1.3 Vertical-axis turbines

Although horizontal-axis turbines are commercially prevalent in wind turbine applications, vertical-axis turbines have been developed for wind energy conversion as well. The rotational axis of the rotor of a vertical-axis turbine is vertical to the incoming wind– in contrast to the rotational axis of the rotor of a horizontal-axis turbine which is parallel to the incoming wind [16]. A nacelle is not needed and the generator size is not a basic problem.

The first vertical-axis turbine was the Savonious turbine [17]. The Darrieus turbine based on straight or bent blades followed [18]. Squirrel cage Darrieus, H-Darrieus (Figure 2.3(a)) and Gorlov helical turbines (Figure 2.3(b)) are based on the initial design of the Darrieus turbine [19].

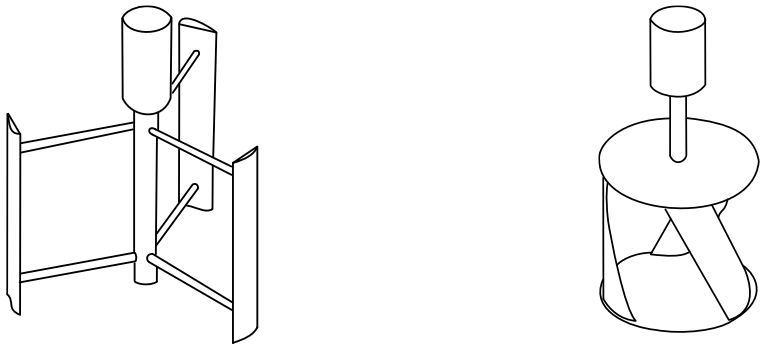

(a) (b)

Figure 2.3. Vertical-axis turbines: (a) H-Darrieus and (b) Gorlov [20].

The angle of attack between the blades and the apparent wind changes with the rotation of the turbine. This leads to the presence of an inherent torque ripple [16]. This ripple affects the mechanical components of the turbine and the quality of the output power [21]. A design with more blades and the variable-speed operation contribute to the elimination of this torque ripple [22].

Figure 2.4 shows the power coefficient C_p versus the tip speed ratio λ for different types of turbines. Although the performance of the vertical-axis turbines has been improved over the recent years, they are less efficient in average compared to their horizontal-axis counter parts. In addition, a push for their start-up is needed and, thus,

an amount of electricity is consumed. For these reasons, there has not been much interest for a large-scale production of vertical-axis turbines for wind industry. However, their shape and the simple structure (no yaw control), make them suitable for hydrokinetic energy conversion systems.

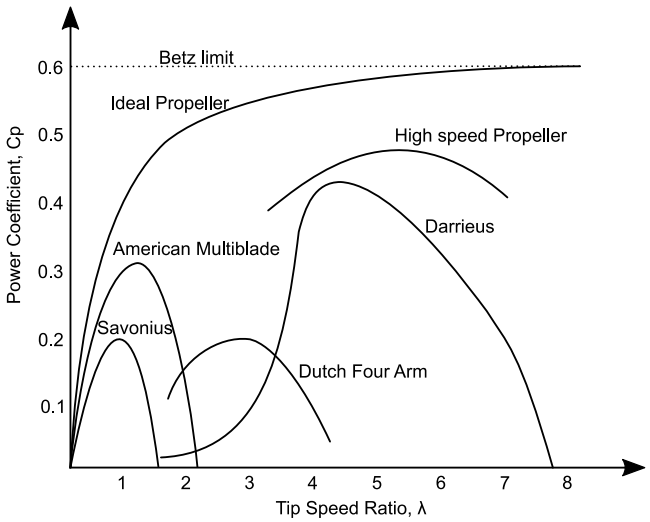

Figure 2.4. $C_p - \lambda$ curves of different turbine types [14].

2.2 Hydrokinetic energy conversion systems

Both horizontal and vertical-axis turbines have been considered for hydrokinetic energy conversion systems. Currently, such systems are used for the generation of electricity in two main areas: tidal currents and river streams [23]. Similarly to the aerodynamic energy conversion, the hydrodynamic energy conversion is described by equations (2.1)–(2.3). The difference is that the water density (997 kg/m^2) is much higher than the density of the air (1.225 x10^{-3} g/cm^3).

Horizontal-axis turbines are commonly used for tidal stream applications [24], though unconventional designs have been also considered [25]. Existing and proposed designs are based on bottom fixed or floating turbines [5] and on either fixed or variable pitch blades [26]. Industrially, a number of horizontal-axis tidal turbines have been developed [27]–[30]. These turbines are bottom mounted with power capacities up to several megawatts [31], [32].

Apart from tidal stream turbines, river stream turbines have also been considered for hydrokinetic energy conversion [33]. On a conceptual stage, both horizontal and vertical-axis turbines have been considered for this technology. Vertical-axis turbines,

though, seem to attract attention mainly due to their shape and the simplicity of the structures needed for augmentation for higher efficiencies [34].

2.3 Fixed-speed and variable-speed operation

The oldest and simplest wind turbine technology is based on fixed-speed induction generators (FSIGs). As the size of wind turbines increased, variable-speed technology was developed. This way, the maximum power extraction was enabled and new requirements for grid connection were issued in Grid Codes [12]. The most common variable-speed wind turbine configurations are the DFIG-based and the FRC-based wind turbine.

Since hydrokinetic energy conversion systems were developed – either conceptually or industrially – when the wind technology was already mature, they were mostly designed for variable-speed operation [35]. However, a fixed-speed topology has been employed in tidal applications [36].

2.3.1 Fixed-speed induction generator-based turbines

Fixed-speed wind turbines are fairly simple electrical devices. This technology is based on an induction generator driven by an aerodynamic rotor via a gearbox. The typical configuration of a FSIG-based wind turbine is shown in Figure 2.5. It consists of a squirrel-cage induction generator connected to the power system through a turbine transformer. Although the slip varies as the operating power level changes, its variation is generally less than 1-2 % and thus, this type of wind turbine is referred to as a fixed-speed [37].

Due to the fact that squirrel-cage induction machines consume reactive power, power factor correction capacitors at each wind machine are used. In addition, a soft-starter is employed so that the magnetic flux is built up slowly and the transient currents are limited [38].

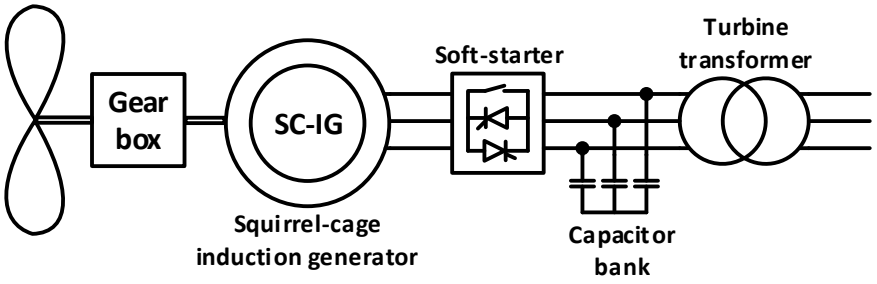

Figure 2.5. Configuration of a FSIG-based turbine [39].

2.3.2 DFIG-based turbines

A typical configuration of a DFIG-based wind turbine is shown in Figure 2.6. It includes a wound-rotor induction generator and slip rings are used to take current into or out of the rotor winding. A controllable voltage is injected into the rotor winding at slip frequency so that variable-speed operation is achieved. The rotor winding is fed through back-to-back variable frequency voltage source converters (VSCs). The power converters decouple the network electrical frequency from the rotor mechanical frequency. This way, variable-speed operation is enabled. Voltage limiters and an over-current 'crowbar' are used so that both the generator and the converters are protected [40], [41].

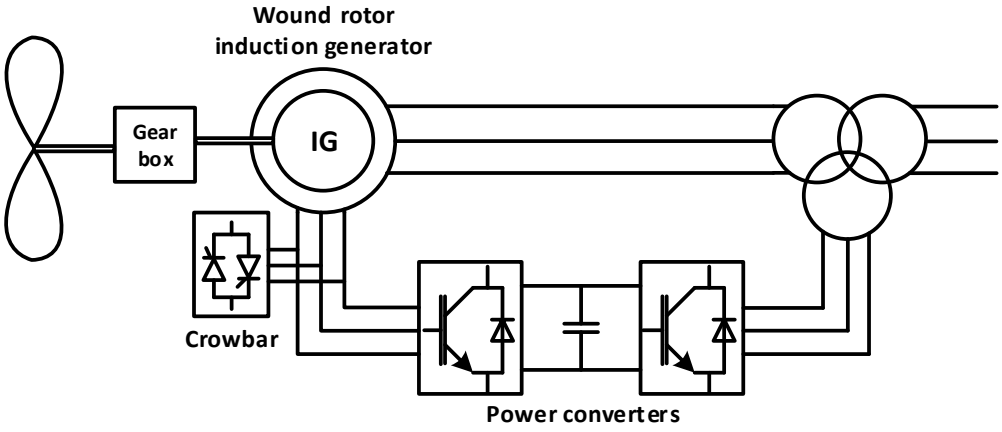

Figure 2.6. Typical configuration of a DFIG-based turbine [39].

In a DFIG-based turbine, power is delivered from the generator to the grid through both the stator and the rotor. Depending on the rotational speed of the generator, the rotor can also absorb power. If the generator operates below synchronous speed (Figure 2.7(a)), power is absorbed from the network though the converters. If the generator operates above synchronous speed (Figure 2.7(b)), power is delivered from the rotor through the converters to the grid.

(a) (b)

Figure 2.7. Sub-synchronous (a) and super-synchronous (b) operation of a DFIG [12].

DFIG-based configurations have also been considered for hydrokinetic energy conversion systems. In [42], a gearless multi-pole DFIG-based configuration was proposed for stream hydrokinetic generation. In [43], the reliability of the power converters of a DFIG-based tidal turbine is assessed. A DFIG-based river turbine systems has been considered in [44]. However, small scale DFIG-based turbine systems have not been much reported in the literature.

2.3.3 FRC-based turbines

For an FRC-based turbine, various electrical generator types can be employed, such as induction, wound-rotor synchronous or permanent magnet synchronous generator (PMSG) [45]. This type of turbine may or may not include a gearbox. Since all of the power generated by the wind turbine goes through power converters, the dynamic operation of the generator is decoupled from the power grid**.** Therefore, the electrical frequency of the generator is varied, while the grid frequency remains unchanged.

Different types of power converters are used for an FRC-based turbine. The type of power converter arrangement that is employed indicates the control strategy for the generator. The most common choice for wind turbines is back-to-back VSCs, as shown in Figure 2.8 (a). The grid-side converter is used to control the dc bus voltage in order to keep it constant, while the machine-side converter is used to control the torque that is applied to the generator. Reactive power is either generated or absorbed by each converter independently. This configuration has also been proposed for tidal energy applications as in [26], as well as for small-scale hydrokinetic energy conversion systems [46].

For an FRC configuration using a PMSG, the excitation is provided by the permanent magnets. However, in the case of a wound rotor synchronous generator, either a cylindrical or salient pole one, a diode rectifier is used for the excitation current of the rotor [47]. The configuration of the system for an electrically excited synchronous generator is shown in Figure 2.8(b).

Another arrangement of the power electronics of an FRC-based turbine is shown in Figure 2.8(c). This configuration consists of a diode-bridge rectifier, a dc-dc converter for the control of the generator and a VSC for the connection to the grid [48]. This has been proposed for both wind applications [49], [50] and small scale hydrokinetic energy conversion systems [51]. In addition, a not widely used arrangement was

reported in [52], [53], where an uncontrolled rectifier is implemented and the inverter is used for the control of the turbine.

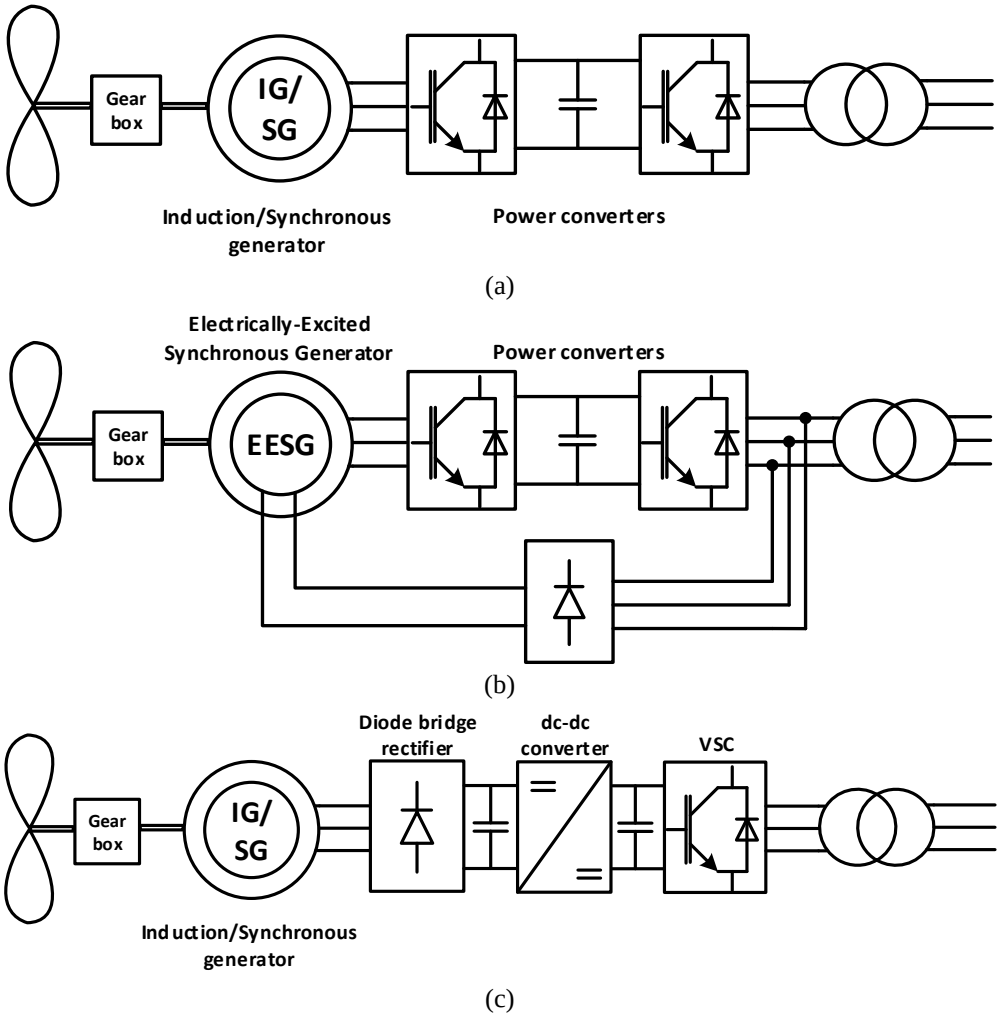

Figure 2.8. Configuration of FRC-based turbines: (a) using back to back VSCs and (b) using diode bridge rectifier and a dc-dc converter.

2.4 Power electronics for variable-speed turbines

As described in Section 2.3, power electronics are the dominant technology for the variable-speed operation of turbine-based systems. An overview of the types and the basic operation of the dc-dc converters as well as the ac-dc VSCs follows.

2.4.1 Dc-dc converters

The main topologies of dc-dc converters are the buck (step-down), the boost (step-up), the buck-boost, the Cúk and the flyback converter [54]. The dc-dc converters are useful in turbine-based energy conversion systems with uncontrolled rectifiers, as shown in Figure 2.8(c), for the control of the generator speed. The basic converter

topologies are the buck and the boost converters. The buck-boost is derived from the cascaded connection of the two basic topologies. The Cúk and the flyback topologies are based on the buck-boost converter.

Dc-dc converters are used in several applications as the output voltage is controlled while the input voltage and the load may vary. One of the methods to control the output voltage is achieved through pulse-width modulation (PWM) switching. In this method, two quantities are under consideration: the switching time period (and thus, the switching frequency) and the duty cycle *D*. The switching time period is normallykept constant, while the duty cycle is varied [55].

The switching time period is defined as [54]

$$T_{sw} = t_{on} + t_{off} \tag{2.4}$$

where t_{on} is the time the switch is on and t_{off} is the time the switch is off.

The duty cycle *D* is given by [54]

$$D = \frac{t_{on}}{T_{sw}} \tag{2.5}$$

There are two modes of the operation of dc-dc converters: the continuous current conduction and the discontinuous current conduction. During the continuous current conduction mode, the average current (inductor current of the figures of the Table 2-1) flows continuously. When the output current is below a critical value, the inductor current becomes zero for a portion of the duty cycle until the beginning of the next switching cycle. This is the discontinuous current conduction mode [56]. Details about the discontinuous conduction mode are given in [54].

Table 2-1 summarises the basic uni-directional dc-dc converters. The topologies along with the ratios between the input and the output voltages and currents for the continuous conduction mode are listed. No power losses within the converters is assumed.

Table 2-1: Basic dc-dc converter topologies [54], [57].

Dc-dc converter	Topology	V_o/V_d	I_o/I_d
Buck	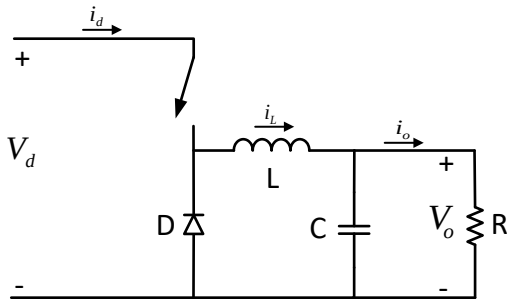	D	$\frac{1}{D}$
Boost	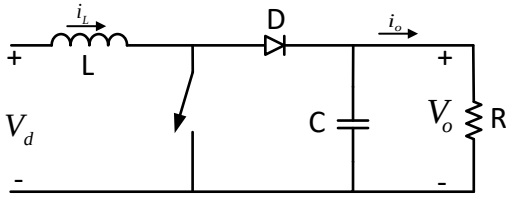	$\frac{1}{1-D}$	$1-D$
Buck-boost	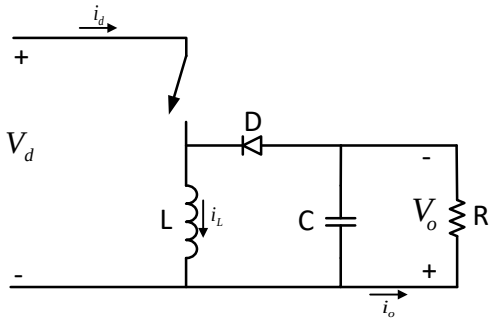	$D\frac{1}{1-D}$	$\frac{1-D}{D}$
Cúk	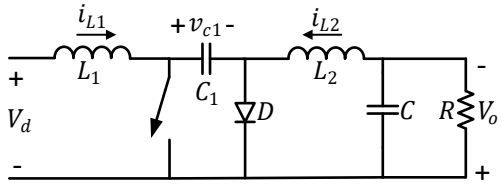	$D\frac{1}{1-D}$	$\frac{1-D}{D}$
Flyback	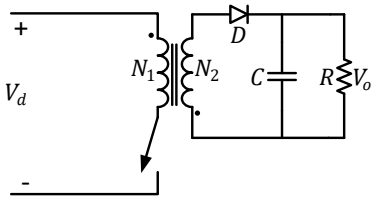	$D\frac{1}{1-D}$	$\frac{1-D}{D}$

In this chapter the buck-boost converter is examined in detail as it was adopted in this work. For a dc input voltage V_d, the buck converter produces a lower average voltage output V_o. Conversely, the output voltage V_o is always greater than the input voltage in the case of a boost converter.

As the name implies, the output voltage of a buck-boost converter is either higher or lower than the input voltage. As shown in Figure 2.9, during the interval when the switch is on, the diode is reversed-biased and the input source provides energy to the inductor. When the switch is off, the energy stored in the inductor is supplied to the output load and no energy is flowing from the input source.

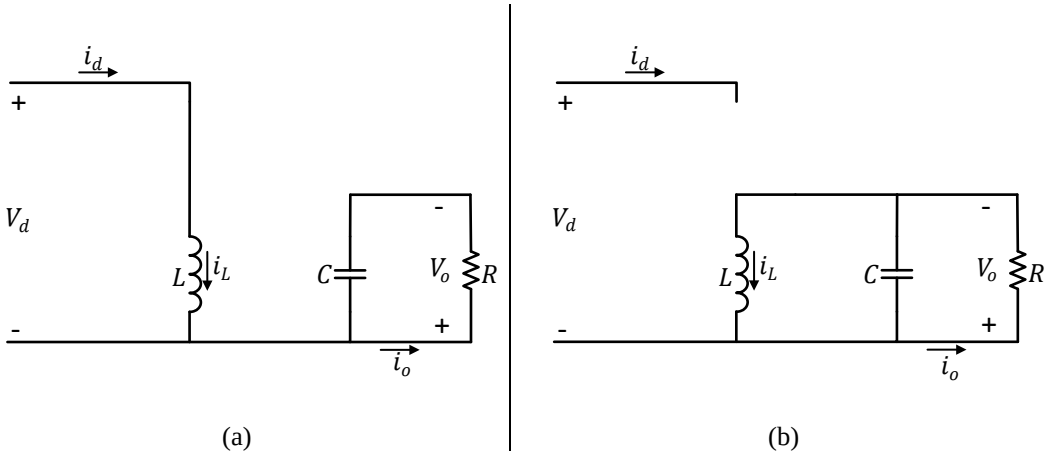

Figure 2.9. Buck-boost converter when the switch is on (a) and off (b) [54].

Figure 2.10 shows the voltage and the current waveforms of a buck-boost converter when the inductor current flows continuously. By integrating the inductor voltage over one time period

$$V_d D T_{sw} + (-V_o)(1 - D) T_{sw} = 0 \tag{2.6}$$

Thus, since $T_{sw} \neq 0$,

$$\frac{V_o}{V_d} = \frac{D}{1 - D} \tag{2.7}$$

Assuming no losses within the converter,

$$P_d = P_o \tag{2.8}$$

The ratio between the input and the output current is given by

$$\frac{I_o}{I_d} = \frac{1 - D}{D} \tag{2.9}$$

Similarly, the ratios between the input and output voltage and currents for the other dc-dc converters can be obtained and these are summarised in Table 2-1.

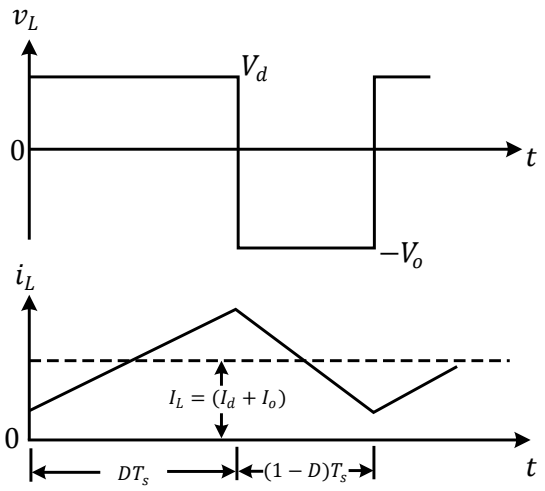

Figure 2.10. Waveforms of the voltage and the current for the continuous-conduction mode of the buck-boost converter [54].

2.4.2 Voltage source converter

The three main types of VSC topologies are the two-level, the three-level and the multilevel. The voltage level for a two-level VSC is around 2 kV and the power rating is a few MWs. The three-level VSC is rated at 4 kV and usually used in industrial plants. The multilevel VSC is rated at a few GWs and is used in a utility scale. All types of VSCs are used in HVDC systems [58], [59]. For the control of variable-speed turbines, two-level and three-level VSCs have been proposed [60]–[62]. The output voltage waveforms for the three topologies are shown in Figure 2.11.

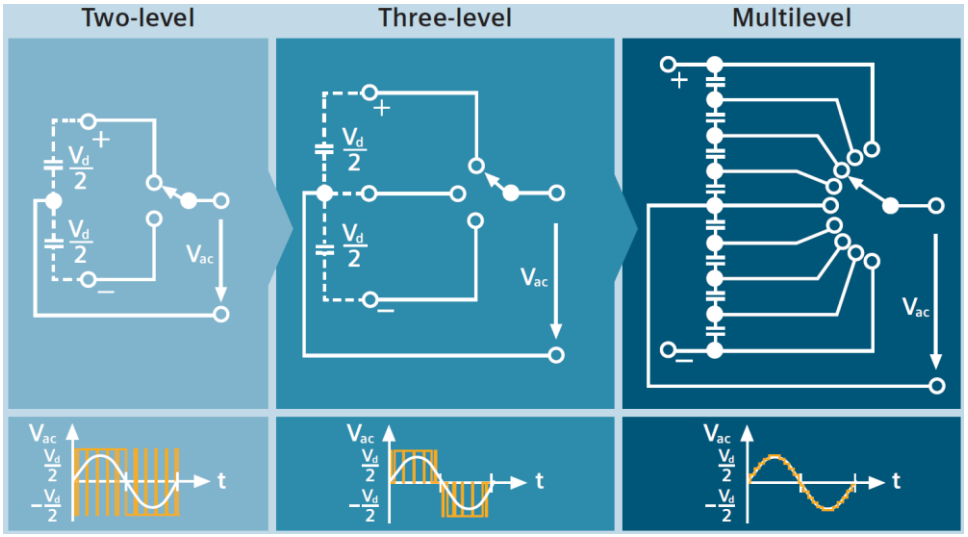

Figure 2.11. Topologies and output voltage waveforms for the two-level, the three-level and the multilevel VSCs [63].

This chapter is restricted to the analysis of two-level VSCs used for the variable-speed operation and the grid connection of wind and hydrokinetic turbines. For a two-level VSC, series connected insulated-gate bipolar transistors (IGBTs) are used in order to switch between the positive and the negative polarity of a charged dc capacitor, as shown in Figure 2.11. The IGBTs are controlled using the PWM technique. This way, the independent control of the magnitude and the phase angle of the ac output is enabled. Therefore, the active and reactive power are controlled independently.

Figure 2.12 shows the topology of one phase of a two-level VSC with the dc capacitor grounded at midpoint. The output voltage is generated using two voltage levels between the midpoint of the dc capacitor and the point 'p' shown in Figure 2.12. The switching frequency of the two-level VSC is of 1 kHz and above. Thus, high frequency harmonic components are produced and ac filters are used at the output of the VSCs. Furthermore, the dc voltage steps at the converter output are large, as shown in Figure 2.11. Special transformers are used to withstand this high voltage output stress [64].

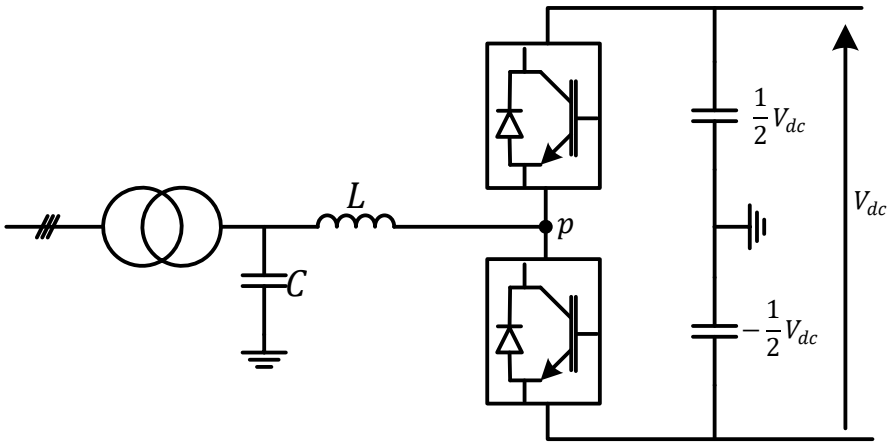

Figure 2.12. One-phase of a two-level VSC.

2.5 Maximum power extraction from variable-speed turbines

2.5.1 Operating regions of a variable-speed turbine

Figure 2.13 shows the operating regions of a turbine. It operates between the cut-in and the cut-out speed. For speeds below the cut-in speed, the available power is not enough to overcome the turbine losses. Therefore, no power is generated. For speeds between the cut-in and the rated speed, variable-speed operation of the turbine is enabled for the maximum power extraction. The last region ranges between the rated and the cut-out speed. In this region, for horizontal-axis turbines (mainly wind and

tidal), the aerodynamic/hydrodynamic power is limited by stall regulation, pitch angle control or yaw control [8], [26].

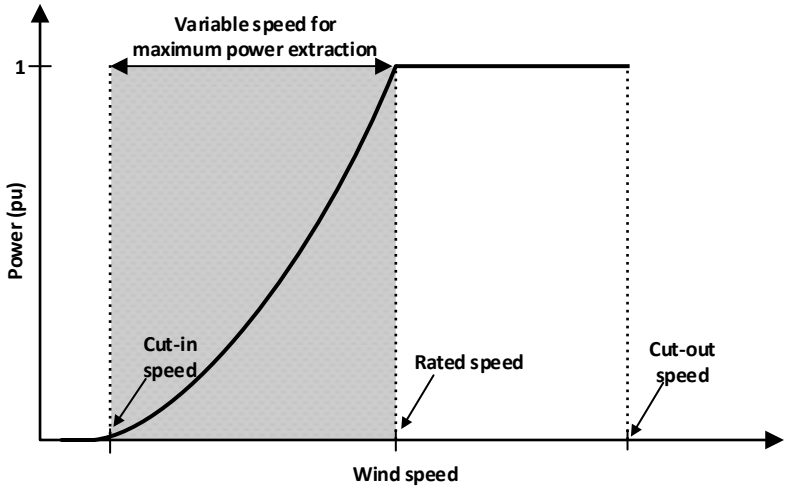

Figure 2.13. Ideal power curve of a turbine [12].

The cut-in, rated and cut-out speeds depend on the turbine design. For a wind turbine, the cut-in speed typically varies between 3 to 5 m/s, and the cut-out speed is mostly 25 m/s [12]. Unlike wind turbines, the operating regions of hydrokinetic turbines are not well defined [65]. For hydrokinetic turbines operating under unconstrained flow, the rated speed is mostly considered to be 2.5 to 3 m/s [66]. The rated water speed of a hydrokinetic turbine, though, depends on various factors such as site resources and channel augmentation [65].

2.5.2 MPPT methods

The maximum energy production depends not only on the available power from a natural source (e.g. wind, hydro), but also the operating point the energy conversion devices are working on. MPPT techniques have been developed and play a key role in the efficiency of the renewable energy technologies.

The MPPT techniques used in wind turbines are either based on a predefined trajectory obtained from the turbine characteristics or on iterative search. Turbine-based hydrokinetic energy conversion systems are based on previously developed wind turbine systems. Therefore, MPPT methods used in wind turbines have been also considered for the MPPT of hydrokinetic turbines.

Figure 2.14 shows the power-speed characteristic curve of a wind turbine for various wind speeds as well as the maximum power-speed curve. The control objective is to

keep the turbine operating on the maximum power curve under various wind conditions. For this purpose, power electronics are used in modern variable-speed wind turbines, as described in Section 2.3.

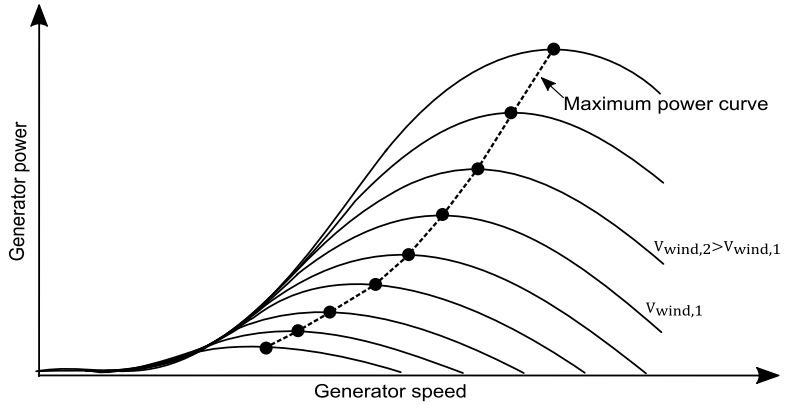

Figure 2.14. Power-speed characteristic for various wind speeds and the maximum power-speed curve [12].

Prior to the implementation of the control system, simulation or experimental results are used to obtain the optimal power characteristic curve of a wind turbine. The data are stored in a look-up table. As shown in Figure 2.15, the rotational speed of the generator is measured and used as an input to the look-up table. A reference set-point for the optimal power extraction is obtained from the look-up table and is used as a reference value for the controllers of the system [67]. An alternative way to achieve this is through the use of a polynomial equation instead of the look-up table [14].

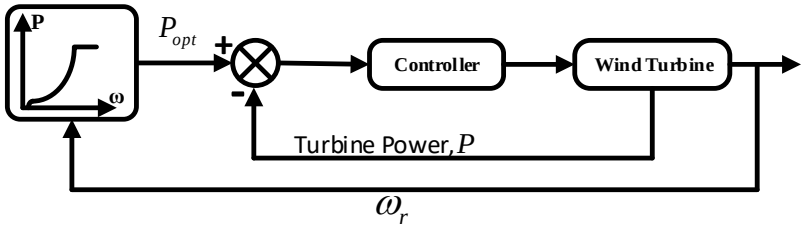

Figure 2.15. Control scheme for maximum power extraction.

According to [12], the optimal power curve is defined by

$$P_{opt} = K_{opt}\omega_r^3 \tag{2.10}$$

and the optimal torque curve is given by

$$T_{opt} = K_{opt}\omega_r^2 \tag{2.11}$$

where T_{opt} is the optimal torque of the machine, K_{opt} is a constant depending on the aerodynamic performance of the wind turbine and ω_r is the rotational speed of the generator.

Therefore, the optimal toque-speed characteristic shown in Figure 2.16 is also used in control schemes for optimum wind power extraction [68],[69]. A control scheme based on the absence of mechanical sensors is described in [70], although it is not industrially popular.

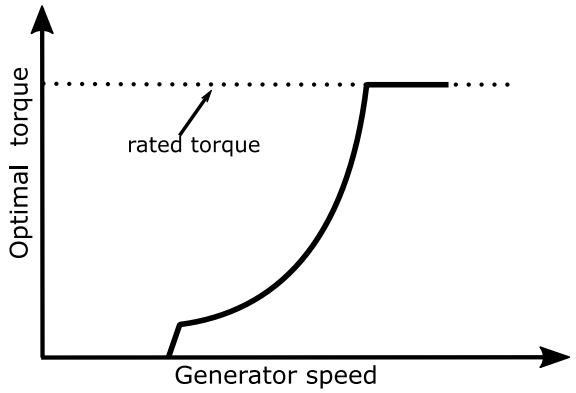

Figure 2.16. Optimal torque-speed characteristic.

Alternatively, instead of controlling the power or the torque of the generator, MPPT is achieved by controlling the tip speed ratio [71]. There is a unique optimal tip speed ratio for a specific wind turbine, regardless of the wind speed. For this control scheme, an anemometer is used to measure the wind speed. Then, a reference value for the rotational speed corresponding to the maximum power extraction is calculated, using

$$\omega_{r,opt} = \frac{\lambda_{opt} v_w}{R}, \tag{2.12}$$

where $\omega_{r,opt}$ is the rotational speed for maximum power extraction, λ_{opt} is the optimal tip speed ratio, R is the radius of the wind turbine, and v_w is the wind speed.

As in the case for power/torque control schemes, the rotational speed is measured. The difference between the measured and the reference value of the rotational speed is fed to the controllers of the system to ensure maximum power production. The control of the tip speed ratio in a marine current turbine is described in [72].

All these alternative ways to take advantage of a predefined trajectory for the MPPT of a wind turbine are based on rotational speed measurements. This poses a risk, because due to the combined inertia of the wind turbine and the generator, a rapid

change in wind speed might not have an immediate impact on the generator rotational speed.

Furthermore, the use of a look-up table is based on the assumption that constant optimal values are stored in it. In reality, there are factors that influence these values, such as the air density variation, the aging and the efficiencies of the generator and the converters [73].

Additionally, in the case of the optimal tip speed ratio control scheme, the anemometer is usually placed at the hub height (nacelle) and the wind speed measurements do not correspond to the whole projected area of the wind turbine. Therefore, the actual wind speed that the wind turbine faces is slightly different from the anemometer measurements.

Although MPPT schemes based on a predefined trajectory are widely used in the wind industry, especially in large-scale, grid-connected wind turbines [49], perturb and observe (P&O) methods are discussed in the literature for either standalone [74], or grid-connected [75] small-scale turbines. Industrially, though, P&O methods have been widely used in photovoltaic systems [76]. The main principle of this method is the perturbation of a variable and the observation of the resulting electrical power. For the implementation of the P&O algorithm, no prior knowledge of the wind turbine characteristic curve is required.

A typical P&O algorithm for the MPPT in turbines with a configuration shown in Figure 2.8(c) is shown in Figure 2.17. The control variable for this method is the rotational speed ω. A reference value for the rotational speed ω^* is set and the resulting electrical power P is measured. The principle for this method is that at the maximum power production, $\frac{dP}{d\omega} = 0$. For a specific perturbation of the rotational speed at time $t = k$, the rectifier voltage $V(k)$ and current $I(k)$ are measured and the electrical power $P(k)$ is obtained. Then, for a specific perturbation of the rotational speed $\omega(k+1)$, if the electrical power output is increased ($P(k+1) - P(k) > 0$), a step change in the control variable of the same direction takes place (if $\omega(k+1) - \omega(k) > 0$ then ω^* is set higher and if $\omega(k+1) - \omega(k) < 0$ then $\omega^*$is set lower). Otherwise ($P(k+1) - P(k) < 0$), the same step change takes place with a reversed sign (if

$\omega(k+1)-\omega(k)>0$ then ω^* is lower and if $\omega(k+1)-\omega(k)<0$ then $\omega^*$is set higher) [77].

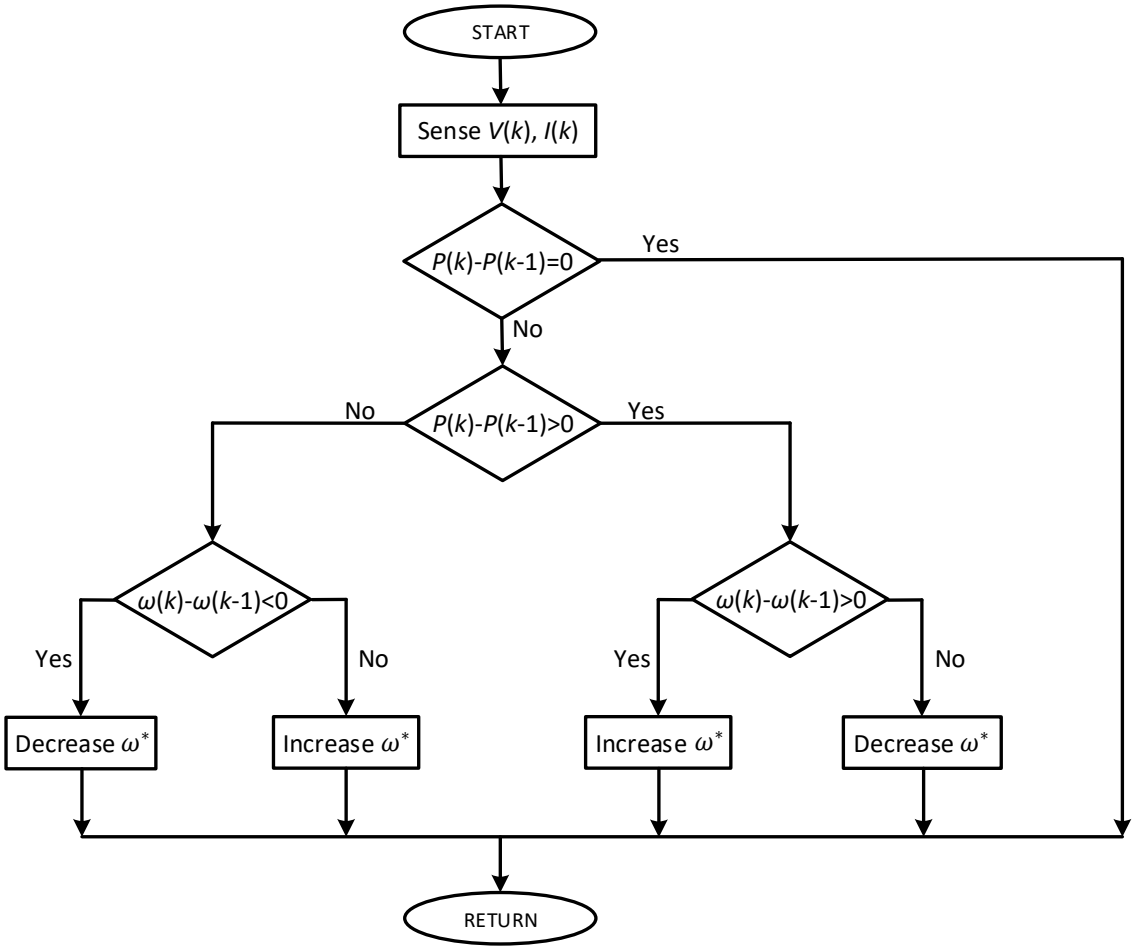

Figure 2.17. Flowchart of the P&O algorithm for wind/hydrokinetic turbines.

A P&O technique based on the perturbation of the duty cycle of a dc-dc converter is presented in [78] for a similar system to the one of Figure 2.8(c). The same technique with the implementation of different dc-dc converters is reported in [79], [80]. The advantage of perturbing the duty cycle of the converter is that there is no dependency on the rotor-speed and power converter ratings.

Similar techniques, without the use of mechanical sensors have been reported in the literature [73]. In [76], the perturbation variable is the rectifier voltage V, while in [81] the controlled variable is the input current to the dc-dc converter.

The MPPT based on the optimum relationship between the rectifier voltage and current is presented in [82]. Another approach is presented in [83], where a matrix converter is used to control of the frequency and the voltage of the generator terminal. However, in this case there is high dependence on the system parameters. In addition,

maximum power extraction using a control scheme of a switched reluctance generator is presented in [84]; however, this is not a popular application for wind power take-off and MPPT.

The tracking procedure for a constant wind/water speed is shown in Figure 2.18.

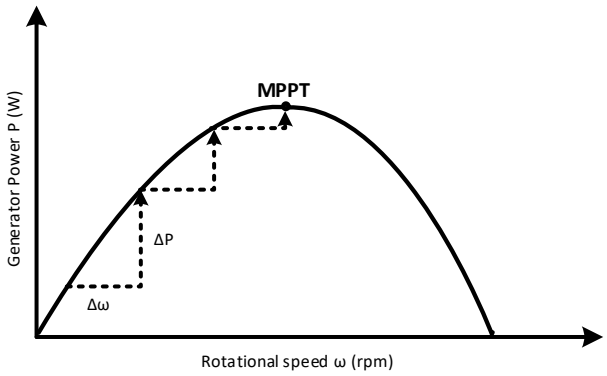

Figure 2.18. MPPT in a wind turbine for a constant wind speed.

P&O is a rather simple MPPT method to be implemented, but its use in turbine applications comes with some challenges. The first challenge is the appropriate selection of the step-size of the perturbation. A small step-size results in a high efficiency, but also in a decreased speed of convergence. A large step-size improves the convergence speed, although higher oscillations around the maximum power point (MPP) are observed. To relieve the aforementioned issues, adaptive step-size methods have been proposed [81], [85]. In these methods, the step-size of the perturbation is varied depending on the distance of the current operating point from the MPP.

Another challenge is that in the case of medium or large wind turbines, a rapid change in the wind speed may result in losing track of the MPP. This uncertainty occurs because the power difference due to the change in the wind speed is not distinguished from the change in power resulting from the previous perturbation. To limit this problem, hybrid methods (slope-assisted P&O) combining a look-up table based MPPT method with the P&O algorithm have been proposed [86].

In addition to the heuristic algorithms previously discussed, fuzzy logic and neural networks are also considered in control schemes for maximum power extraction. For example, in [87] fuzzy logic is used for the control of the firing angle of the inverter, while in [88], a neural network-based method is used for the estimation of the wind speed in order to avoid the use of an anemometer and mechanical sensors.

2.6 Summary

Horizontal and vertical-axis turbines are considered for wind and hydrokinetic energy conversion systems. Large wind turbines mainly use horizontal-axis turbines, while both designs are considered for hydrokinetic energy conversion systems depending on the application. Horizontal-axis turbines are discussed for tidal turbines and vertical-axis turbines are reported in the literature for river streams or man-made waterways.

Power electronics are used for the variable-speed operation of wind turbines. As hydrokinetic energy conversion systems are fairly newer than wind turbines, the same configurations are considered for the variable operation of the hydrokinetic turbines. DFIG-based and FRC-based turbines are the dominant types. Although the FRC-based turbines mainly use back-to-back VSCs, a combination of a diode-bridge rectifier, a dc-dc converter and a voltage source inverter is reported in the literature especially for small scale turbines.

Depending on the turbine configuration, different control strategies are employed for the variable-speed operation for speeds between the cut-in and the rated speed. This way, a restraining torque is applied to the generator and the MPPT is achieved. The control schemes are either based on a predefined trajectory or a heuristic algorithm.

Chapter 3
Modelling of grid connected renewables

3.1 Introduction

Several studies have been conducted towards the modelling of renewable energy sources and their connection to the electricity grid. The increasing integration of renewable energy sources to the grid comes with new challenges regarding the power-supply reliability and quality [89]. Grid connected renewables such as photovoltaic systems, wind turbines, tidal turbines and hydrokinetic turbines are connected to the grid through power converters. Usually two back-to-back converters are used; a controlled rectifier for the MPPT of the renewable system and an inverter for the connection to the grid and the maintenance of the dc voltage.

Among the turbine-based renewable energy conversion systems, wind turbines are the prominent technology. In the UK, the installed capacity of wind generation is expected to increase up to 33 GW by 2030, with a number of projects currently under construction or planned in the short term [90]. Wind farms are required to behave as much as possible as conventional power plants to support the network. As such, different studies are carried out on the capability of wind farms to provide ancillary services and to meet the Grid Code requirements.

In this chapter, detailed DFIG and FRC-based wind turbines were modelled using MATLAB/Simulink. Aerodynamic and drive-train models were included to obtain more realistic configurations. The aerodynamic model was used for the implementation of the aerodynamic torque generated by the wind turbine. BLADED, a commercial software, was employed to specify the power coefficient (C_p) used for the calculation of the generated aerodynamic power for a practical 2 MW wind turbine. The control schemes for the grid-side and the machine-side converters and an optimum power extraction scheme were included. Tower shadow effect and above rated wind speed operation were not considered. The compliance of the wind turbines with the Grid Code requirements were tested.

3.2 GB TSO requirements

3.2.1 Fault ride-through requirements

The fault ride-through requirements for wind turbines are specified by the TSO of each country. Although these vary from one country to another, turbines are expected to operate at a reduced voltage for a few milliseconds to several seconds. The fault ride-through capability demanded by National Grid is shown in Figure 3.1.

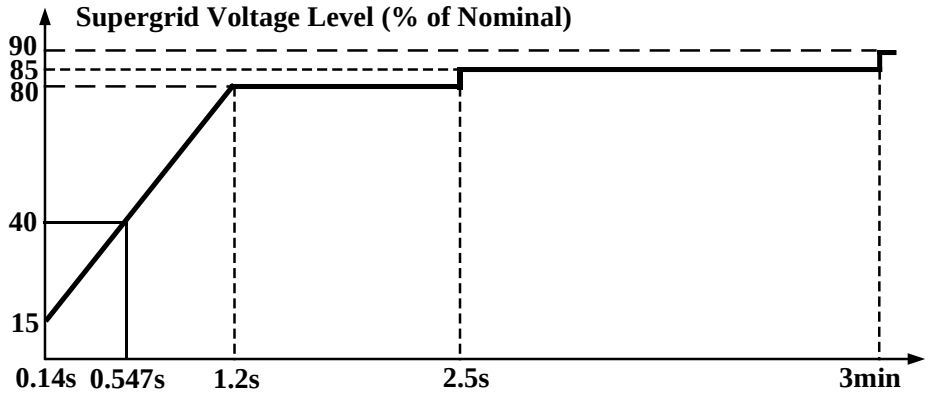

Figure 3.1. Fault ride-through requirements defined by the UK TSO [91].

3.2.2 Frequency in the GB power system

The frequency of the GB power system in steady state is set at 50 ± 0.5 Hz. At present, the GB system is designed to retain stability of operation for a maximum loss of 1320 MW of generation, with the frequency drop limited to −0.8 Hz. An example of the frequency variation for a generation loss of 1320 MW is illustrated in Figure 3.2. In future, the maximum loss of generation is expected to increase to 1800 MW with the connection of larger generators [92].

According to Figure 3.2, when a sudden failure in generation or a connection of a large load takes place the system, the frequency drops. The initial rate of change of frequency is determined by the total inertia of the generators and spinning loads. The GB TSO has specified requirements regarding the provision of particular services in order for the frequency to be brought back to its nominal value. These services include primary and the secondary frequency response. Primary frequency response can be defined as the immediate delivery of active power provided by a generation unit available between 10 and 30 s after the frequency event. After further frequency fall

is prevented, secondary frequency response is provided: active power output increases and this lasts between 30 s and 30 min after the frequency event [93].

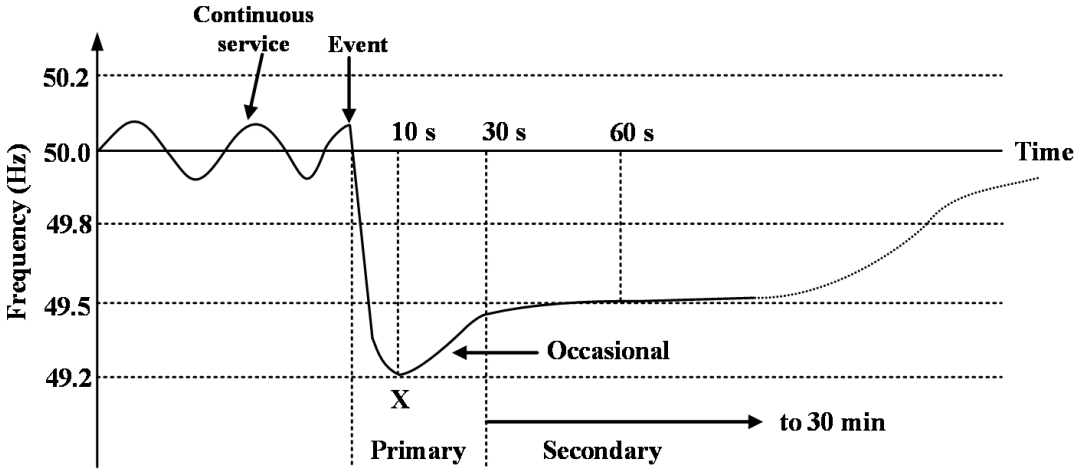

Figure 3.2. Frequency deviation for a generation loss of 1320 MW [93].

3.3 Modelling of a wind turbine

3.3.1 Aerodynamic modelling

The aerodynamic torque τ_{aero} developed by the wind turbine rotor is given by [14]

$$\tau_{aero} = \frac{\rho A V_w^3 C_P(\lambda, \beta)}{2\omega_{rot}} \tag{3.1}$$

where ρ is the air density (kg/m^3), A is the swept area of the rotor (m^2), V_w is the wind speed (m/s), ω_{rot} ithe rotor speed (rad/s) and C_P is the power coefficient which is a function of the blade pitch angle β (deg) and tip speed ratio λ.

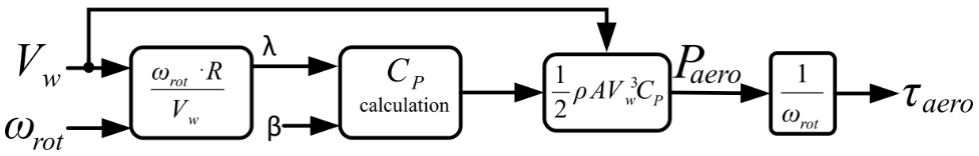

Figure 3.3. Aerodynamic model.

A simplified aerodynamic model, neglecting any dynamic inflow effects, wind shear or tower shadow effect was used to convert wind energy to aerodynamic torque, as shown in Figure 3.3. The power coefficient (C_P) can either be obtained using a polynomial equation or a look-up table [14]. BLADED, a commercial software, was employed to specify the power coefficient (C_p) used for the calculation of the generated aerodynamic power for a practical 2 MW wind turbine, with parameters specified in the Appendix A.

3.3.2 Drive-train model

The torque developed by the wind turbine is transferred to the generator shaft via the drive-train. The drive-train consists of an aerodynamic rotor, a low-speed shaft (LSS), a gearbox, a high-speed shaft (HSS) and a generator.

A common way to model the drive-train of a wind turbine is through a number of masses separated by springs [8]. Lumped (single-mass), two-mass and three-mass models are commonly used depending on the nature of the problem studied [12].

Particularly, for a three-mass model of the drive-train, three inertia constants are considered for: the flexible part of the blade, the rigid part of the blade and the generator. The three-mass model is illustrated in Figure 3.4 and was used for this study.

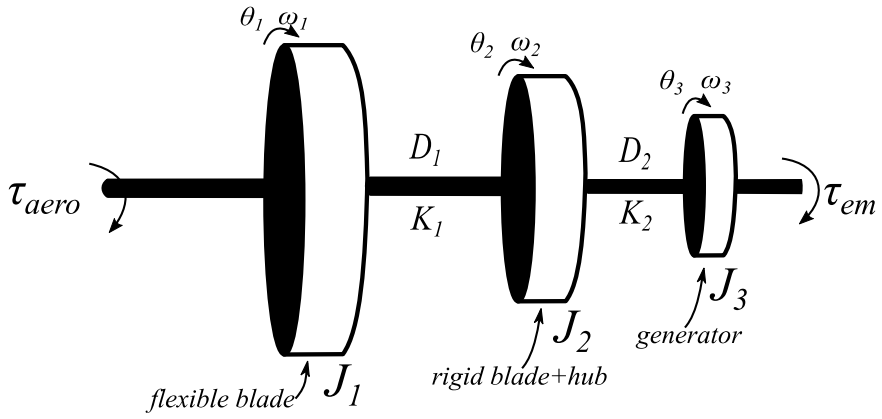

Figure 3.4. Three-mass model of the wind turbine drive-train [12].

The dynamic equations referred to the LSS are [94]

$$J_1 \frac{d}{dt}\omega_1 = \tau_{aero} - K_1(\theta_1 - \theta_2) - D_1 \frac{d}{dt}(\theta_1 - \theta_2) \tag{3.2}$$

$$J_2 \frac{d}{dt}\omega_2 = -K_1(\theta_2 - \theta_1) - K_2\left(\theta_2 - \frac{\theta_3}{N}\right) + -D_1 \frac{d}{dt}(\theta_2 - \theta_1) - D_2 \frac{d}{dt}\left(\theta_2 - \frac{\theta_3}{N}\right) \tag{3.3}$$

$$J_3 \frac{d}{dt}\omega_3 = -\tau_{em} - K_2\left(\frac{\theta_3}{N} - \theta_2\right) - D_2 \frac{d}{dt}\left(\frac{\theta_3}{N} - \theta_2\right) \tag{3.4}$$

$$\frac{d}{dt}\theta_1 = \omega_1, \qquad \frac{d}{dt}\theta_2 = \omega_2, \qquad \frac{d}{dt}\theta_3 = \omega_3 \tag{3.5}$$

where $J_1,\ J_2, J_3$ (kg·m^2) are the inertias of the flexible part of the blades, the hub and the rigid part of the blades and the generator, respectively; K_1, K_2 (N·m/rad) are the

effective blade stiffness and the resultant stiffness of the LSS and HSS, respectively; D_1, D_2 (N·m·s/rad) are the effective blade and resultant LSS-HSS damping factors, respectively; ω_1, ω_2, ω_3 (rad/s) are the rotor, LSS and generator speeds, respectively; N is the gearbox ratio and τ_{em} (N·m) is the electromagnetic torque.

3.4 Modelling of FRC-based wind turbines

The topology of an FRC-based wind turbine modelled in this work is shown in Figure 3.5. It consists of a PMSG and a power converter system consisting of two back-to-back VSCs connected to an infinite bus representing an ac grid. For the simulations, an ideal voltage source was used to represent the infinite bus. The infinite bus is used to represent the grid with the assumption of an infinite upstream capacity. This means that the voltage at this bus is always constant and any downstream disturbances do not affect the voltage.

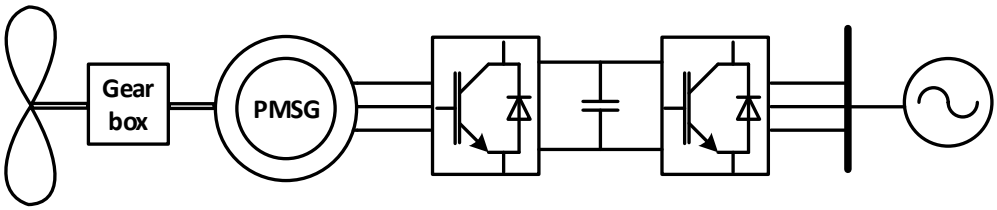

Figure 3.5. FRC-based wind turbine connected to an infinite bus.

3.4.1 Modelling of a permanent magnet synchronous generator

The PMSG model in the *dq* frame is given in [95] as

$$\frac{d}{dt}i_d = \frac{1}{L_d}v_d - \frac{R_s}{L_d}i_d + \frac{L_q}{L_d}n_{pp}\omega_{gen}i_q \tag{3.6}$$

$$\frac{d}{dt}i_q = \frac{1}{L_q}v_q - \frac{R_s}{L_q}i_q - \frac{L_d}{L_q}n_{pp}\omega_{gen}i_d - \frac{\lambda_m n_{pp}\omega_{gen}}{L_q} \tag{3.7}$$

$$\tau_{em} = \frac{3}{2}n_{pp}\left[\lambda_m i_q + \left(L_d - L_q\right)i_d i_q\right] \tag{3.8}$$

where L_d, L_q (H) are the self inductances of the stator; R_s (Ω) is the stator resistance; v_d, v_q (V) are the stator voltages; i_d, i_q (A) are the stator currents; λ_m (V·s) is the flux linkage of the permanent magnet; n_{pp} the pole pairs and ω_{gen} is the generator mechanical speed.

3.4.2 Controller for the machine-side converter

The generator-side converter is controlled using a vector control scheme, such as the unity power factor and the maximum torque per ampere control [12]. In this work, the maximum torque per ampere control was used and the block diagram is illustrated in Figure 3.6.

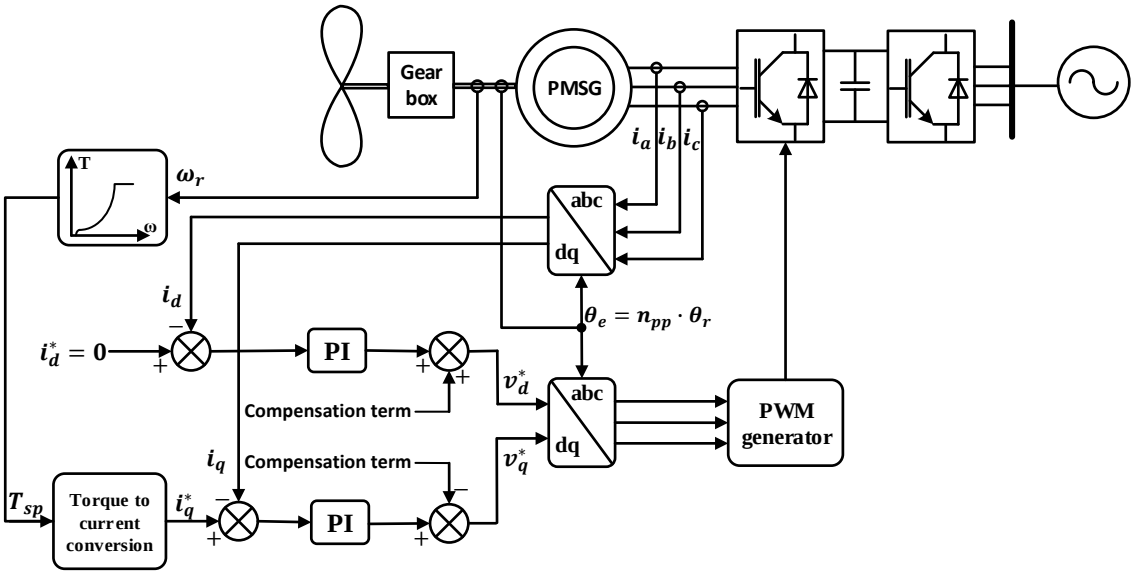

Figure 3.6. Vector control scheme for the generator-side converter of the PMSG [96].

The stator currents are transformed into their equivalent *d* and *q*-axis components using Park's transformation given in Appendix E.

The *q*-axis component of the current is set equal to the stator current and is used to control the torque. For a specific measurement of the generator speed ω_r, a reference set point for the torque T_{SP} is obtained through a look-up table, according to the characteristic for the maximum power extraction. The reference value for the *q*-axis component of the current i_q^* is then calculated and the difference with the measured value i_q is fed to a PI controller. The sum of the output of the PI controller and a compensation term is the *q*-axis component of the controllable voltage v_q^*.

The reference value for the *d*-axis component of the current i_d^* is set to zero. The error between the reference value and the measured value i_d is used as an input to a PI controller. The output of the PI controller is added to a compensation term and the *q*-axis component of the controllable voltage v_d^* is obtained.

Finally, the compensation terms are added so that the independent control of *d* and *q*-axis is guaranteed. The resulting voltages v_q^* and v_d^* are transformed to the *abc* frame and the three-phase voltages are fed to a PWM generator.

According to [95], assuming that the machine has no saliency, (3.8) becomes

$$\tau_{em} = \frac{3}{2} n_{pp} \lambda_m i_q \tag{3.9}$$

Thus, the reference for the stator current is given by

$$i_q^* = T_{SP} \ \frac{2}{3 n_{pp} \lambda_m} \tag{3.10}$$

The compensation term for the *d*-axis current is given by

$$CT1 = \omega_r L_q i_q \tag{3.11}$$

The compensation term for the *q*-axis current is given by

$$CT2 = \omega_r (L_d i_d + \lambda_m) \tag{3.12}$$

3.4.3 Controller for the grid-side converter

Vector control was also used for the control of the grid-side converter to supply active and reactive power to the grid independently [40]. To achieve this, the reference frame is oriented with the supply voltage vector.

For a balanced system, the active and reactive powers in the *dq* frame are given by

$$P = \frac{3}{2} (v_q i_q + v_d i_d) \tag{3.13}$$

$$Q = \frac{3}{2} (v_q i_d - v_d i_q) \tag{3.14}$$

The supply voltage is aligned with the *d*-axis. The *q*-axis component of the supply voltage is set to zero. Therefore, the equations (3.15) and (3.16) reduce to

$$P = \frac{3}{2} v_q i_q \tag{3.15}$$

$$Q = -\frac{3}{2} v_d i_q \tag{3.16}$$

For the control of the grid-side converter, a PLL is employed to obtain the frequency used for the transformation of the current in the *dq* frame. The *d*-axis component of

the current is used to regulate the dc voltage. The reference value for the q-axis component of the current is set to zero, so that no reactive power is provided.

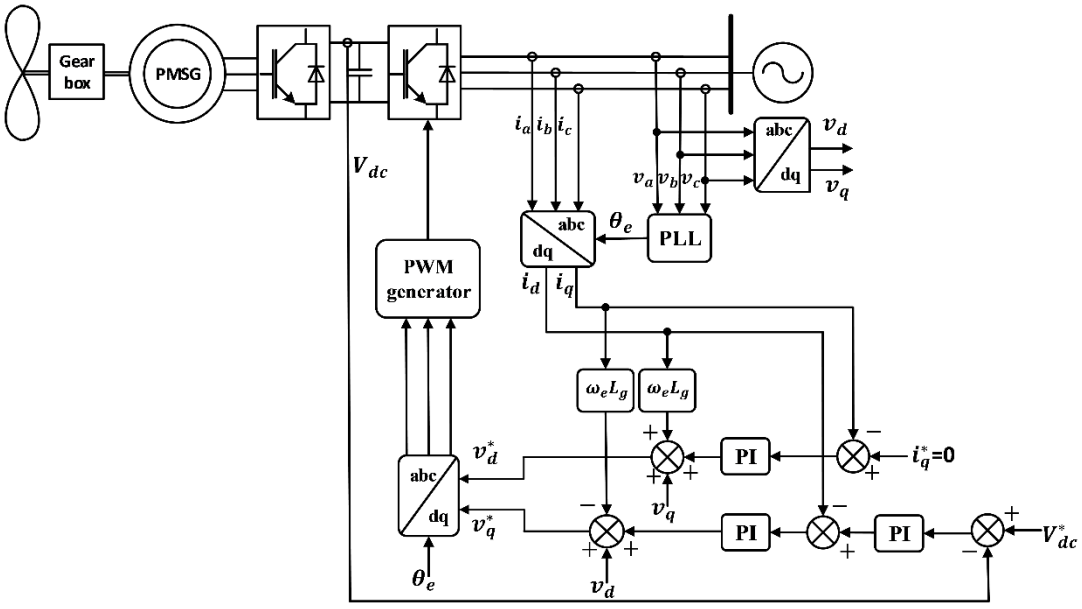

Figure 3.7. Control scheme for the grid-side converter [97].

As shown in Figure 3.7, the difference between the reference value for the dc link voltage and the measured one is used as an input to the PI controller, so that the reference value for the *d* component of the current is provided (outer loop). The difference between the reference value of the *d*-axis current and the measured one is processed by a PI controller (inner current loop). A feed forward term (v_d) is added to the output of the inner current loop, to improve the system response. Compensation (decoupling) terms are also used so that independent control of active and reactive power is ensured. The resulting voltages which are in the *dq* frame are transformed to instantaneous voltage values which are used to generate the PWM signals for the converter [97].

3.4.4 Inertia response control scheme

As wind integration increases, wind farms are expected to participate in the provision of ancillary services, like inertia response. To this end, different methodologies have been proposed, such as inertial coupling [98], [99] and step change in active power output [100], [101]. The main advantage of the first option against the later one is that through the inertial coupling, the response of the machine can be very similar to the natural inertia. In fact, if an artificial inertia higher than the natural response is considered, the frequency response capabilities of the generator are bigger. On the

contrary, applying a step change in the active power output of the generator and thus the torque reference can have a considerable impact on the mechanical stress applied on the shaft.

The kinetic energy stored in the rotor of a variable-speed wind turbine is given by

$$E_k = \frac{1}{2} J \omega_{rot}^2 \tag{3.17}$$

where J is the inertia of the rotor (kg·m^2).

The power stored in the rotating masses is given by calculating the first derivative of the energy

$$P_k = \frac{dE_k}{dt} = J\omega_{rot}\frac{d\omega_{rot}}{dt} \tag{3.18}$$

Using the per unit inertia constant H, (3.20) is expressed as

$$\begin{aligned} P_k &= \frac{2HS_{base}}{\omega_{base}^2}\omega_{rot}\frac{d\omega_{rot}}{dt} \\ \rightarrow \overline{P_k} &= 2H\overline{\omega}_{rot}\frac{d\overline{\omega}_{rot}}{dt} \end{aligned} \tag{3.19}$$

where the overstrike denotes the per unit values.

From (3.20), it is shown that for a change in the rotational speed, a change in power occurs. Thus, the energy stored in the rotating mass can be used for inertial response. However, FRC-based wind turbines are completely decoupled from the grid and the generator controller is not affected by any change in the system frequency. Therefore, the generator torque controller should be modified for the provision of inertial frequency response.

In this work, a supplementary control loop was added to the generator-side controller of the FRC-based wind turbine, as shown in Figure 3.8. This control scheme was used to extract the kinetic energy stored in the rotor of the PMSG and can be found in [101].

In the event of a drop in the frequency of the system, a deceleration torque is applied to the generator (proportional to df/dt) and the rotor is forced to slow down. This way, an over-production takes place due to the extraction of kinetic energy stored in the rotor.

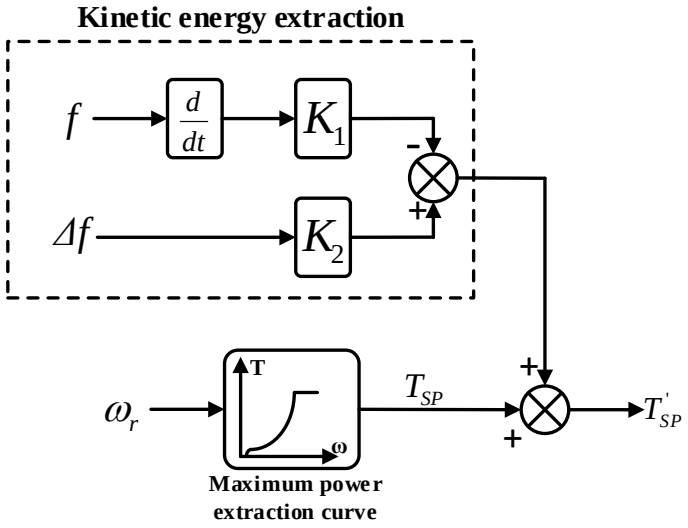

Figure 3.8. Inertia response control scheme [101].

3.5 Modelling of a DFIG-based wind turbine

Figure 3.9 shows a DFIG-based wind turbine connected to an infinite bus. A wound rotor induction generator is used and back-to-back VSCs are implemented, so that a controllable voltage is injected into the rotor winding at slip frequency.

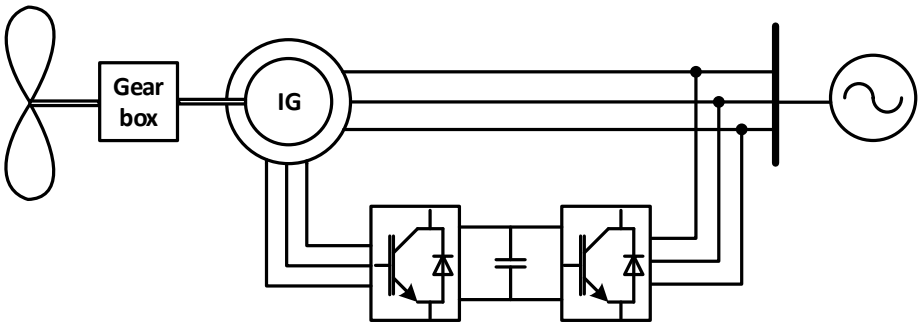

Figure 3.9. DFIG-based wind turbine connected to infinite bus.

3.5.1 Modelling of a DFIG

A per unit representation of the electrical model of the induction generator in the *dq* frame was adopted, given as [41]

$$\overline{v}_{ds} = -\overline{R}_s\overline{i}_{ds} - \overline{\omega}_s\overline{\psi}_{qs} + \frac{1}{\omega_b}\cdot\frac{d}{dt}\overline{\psi}_{ds} \tag{3.20}$$

$$\overline{v}_{qs} = -\overline{R}_s\overline{i}_{qs} - \overline{\omega}_s\overline{\psi}_{ds} + \frac{1}{\omega_b}\cdot\frac{d}{dt}\overline{\psi}_{qs} \tag{3.21}$$

$$\overline{v}_{dr} = \overline{R}_r \overline{i}_{dr} - s\overline{\omega}_s \overline{\psi}_{qr} + \frac{1}{\omega_b} \cdot \frac{d}{dt} \overline{\psi}_{dr} \tag{3.22}$$

$$\overline{v}_{qr} = \overline{R}_r \overline{i}_{qr} + s\overline{\omega}_s \overline{\psi}_{dr} + \frac{1}{\omega_b} \cdot \frac{d}{dt} \overline{\psi}_{qr} \tag{3.23}$$

$$\overline{T}_e = \frac{\overline{e}_d \overline{i}_{ds} + \overline{e}_q \overline{i}_{qs}}{\overline{\omega}_s} \tag{3.24}$$

where $\overline{e}_d$, $\overline{e}_q$, $\overline{v}_{ds}$, $\overline{v}_{qs}$, $\overline{v}_{dr}$, $\overline{v}_{qr}$ (V) are the internal, stator and rotor voltages; $\overline{i}_{ds}$, $\overline{i}_{qs}$, $\overline{i}_{dr}$, $\overline{i}_{qr}$ (A) are the stator and rotor currents; $\overline{\psi}_{ds}$, $\overline{\psi}_{qs}$, $\overline{\psi}_{dr}$, $\overline{\psi}_{qr}$ (V·s) are the stator and rotor flux linkages; $\overline{R}_s$, $\overline{R}_r$ are the stator and rotor resistances; ω_b, $\overline{\omega}_s$ are the base and synchronous speeds; s is the slip and $\overline{T}_e$ is the electromagnetic torque. The overstrike denotes the per unit values

The flux variables used in (3.22)-(3.26) are given by [12]

$$\overline{\psi}_{ds} = -\overline{L}_{ss} \overline{i}_{ds} + \overline{L}_m \overline{i}_{dr} \tag{3.25}$$

$$\overline{\psi}_{qs} = -\overline{L}_{ss} \overline{i}_{qs} + \overline{L}_m \overline{i}_{dr} \tag{3.26}$$

$$\overline{\psi}_{dr} = \overline{L}_{rr} \overline{i}_{dr} - \overline{L}_m \overline{i}_{ds} \tag{3.27}$$

$$\overline{\psi}_{qr} = \overline{L}_{rr} \overline{i}_{qr} - \overline{L}_m \overline{i}_{qs} \tag{3.28}$$

$$\overline{L}_{ss} = \overline{L}_{ls} + \overline{L}_m \tag{3.29}$$

$$\overline{L}_{rr} = \overline{L}_{lr} + \overline{L}_m \tag{3.30}$$

where $\overline{L}_m$ is the mutual inductance between stator and rotor windings, $\overline{L}_{ls}$ is the stator leakage inductance and $\overline{L}_{lr}$ is the rotor leakage inductance.

3.5.2 Controller for the machine-side converter

The PVdq control scheme [12] [40] was chosen for the control of the DFIG. This control scheme is vector control, as in the case of the FRC model, however the stator flux oriented reference frame is used. As shown in Figure 3.10, for a specific measurement of the rotor speed ω_r, a reference set point for the torque is obtained through a look-up table, according to the curve for the maximum power extraction. The reference value for the q-axis component of the rotor current i_{qr}^* is then calculated

and the difference with the measured value i_{qr} is fed to a PI controller. The sum of the output of the PI controller and a compensation (decoupling) term is the q-axis component of the voltage v_{qr} that is injected to the rotor winding.

According to [12], torque can be expressed as

$$\overline{T}_e = \overline{L}_m(\overline{i}_{dr}\overline{i}_{qs} - \overline{i}_{qr}\overline{i}_{ds}) \tag{3.31}$$

Assuming that the stator resistance is zero and neglecting the stator transients, (3.22) and (3.28) give

$$\overline{v}_{ds} = -\overline{\omega}_s(-\overline{L}_{ss}\overline{i}_{qs} + \overline{L}_m\overline{i}_{qr}) \tag{3.32}$$

Therefore, the q-component of the current is expressed as

$$\overline{i}_{qs} = \frac{1}{\overline{\omega}_s\overline{L}_{ss}}\overline{v}_{ds} + \frac{\overline{L}_m}{\overline{L}_{ss}}\overline{i}_{qr} \tag{3.33}$$

Since the stator flux oriented reference frame is used ($\overline{v}_{ds} = 0$), (3.35) is reduced to

$$\overline{i}_{qs} = \frac{\overline{L}_m}{\overline{L}_{ss}}\overline{i}_{qr} \tag{3.34}$$

Assuming that the stator resistance is zero and neglecting the stator transients, (3.23) and (3.27) give

$$\overline{v}_{qs} = \overline{\omega}_s(-\overline{L}_{ss}\overline{i}_{ds} + \overline{L}_m\overline{i}_{dr}) \tag{3.35}$$

Thus, $\overline{i}_{ds}$ can be expressed as

$$\overline{i}_{ds} = -\frac{1}{\overline{\omega}_s\overline{L}_{ss}}\overline{v}_{qs} + \frac{\overline{L}_m}{\overline{L}_{ss}}\overline{i}_{dr} \tag{3.36}$$

Substituting (3.36) and (3.38) in (3.33), the torque is expressed as

$$\overline{T}_e = \overline{L}_m\left[\overline{i}_{dr}(\frac{\overline{L}_m}{\overline{L}_{ss}}\overline{i}_{qr}) - \overline{i}_{qr}(-\frac{1}{\overline{\omega}_s\overline{L}_{ss}}\overline{v}_{qs} + \frac{\overline{L}_m}{\overline{L}_{ss}}\overline{i}_{dr})\right] \tag{3.37}$$

And therefore, the reference for $\overline{i}_{qr}$ is expressed as

$$i_{qr}^* = \frac{\overline{\omega}_s\overline{L}_{ss}}{\overline{L}_m\overline{v}_{qs}}\overline{T}_{sp} \tag{3.38}$$

where $\overline{T}_{sp}$ is the set point for the torque obtained from the torque-speed characteristic for maximum power production.

The compensation term for the control of the torque is given by [12]

$$CT3 = s\overline{\omega}_s\left(\overline{L}_{rr} - \frac{\overline{L}_m^2}{\overline{L}_{ss}}\right)\overline{i}_{dr} - \frac{\overline{L}_m}{\overline{\omega}_s\overline{L}_{ss}}\overline{v}_{qs} \tag{3.39}$$

The *d*-axis component of the current is used to regulate the terminal voltage. The difference between the reference and the measured value of the terminal voltage is used during the primary stage. A reference value for the *d*-axis component of the rotor current i_{dr}^* is calculated and the difference with the measured value i_{dr} is used as an input to the PI controller. The output of the PI controller is added to a compensation (decoupling) term and the *d*-axis component of the rotor voltage v_{dr} is obtained.

According to [12] the *d*-axis component of the rotor current is

$$i_{dr}^* = i_{dr\_m}^* + i_{dr\_g}^* \tag{3.40}$$

Where $i_{dr\_m}^*$ is the magnetising component and $i_{dr\_g}^*$ is the component for the adjustment of the terminal voltage.

The reference value for the magnetising component is defined as

$$i_{dr\_m}^* = \frac{\overline{v}_{qs}}{\overline{\omega}_s\overline{L}_m} \tag{3.41}$$

So that the reactive power consumed by the DFIG is compensated.

For the regulation of the terminal voltage

$$i_{dr\_g}^* = K_{vc}(|v_s^*| - |v_s|) \tag{3.42}$$

where $|v_s|$ is the terminal voltage. Consequently, the terminal voltage of the DFIG is regulated by adjusting K_{vc}.

The compensation term for the voltage is given by [12]

$$CT4 = s\left(\overline{L}_{rr} - \frac{\overline{L}_m^2}{\overline{L}_{ss}}\right)\overline{i}_{qr} \tag{3.43}$$

The resulting voltages v_{qr} and v_{dr} are transformed to the *abc* frame using the slip frequency. The three-phase voltages are then fed to a PWM generator.

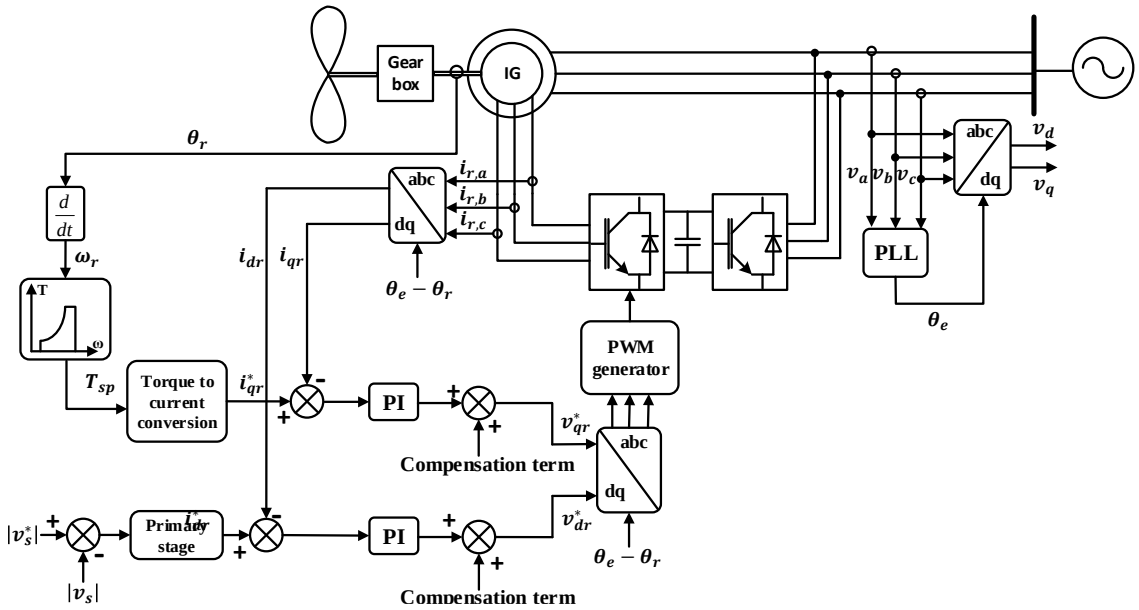

Figure 3.10. Vector control scheme for the rotor-side converter of the DFIG [39].

3.5.3 Controller for the grid-side converter

The control strategy for the grid-side converter is similar as in the case of the FRC-based wind turbine. However, the voltage used as an input to the PLL is measured in the branch just after the grid-side converter and not at the connection point, as shown in Figure 3.11.

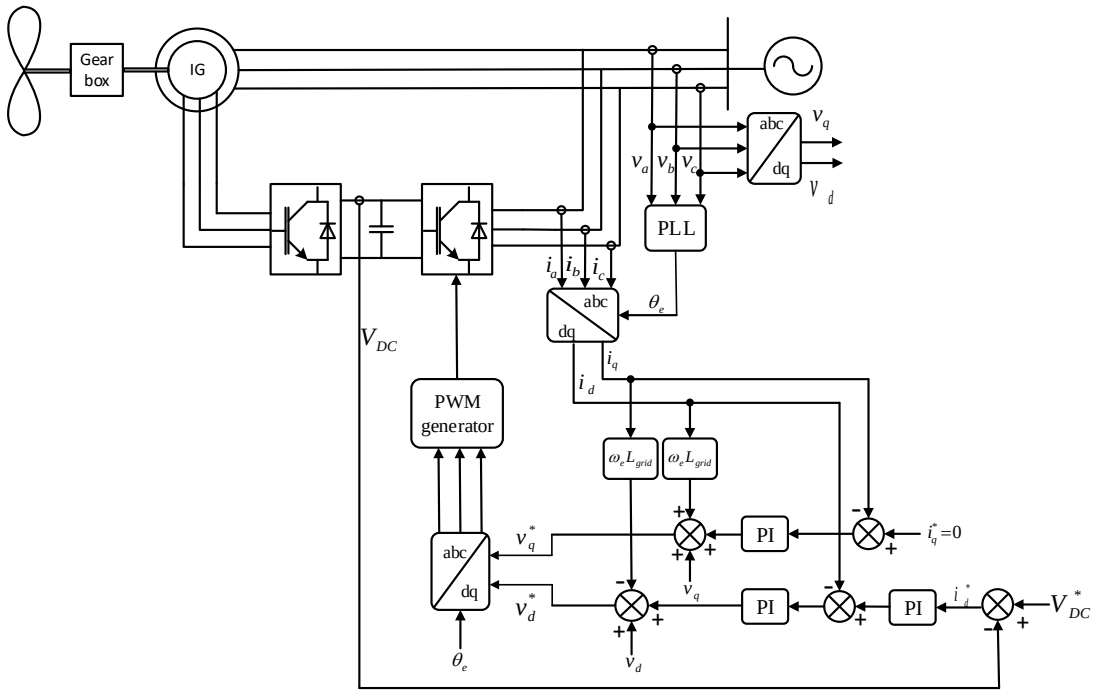

Figure 3.11. Control scheme for the grid-side converter of a DFIG-based wind turbine.

3.6 Simulation results

3.6.1 Grid Code compliance and comparison of the responses of a DFIG and an FRC-based wind turbine

The fault ride-through capability of a 2 MW DFIG-based and a 2 MW FRC-based wind turbine models was investigated. Simulations were conducted using Matlab/Simulink. A voltage sag of 60% was applied at the infinite bus at 1s for 500 ms.

The fault ride-through capabilities of both wind turbine technologies were tested and the results are shown in Figure 3.12 and Figure 3.13. It is shown that there is a larger impact on the DFIG torque rather than the FRC-based one. During the fault, there is a slight change in the torque provided by the PMSG. On the contrary, a peak of 3.5 p.u. is observed in the torque response of the DFIG. This is reasonable since the stator of the DFIG is directly connected to the grid, while the PMSG is electrically isolated from it. Additionally, the dc voltage response does not vary much for either configuration, as shown in Figure 3.13. Thus, it is concluded that both technologies modelled in this work are capable of overcoming the voltage sag.

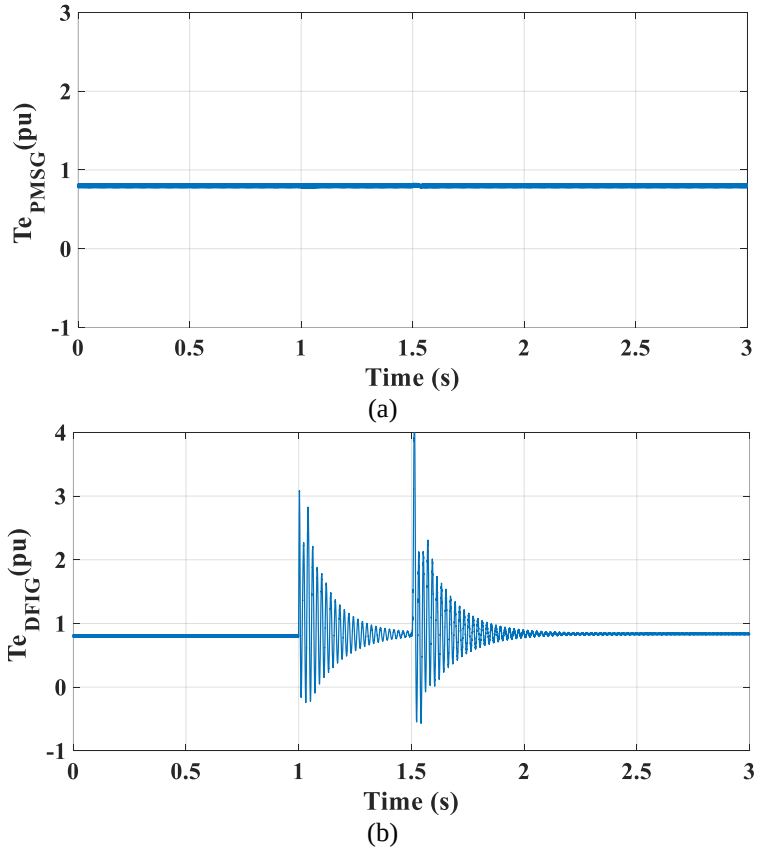

Figure 3.12. PMSG and DFIG response under a 60% voltage sag for 500 ms: electromagnetic torque.

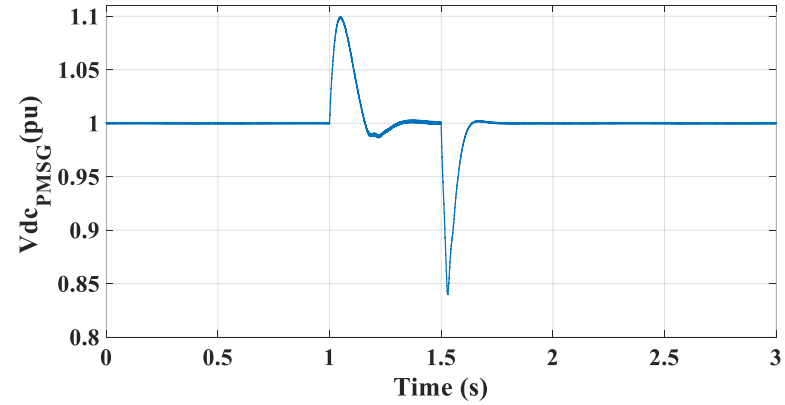

(a)

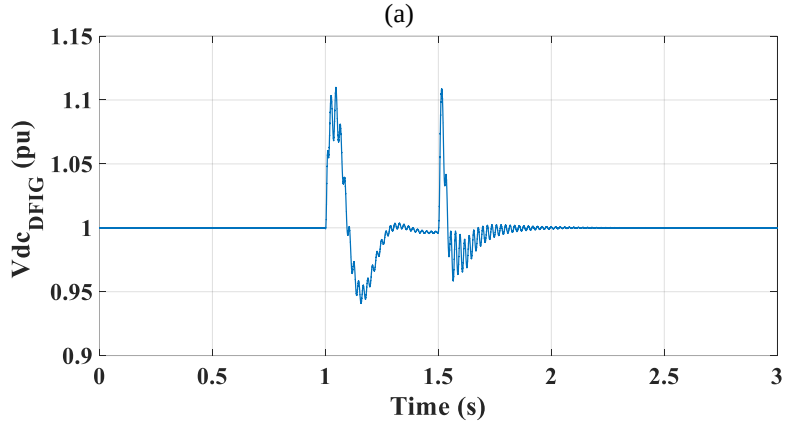

(b)

Figure 3.13. PMSG and DFIG response under a 60% voltage sag for 500 ms: dc voltage.

Figures 3.14 and 3.15 show the current waveforms of the generators and the converters for both the FRC and the DFIG-based wind turbines. The magnitudes of the currents were obtained using their *dq* axis components: $i_{magn} = \sqrt{i_d^2 + i_q^2}$. Figure 3.14 shows the magnitude of the current of the grid side converter $i_{GSC,magn}$(a) and the stator $i_{s,magn}$ (b) under the voltage sag of 60% for 500 ms. It is shown that there is almost no impact on the stator current as expected according to the response of the torque shown in Figure 3.12. However, there is a big impact on the current of the grid side converter which is linked to the response of the dc voltage shown in Figure 3.13. The magnitude of the current becomes even more than twice its rated value. This value, thought, is far above the value of 10% which is set to protect the VSCs. Therefore, a current limiter should be used under normal conditions to avoid harmful effects on the VSCs.

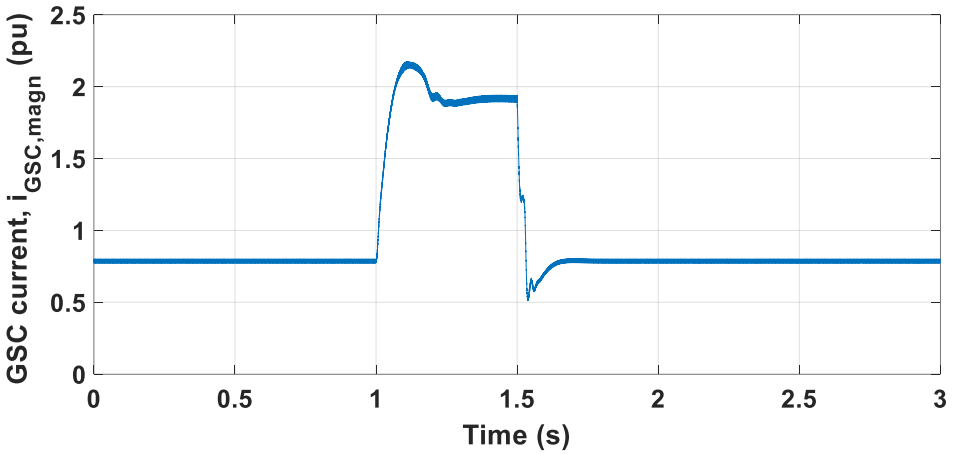

(a)

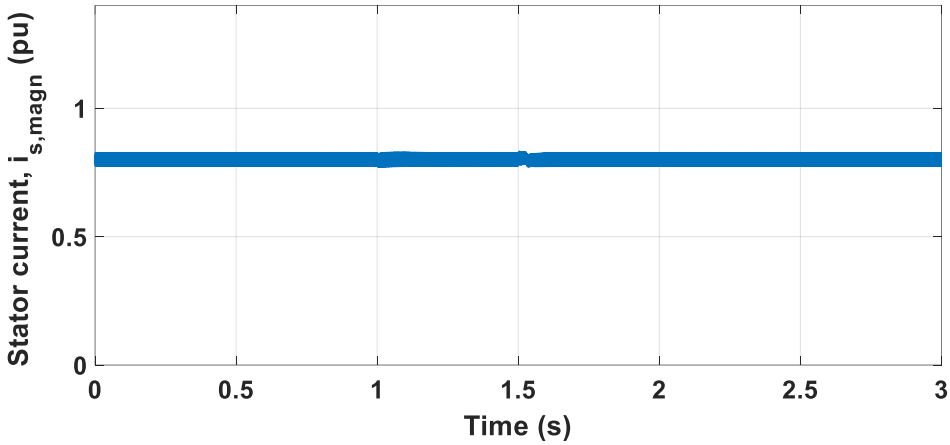

(b)

Figure 3.14. Stator and grid side converter currents of the PMSG under a 60% voltage sag for 500 ms: dc voltage.

Figure 3.15 shows the response of the current of the DFIG-based wind turbine under the voltage sag of 60% for 500 ms. As expected from Figure 3.12, there is a big impact on the stator and the rotor current (Figure 3.15a and 3.15b) posing a risk for the operation of the rotor side converter. Current limiters need to be used for the safe operation of the rotor side VSC. However, the current of grid side converter remains within acceptable limits as shown in Figure 3.15c. In addition, the slip varies slightly as shown in Figure 3.15d.

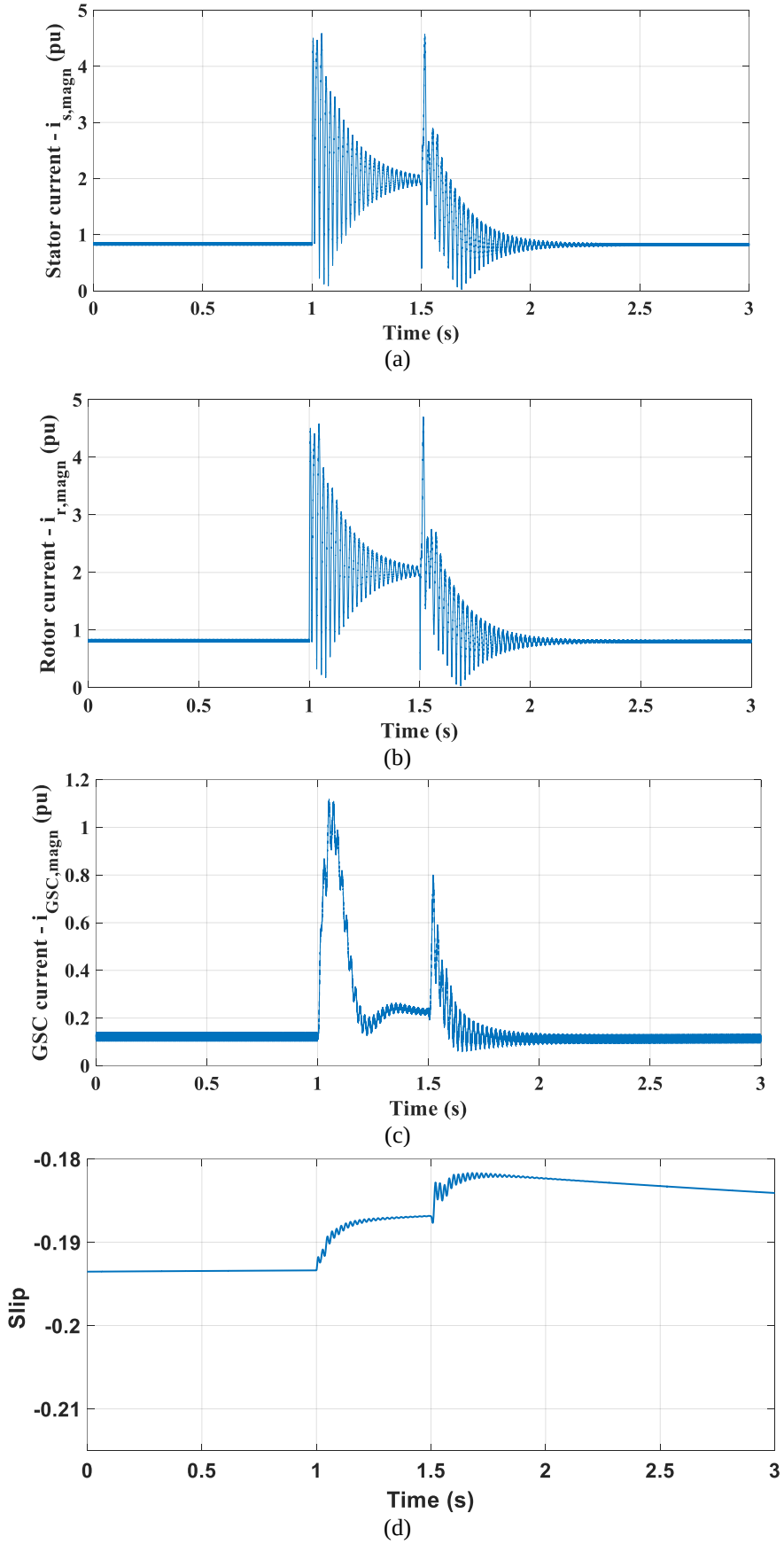

Figure 3.15. Stator, rotor and grid side converter currents and slip of the DFIG under a 60% voltage sag for 500 ms: dc voltage.

The results shown in Figures 3.12-3.15 indicate that the FRC-based wind turbines perform better than DFIG-based ones during a fault. This is due to the fact that the FRC-based turbines are fully decoupled from the grid. On the contrary, the stator of a DFIG is directly connected to the grid and any fault that occurs has an immediate impact on the torque and the stator and the rotor currents of the DFIG.

Although DFIG-based wind turbines are obviously not the best choice to comply with fault ride-through requirements, they were the first variable speed turbines to have be installed. Therefore, the issues associated with their fault ride-through capabilities need to be taken into account. Some of these issues are listed below.

When a fault occurs, the main problem during voltage dips is caused by the natural response of the stator flux linkage. This results in high oscillatory rotor voltages and currents and consequently, electromagnetic torque and generated power oscillations[102]. The voltage collapse caused by a grid fault triggers a decay of flux linkage in the induction machine. According to [103], there are two transient decay components which contribute equally to the fault currents of the generator: a near-dc decay of self-linking flux and a near-rotor-speed decay of mutual flux. The resulting deviation can be 1% for a typical induction machine or over 3.5% for an induction machine with a very high rotor resistance, as in the case of a crowbar resistance shorted across the DFIG's rotor windings. This practically means that a current up to 4-5pu may occur. It is possible to try to limit this current by current-control on the rotor side of the converter. However, in this case high voltages at the converter terminals occur, posing a risk for the destruction of the converter [104].

The resulting currents of a DFIG during a voltage dip can cause failure of the rotor side converter. If the rotor side converter is blocked and wind turbine is tripped. As wind integration increases this problem becomes more severe and can cause a negative impact on the overall stability of the system [105]. To eliminate this effect and keep the wind turbines connected several measures are used. Apart from the use of a crowbar, a static synchronous compensator (STATCOM) can be used to adjust the reactive power after fault occurrence[106]. In addition, a superconducting magnetic energy storage (SMES) unit can provide voltage protection to the rotor side converter. It is a costly equipment, though, and it may not suppress the overcurrent and electromagnetic torque oscillations [107]. On the contrary, installing a

superconducting fault current limiter (SFCL) can restrict the fault current and prevent the disruption of protective equipment [106].

3.6.2 Inertial frequency response from offshore wind farms

The total capacity of OWFs connected to the GB system is approximately 5 GW. The provision of inertia response from OWFs in GB was investigated based on the following assumptions: the offshore farms are based on 2 MW FRC-based wind turbines, like the one described above; the wind turbines operate below rated speed; the wind speed is steady (9.5 m/s) and applied to every single wind turbine.

In this work, the simplified model of the GB power system described in [108] was used, as shown in Figure 3.. Synchronous plants increase their output to respond to a drop in frequency. These responsive plants are represented by a governor droop ($1/R_{eq}$= −11), a governor actuator ($T_G = 0.2$ s) and a turbine ($T_T = 0.3$ s). The lead-lag transfer function is added for stability reasons ($T_1 = 2$ s, $T_2 = 12$ s) between the governor and the turbine. The above parameters were obtained from [108]. The total inertia of the 2020 system has been calculated as 4.44 s [109].

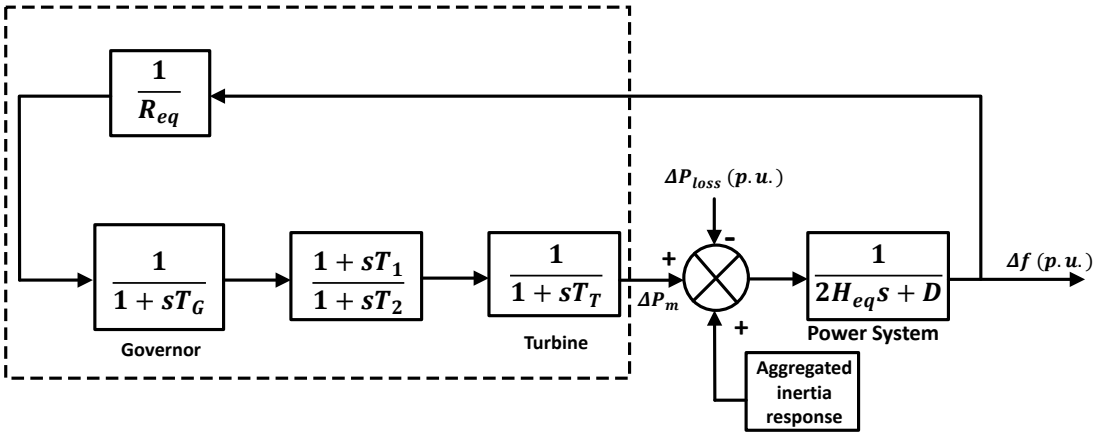

Figure 3.16. Simplified GB power system model [108].

Figure 3.7 shows the frequency deviation of the GB system for a generation loss of 1.8 GW with inertia response (dashed line) and without inertia response (solid line). It can be seen that in case OFWs provide inertia response to the system the rate of change of frequency decreases and the drop of frequency is limited to a higher value.

The impact of the additional control loop shown in Figure 3.8 to the electromagnetic torque developed by the PMSG, the voltage of the dc link, and the additional power generated are illustrated in Figure 3.8. A slight increase of the generated

electromagnetic torque is observed, with a peak of ≈ 0.1 p.u. The variation of the voltage of the dc link is small, with a peak of 0.5% of the nominal value.

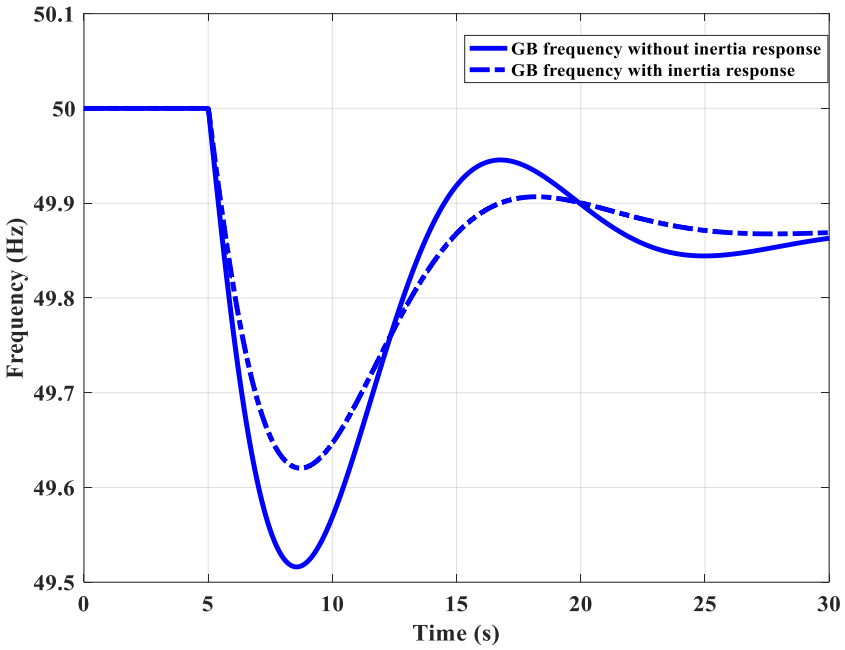

Figure 3.17. GB system frequency deviation for a 1.8 GW loss of generation.

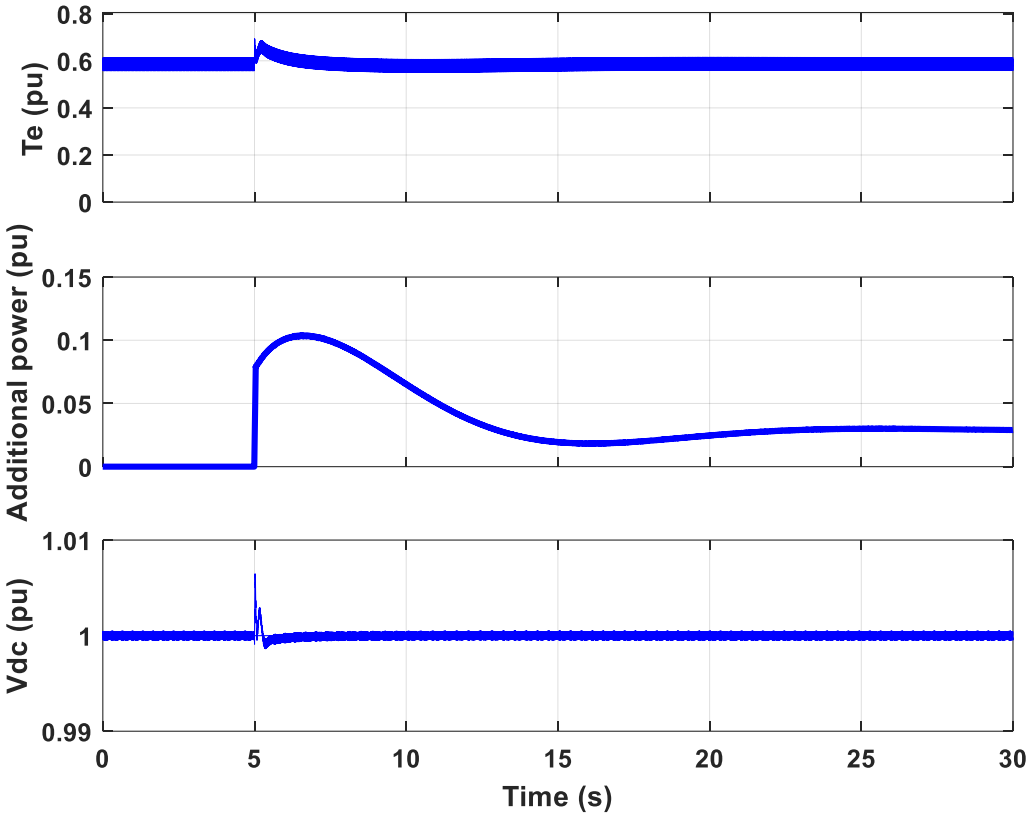

Figure 3.18. Single FRC-based wind turbine contribution to inertia response.

To investigate the impact of the limitations of the converters on the inertia support capabilities of wind turbines, simulations were conducted assuming different current

limiters. It was assumed that an extra ≈40% of the power is reserved and can be released to the grid. Figure 3.19 shows the additional power provided to the grid assuming current limiters of 1.1, 1.3 and 1.5 times the rated current of the converters. It is shown that only in the case of a current limiter of 1.5 times the rated current of the converter, all the available extra power is fed to the grid.

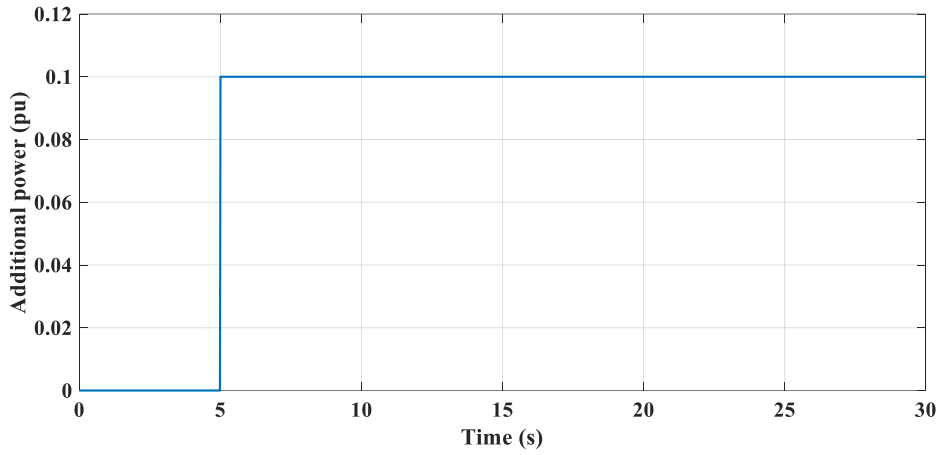

(a)

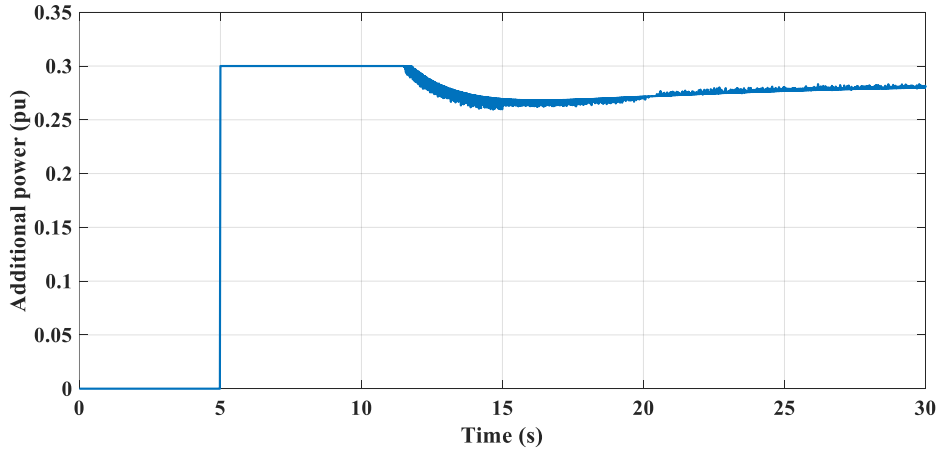

(b)

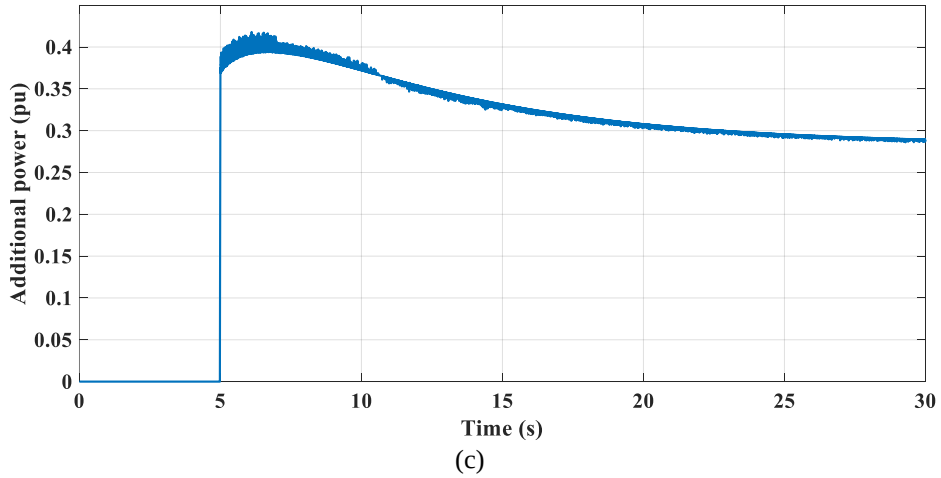

(c)

Figure 3.19. Provision of extra power to the grid with current limiters of (a) 1.1, (b) 1.3 and (c) 1.5 times the rated current of the converters.

The impact of the current limiters on these current limiters on the deviation of the frequency of the GB system is shown in Figure 3.20. It is shown that when the current of the converter is restricted to 1.1 times the rated current, the contribution of the wind turbines to the restoration of the frequency of the system is lower that in the case of a current limiter of 1.5 times the rated current of the converter. Therefore, it is concluded that the inertia support capabilities of the wind turbines does also largely depend on the ratings of the converters.

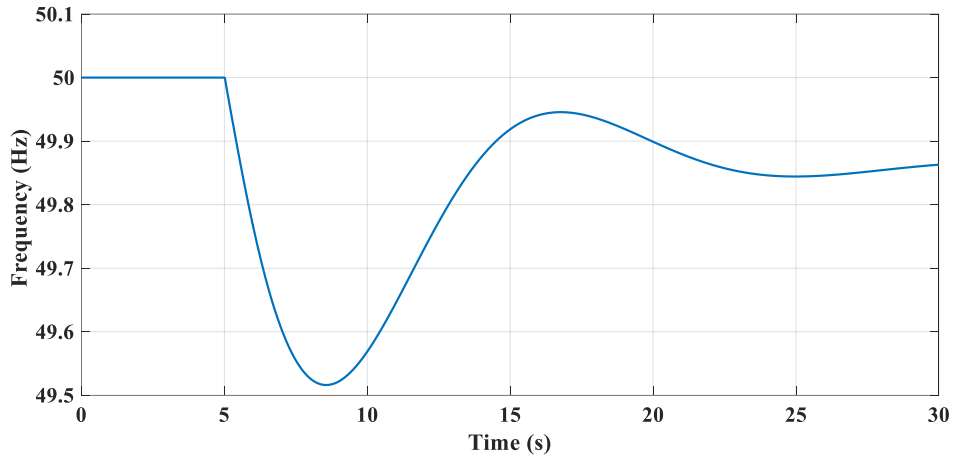

(a)

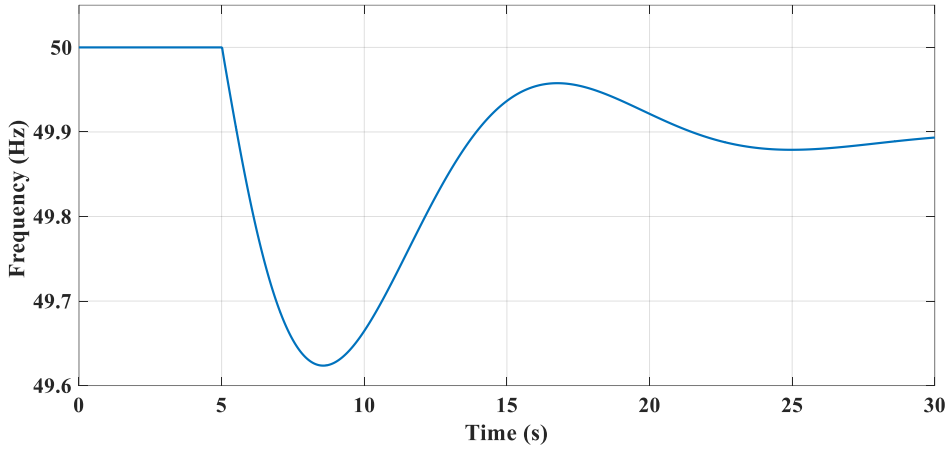

(b)

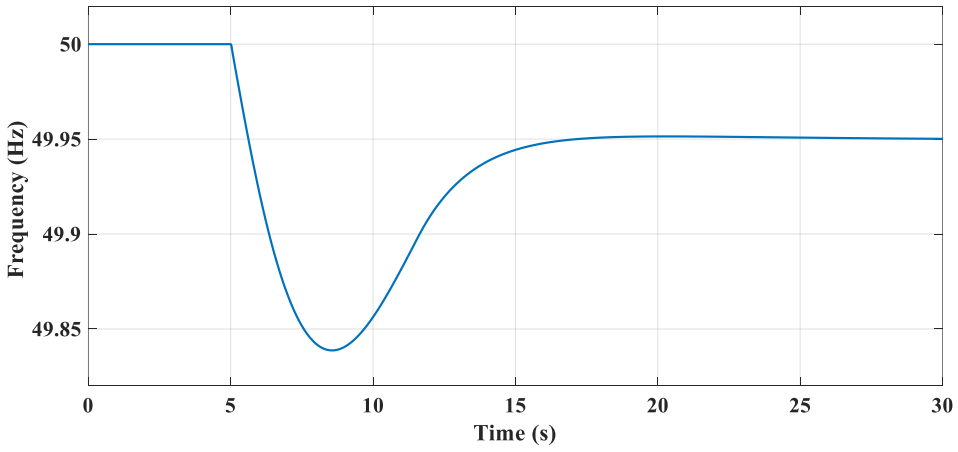

(c)

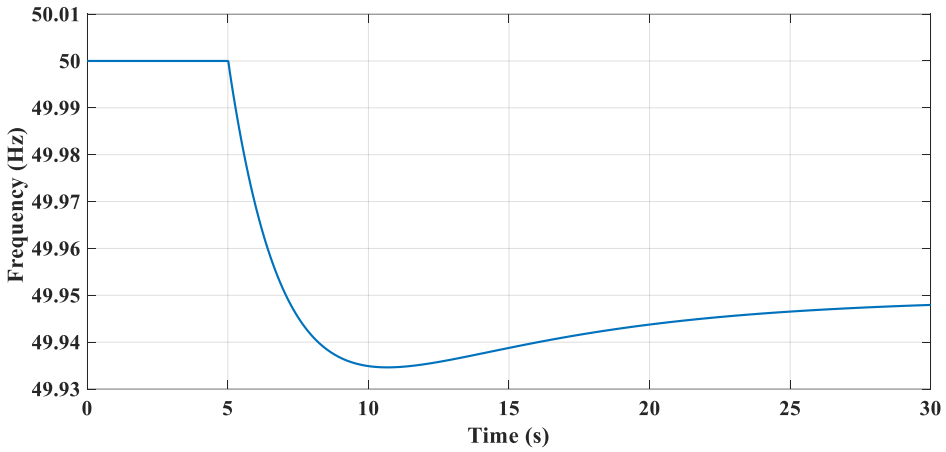

(d)

Figure 3.20. GB system frequency deviation with (a) no inertia support and with inertia support and current limiters of (b) 1.1, (c) 1.3 and (d) 1.5 times the rated current of the converters.

In these case studies, it was assumed that all the wind turbines contribute equally to the inertia support. A more realistic study would include the implementation of wind farms based on different wind turbine technologies considering different wind speeds and network characteristics.

3.7 Summary

In this chapter, control strategies for DFIG and FRC PMSG-based wind turbines were reviewed and presented. Detailed wind turbine models for both technologies considering aerodynamic and shaft flexibilities were implemented in order to assess the performance of the proposed strategies under voltage sag conditions at the point of connection with the grid. It is concluded that although both wind turbine technologies comply with Grid Code requirements issued by National Grid, the UK TSO. However, there is a difference in their dynamic responses.

A simplified model for the frequency deviation of the GB system was used. The inertia response capabilities of FRC PMSG-based wind farms was investigated. The inertial coupling method was used to modify the generator-side controller of each wind turbine. The total capacity of these wind farms was assumed to be equal to the capacity of the installed offshore wind farms in the UK. Results showing the overall contribution to the system inertia as well as the impact on the torque generation and the dc voltage deviation of each wind turbine have been presented. It is seen that the rate of change of frequency is limited to a higher value and the dynamic responses of the PMSG-based wind turbines are within acceptable limits.

The impact of the ratings of the converters on the inertia support capabilities of the FRC-based wind turbines was also investigated. It is shown that when the currents of the converters are limited to low values the inertia support capabilities of the wind turbines are restricted. On the contrary, when the additional power provided to the grid does not lead to currents higher than the rated current of the converters, wind turbines can support the grid and contribute to the restoration of the frequency.

Both studies conducted in this chapter lead to the conclusion that the performance of the FRC-based technology is superior to the performance of DFIG-based under fault ride-through and frequency dips. This is the reason it is mainly considered for new and highly rated wind turbines. Therefore, FRC-based technology is considered for the electrical interface of new turbine-based hydrokinetic energy conversion concepts.

Chapter 4

Control of a hydrokinetic energy conversion system

This work was carried out in collaboration with Hydro-environmental research centre in Cardiff University. The turbines and the drive-train of the laboratory prototype were designed and constructed by Mr Stefan Runge of Cardiff University, School of Engineering, UK. The PhD. candidate designed and implemented the electrical subsystem of the hydrokinetic energy conversion system.

4.1 Introduction

In Chapter 3, a detailed modelling and Grid Code compliance study of wind turbines was presented. Similar studies extend to other renewable energy sources, such marine currents and river flows have been reported in the literature [77],[26]. Among these technologies, one of the most promising is based on taking advantage of the water flowing in man-made waterways. For this purpose, a system consisting of a set of two identical turbines has been proposed by [7].

To explore the capabilities of such a system, a laboratory prototype of two identical turbines driving a generator through a common shaft had been previously designed and constructed in the Cardiff University premises. The focus of this work was on the design of the electrical interface of this system for the power take-off and for control purposes.

In this chapter, a power electronics based electrical subsystem for the hydrokinetic energy conversion system was designed and tested. At first, the turbines, the drive-train and the generator previously developed were described. A no-load test and a resistive load test under varying water flow conditions followed. Then, the electrical subsystem for the hydrokinetic energy conversion system was introduced. To assess the performance of the proposed system, a test rig was set up. The suitability of the proposed configuration for the power take-off and the control of the hydrokinetic energy conversion system was highlighted. Finally, the complete laboratory prototype of the hydrokinetic energy conversion system (system of the turbines and the electrical interface) was tested.

4.2 Description of the hydrokinetic energy conversion system

4.2.1 General description of the system

The hydrokinetic energy conversion system is shown in Figure 4.1. It consists of two identical vertical-axis turbines driving a permanent magnet synchronous generator (PMSG) through a common shaft. The power conversion system consists of a diode-bridge rectifier, a dc-dc converter and a three-phase inverter for the connection to the grid. A voltage source converter (VSC) is used for the grid connection of the system and to keep the voltage V_b constant. With a fixed voltage V_b, the dc-dc converter is used to provide a variable voltage V_{dc} for the control of the generator. The anticipated full-scale hydrokinetic energy conversion system is rated at 10 kW.

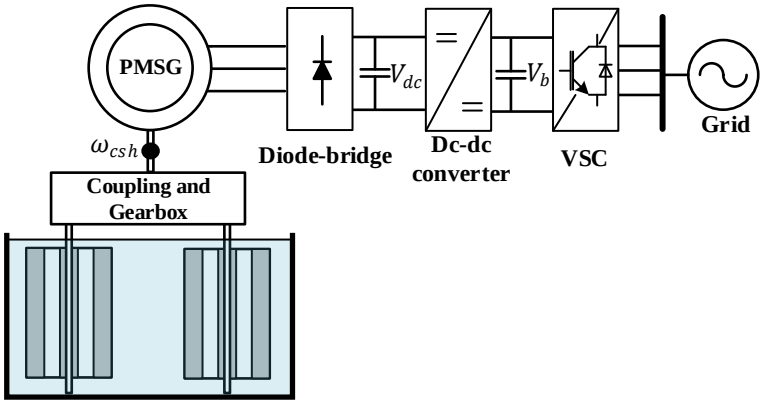

Figure 4.1. Configuration of the full-scale hydrokinetic energy conversion system.

4.2.2 Vertical-axis turbines

The use of vertical-axis turbines for the hydrokinetic energy conversion system for man-made waterways comes with some advantages against the use of horizontal axis turbines.

At first, the machining and manufacturing of vertical-axis turbines is not as delicate as in the case of horizontal-axis turbines. Consequently, vertical-axis turbines are simpler and less expensive option, especially for low power rated systems. In addition, the generator can be connected to one end of a vertical-axis turbine allowing its placement outside the water. Therefore, the insulation costs are avoided making the investment even more attractive [5].

Another advantage of the vertical-axis turbines against the horizontal-axis ones is their shape. The cylindrical shape of a vertical-axis turbine makes it more suitable for installation inside a rectangular channel similar to a rectilinear duct [5]. Furthermore,

in a shallow channel, the upper part of a turbine faces higher water velocity than the lower part. Vertical-axis turbines are reported to perform better under such conditions [110].

The turbines of the hydrokinetic energy conversion system had been previously designed in Cardiff University. They consist of three twisted blades and their design is similar to Gorlov type [17]. Small-scale turbines had been constructed for testing purposes in the Cardiff University premises. The laboratory-scale turbines are shown in Figure 4.2 and their dimensions are given in Appendix B.

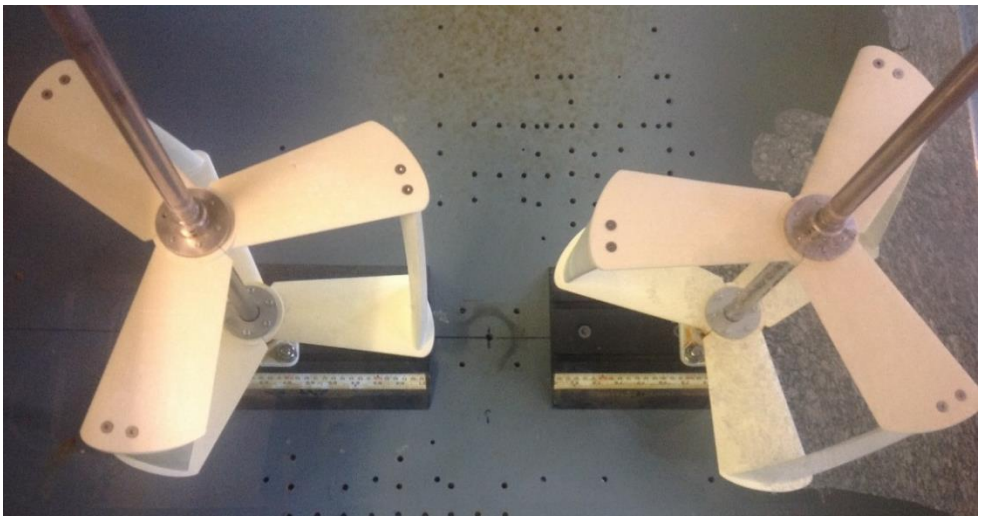

Figure 4.2. Small scale turbines used for laboratory tests.

The use of vertical-axis turbines comes with a ripple in the torque/speed. The frequency of this ripple is three times the rotational frequency of the turbines (3P). This ripple can be explained by the hydrodynamics of the vertical-axis turbines. The general mathematical expressions for the analysis of the hydrodynamic models for a Darrieus-type turbine are obtained based on [17]. According to Figure 4.3, the direction of the flow speed V_a is considered to be axial. It is also assumed that the flow speed is uniform and constant and the analysis is done in two dimensions space.

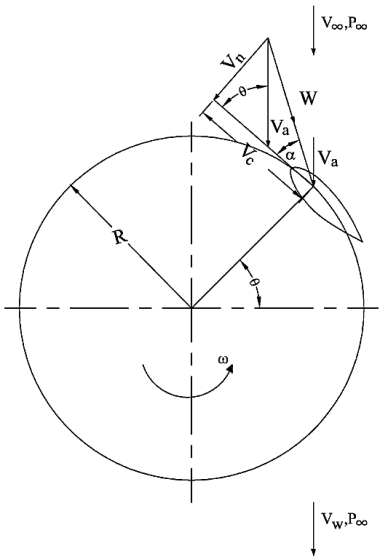

Figure 4.3. Flow velocities of straight-bladed Darrieus-type turbine [17].

Regarding the velocity of the blade, there are two components: the chordal velocity component V_c and the normal velocity component V_n. The equations for the derivation of these velocity components are given as

$$V_c = \mathrm{R}\omega + V_a \cos\theta \tag{4.1}$$

$$V_n = V_a \sin\theta \tag{4.2}$$

where ω is the rotational speed, R is the radius of the turbine and θ is the azimuth angle. As it can be seen in Figure 4.3, the angle of attack α can be expressed as

$$a = \tan^{-1}\left(\frac{V_a \sin\theta}{R\omega + V_a \cos\theta}\right) \tag{4.3}$$

Using the definition of the tip speed ratio $\lambda = \omega R/V_a$, (4.3) becomes

$$a = \tan^{-1}\left(\frac{\sin\theta}{\lambda + \cos\theta}\right) \tag{4.4}$$

If the blade is considered to be pitched by an angle γ, the angle of attack α becomes

$$a = \tan^{-1}\left(\frac{\sin\theta}{\lambda + \cos\theta}\right) - \gamma \tag{4.5}$$

Fig. 2 shows the angle of attack α against the angle of rotation θ for one revolution of a single blade of a Darrieus-type turbine ($\lambda = 3, \gamma = 6^o$).

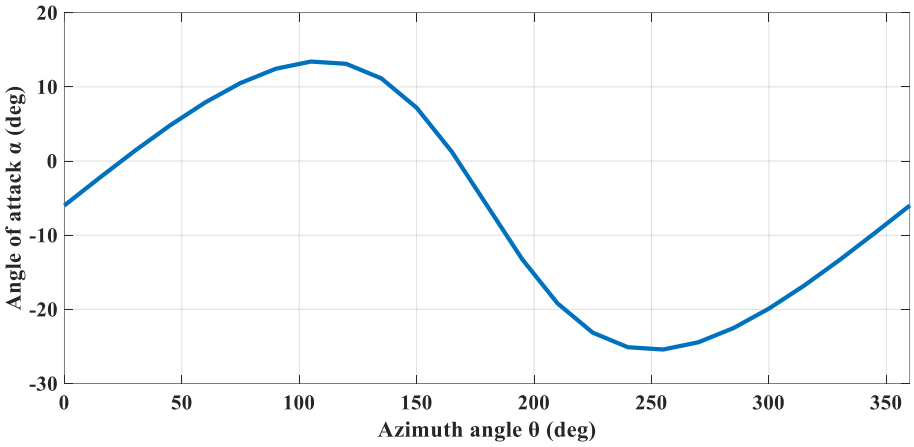

Figure 4.4. Angle of attack α for one revolution of the turbine.

According to Figure 4.3, the relative flow velocity (W) can be expressed in terms of V_c and V_n as

$$W = \sqrt{{V_c}^2 + {V_n}^2} \tag{4.6}$$

Figure 4.5 shows the forces applied on a single blade. The *lift force L* is perpendicular to the flow and is due to the pressure difference between the top and the bottom of the blade. The *drag force D* is in the direction of the flow; it is basically the resistance of the blade to the flow.

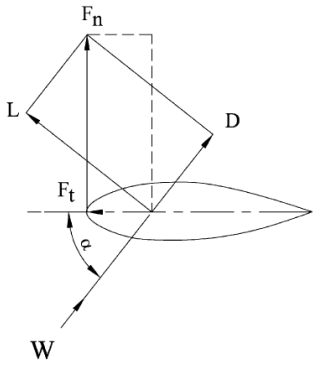

Figure 4.5. Diagram of forces on a single blade [17].

The lift and drag forces can be analysed to their normal and tangential coefficients. The difference between the tangential components of lift and drag forces is the tangential force coefficient C_t, and the difference between the normal components of the lift and the drag force is the normal force coefficient C_n. The mathematical equations for the derivation of C_t and C_n are

$$C_t = C_l \sin a - C_d \cos a \tag{4.7}$$

$$C_n = C_l \cos a + C_d \sin a \tag{4.8}$$

where, C_l and C_d are the lift and drag coefficients respectively.

Given the tangential and the normal force coefficients C_t and C_n, the tangential and normal forces can be defined as

$$F_t = C_t \frac{1}{2} \rho C H W^2 \tag{4.9}$$

$$F_n = C_n \frac{1}{2} \rho C H W^2 \tag{4.10}$$

where, ρ is the water density, C is the blade cord and H is the height of the turbine. The average tangential force on one blade can be expressed as

$$F_{t,av} = \frac{1}{2\pi} \int_0^{2\pi} F_t(\theta) d\theta. \tag{4.11}$$

Since the tangential force $F_{t.av}$ is the predominant component, the total torque for one blade can be expressed as

$$T = F_{t,av} R \tag{4.12}$$

Figure 4.6 shows the torque acting on a single blade of a vertical axis turbine and Figure 4.7 shows the total torque considering all the 3 blades of the turbine. The laboratory-scale turbines were used to demonstrate the agreement of the measurements with the theoretical curves.

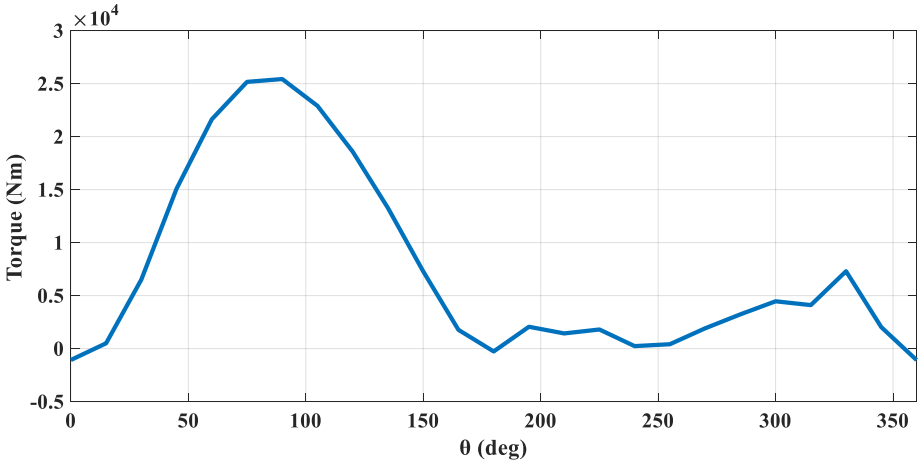

Figure 4.6. Torque against the angle of rotation considering one blade for one revolution.

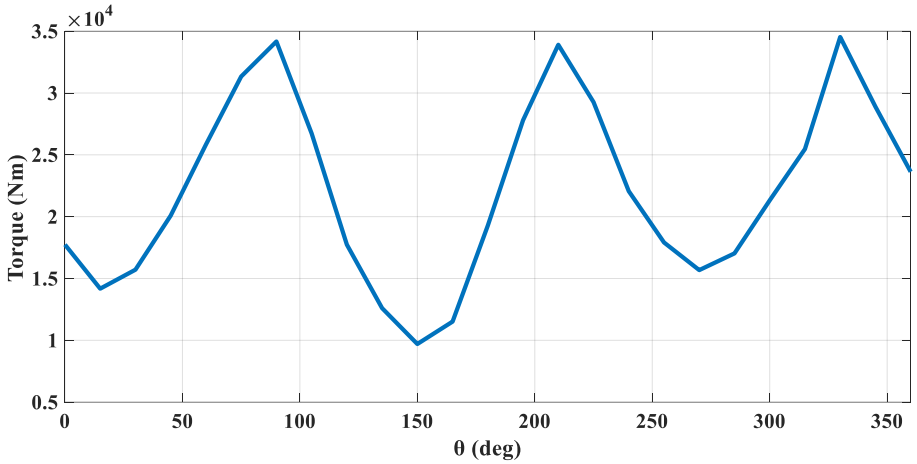

Figure 4.7. Torque against angle of rotation considering three blades for one revolution.

The measurements taken using the experimental set up are shown in Figure 4.8. The laboratory scale turbines shown in Figure 4.2 were used. It is shown that the measured torque of the turbine for one revolution follows the general curve derived from the equations and shown in Figure 4.7. The torque is measured for one revolution of the common shaft (details in Section 4.2.3) where the torque transducer was placed.

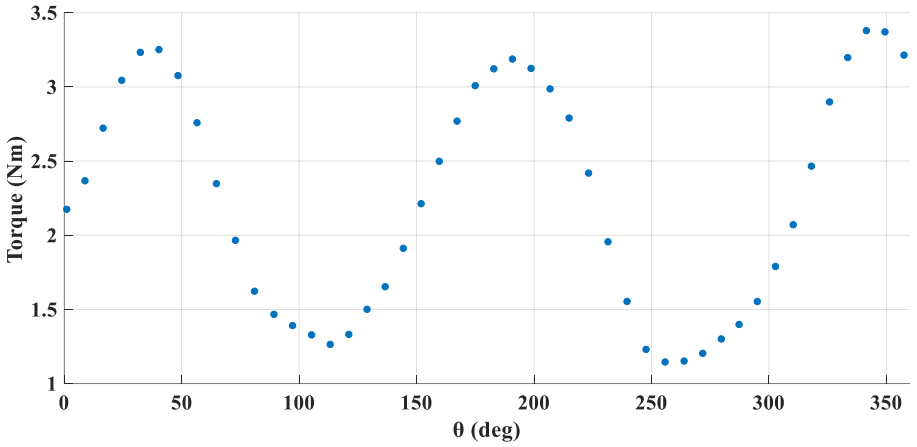

Figure 4.8. Torque of the system of vertical-axis turbines of the laboratory prototype for one revolution of the common shaft.

4.2.3 Drive-train and gearing

A drive-train had been previously designed and was used to transfer the rotation of the two turbines into the rotation of a common shaft. As shown in Figure 4.9, two identical pulleys were put on the rotor of each turbine. A timing belt was used to connect the two separate pulleys with a third pulley fixed onto another rotor. This way, the synchronised counter-rotation of the turbines was ensured. The common shaft was used to drive a generator. The ratio between the radius of the pulleys of each turbine

and the radius of the pulley of the common shaft defined the gearing provided by the drive-train.

4.2.4 Generator

A PMSG was used to convert the mechanical power provided by the common shaft into electrical power. The rated speed of the generator was 200 rpm and the rated power was 200 W. The specifications of the PMSG are given in Appendix B. The drive-train and the generator used for the tests in the laboratory are shown in Figure 4.9.

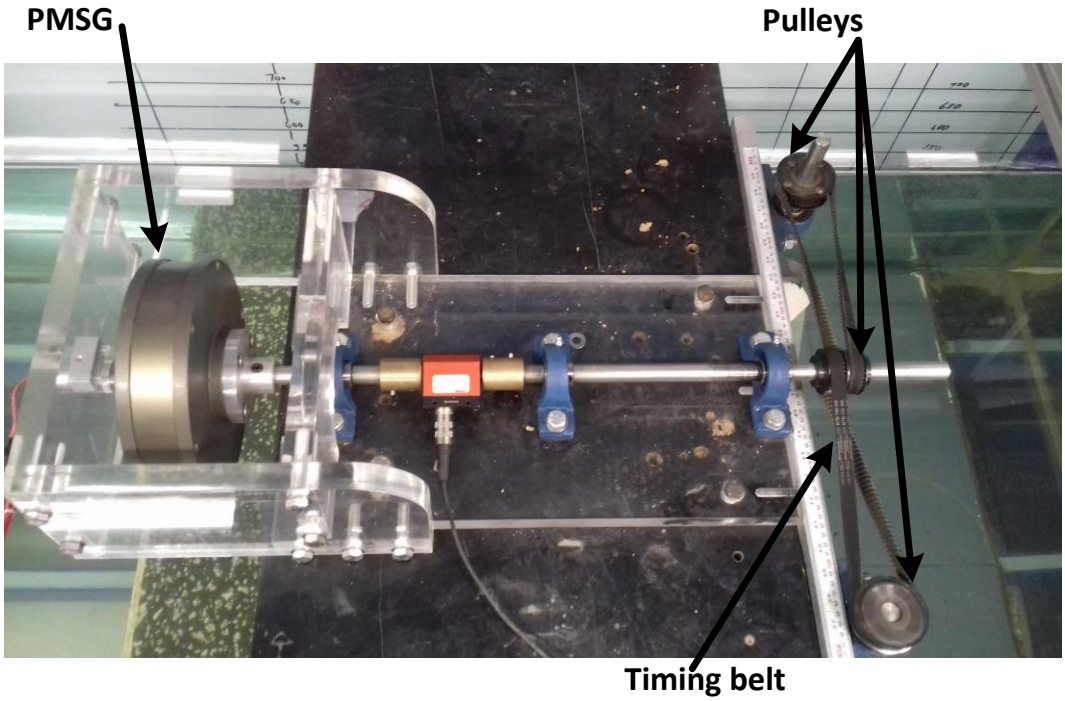

Figure 4.9. Drive-train and PMSG of the test system.

4.2.5 Diode rectifier

The output of the generator was connected to an uncontrolled rectifier. The uncontrolled rectifier was a diode-bridge, as shown in Figure 4.10.

With the use of a three-phase diode-bridge, the operation of the rectifier is uni-directional; power can only flow from the ac side to the dc side of the rectifier. Unavoidably, current distortion occurred, but the power level is low and its effect on the power quality is of minor importance. In contrast, it is a reliable solution to reduce the cost and the complexity of the hydrokinetic energy conversion system.

To analyse the diode bridge rectifier, it is assumed that there is no inductance in the ac side and instead of a load, a constant dc current I_d is connected to the dc side of the rectifier, as shown in Figure 4.10 [54]. In the same figure, it can be seen that there are two groups of diodes: the top and the bottom group. The current I_d flows through one diode from the top group and one from the bottom group. When the anode of a diode of the top group reaches its highest potential, it conducts. The rest diodes of the same group are reversed biased. Similarly, when the cathode of a diode is at its lowest potential, the diode conducts and the rest diodes of the bottom group become reversed biased [54].

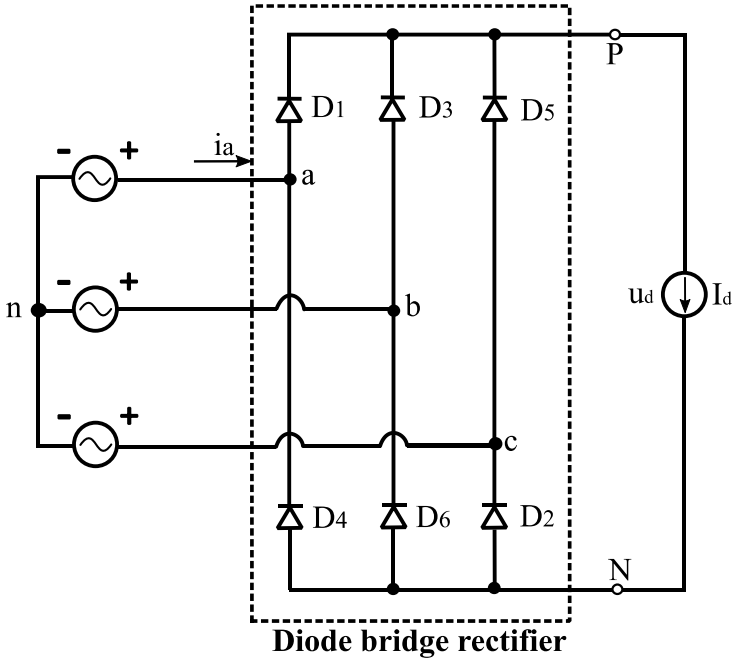

Figure 4.10. Diode-bridge rectifier with constant dc current [54].

Figure 4.11(a) shows the voltage waveforms in the circuits of Figure 4.10. u_{Pn} is the voltage at the positive terminal *P* with respect to the ac voltage neutral point *n* and u_{Nn} is the voltage at the negative terminal *N*. The dc side voltage of the rectifier is

$$u_d = u_{Pn} - u_{Nn} \tag{4.13}$$

Figure 4.11(b) shows the waveform of u_d. It is shown that there are six segments per cycle of the line frequency and each segment is one of the six line-line combinations. Due to this ripple in the dc voltage-and thus the dc current- this rectifier is often called a six-pulse rectifier. As shown in Figure 4.11(c), each diode conducts for 120^o [54].

To obtain the average value of the output dc voltage, one of the six segments is considered and the average over 60^o is obtained. The time origin t=0 is chosen when the line-line voltage u_{ab} is at its maximum. Thus,

$$u_d = u_{ab} = \sqrt{2}V_{LL}cos\omega t, \qquad -\frac{\pi}{6} < \omega t < \frac{\pi}{6} \tag{4.14}$$

where $V_{LL}$is the rms value of the line-line voltages.

The area A in Figure 4.11(b) is given by

$$A = \int_{-\frac{\pi}{6}}^{\frac{\pi}{6}} \sqrt{2}V_{LL}cos\omega t \; d(\omega t) \tag{4.15}$$

Therefore, the rms value of the voltage u_d is given by

$$V_d = \frac{1}{\frac{\pi}{3}} \int_{-\frac{\pi}{6}}^{\frac{\pi}{6}} \sqrt{2}V_{LL}cos\omega t \; d(\omega t) = 1.35V_{LL} \tag{4.16}$$

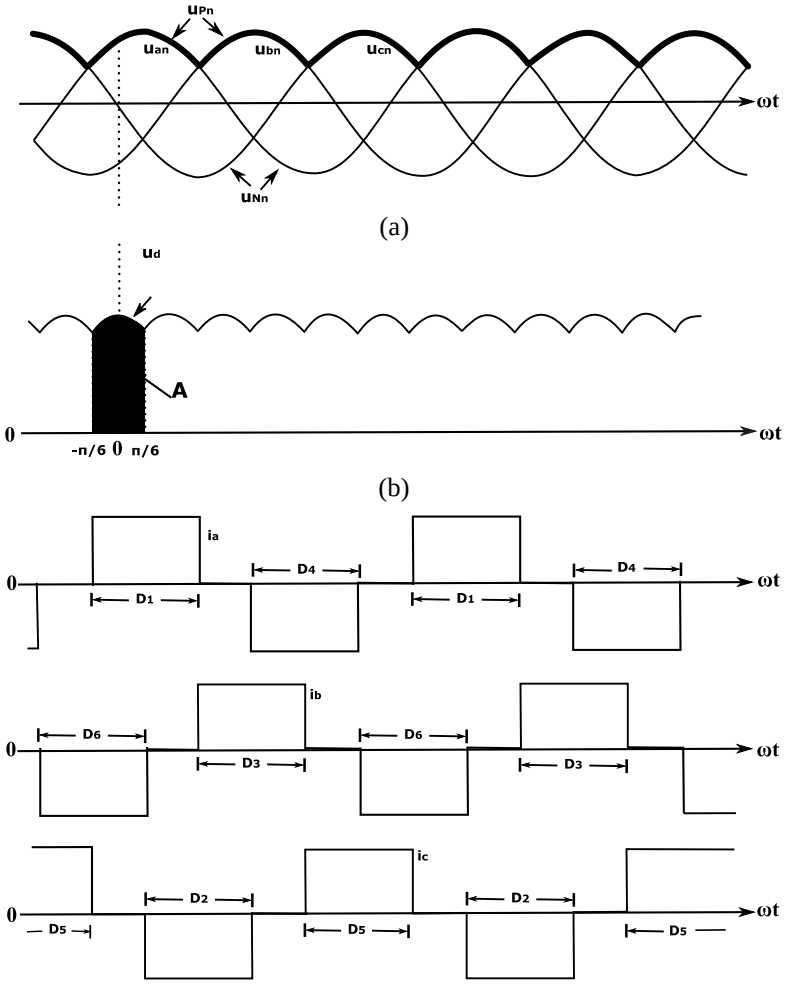

Figure 4.11. Waveforms of the voltages and the current of Figure 4.10 [54].

If the current source is replaced by an ohmic load, the voltage and current waveforms will be identical. However, the current waveforms will not have a flat top [54].

The circuit of the diode rectifier shown in Figure 4.10 was simulated. Instead of an ideal ac source, the PMSG described in Section 4.2.4 was used and instead of the dc current source, a resistive load at the dc side was used, as shown in Figure 4.12. Simscape blocks were used to simulate the system in MATLAB/Simulink. The speed of the generator was set to 17.5 rad/sec. The results are shown in Figure 4.13.

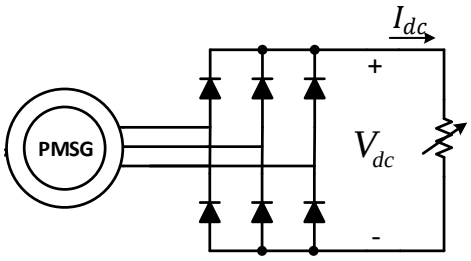

Figure 4.12. System modelled and simulated to demonstrate the 6f ripple due to the diode-bridge rectifier

It is shown that there is a ripple in the dc voltage and the dc current due to the uncontrolled rectifier. The rotational speed was set to 17.5 rad/sec. Thus, considering 8 pole pairs of the generator, the electrical frequency of the generator was $f_e = 22.28\,Hz$. The oscillation of the dc voltage, the dc current and the torque is $T_{osc} \approx 0.007$sec and thus, $f_{osc} \approx 133.7Hz = 6f_e$. Therefore, the frequency of the ripple observed after the simulation of the system shows good agreement with what was theoretically expected.

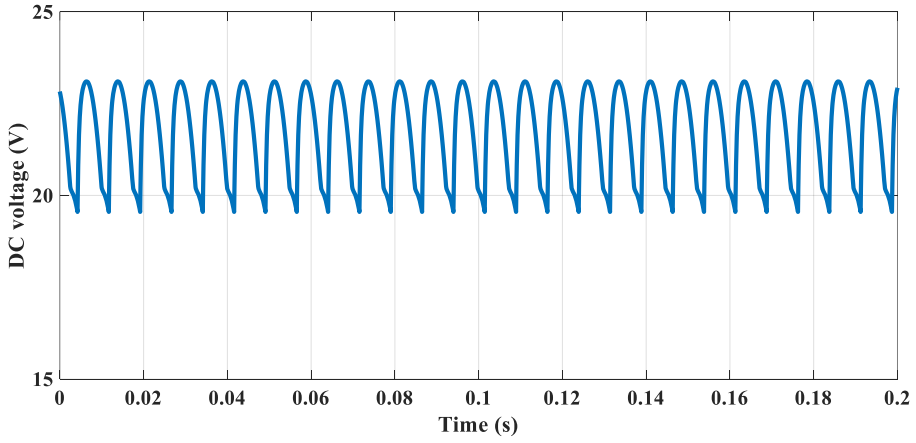

(a)

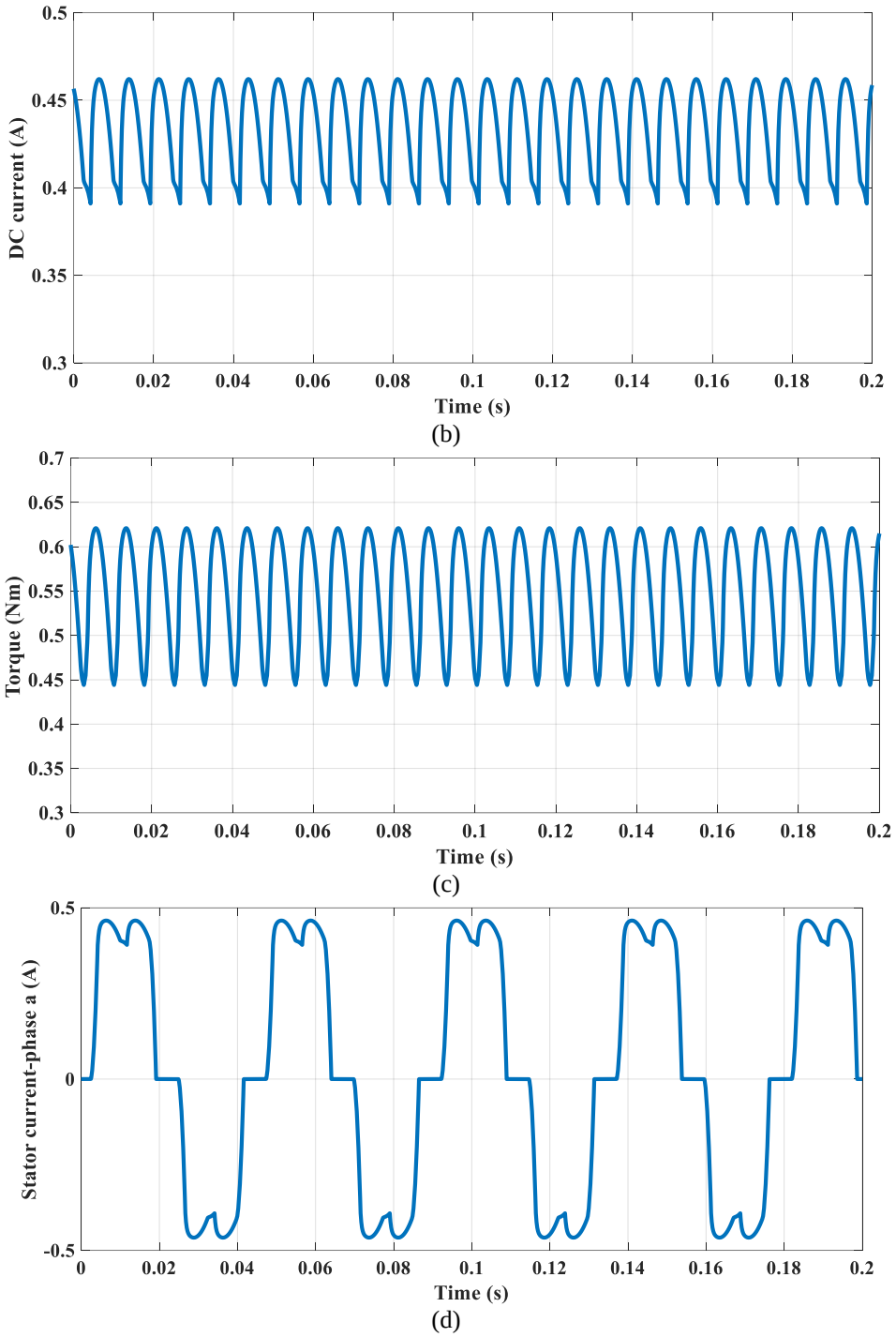

Figure 4.13. Diode bridge rectifier connected to a PMSG: (a) dc voltage, (b) dc current, (c) torque of the generator and (d) phase a stator current.

4.2.6 No-load test of the generator

The turbines were put into an 18 m flume filled with water. The water level was 500 mm and the distance between the shafts of the two turbines was 540 mm. The speed of the water of the flume was varied using a pump controlled remotely from a control panel. Four different water speeds were achieved: 0.72 m/s, 0.85 m/s, 0.98 m/s and 1.09 m/s.

At first, the hydrokinetic energy conversion system was tested to obtain the no-load characteristic curve of the system. To achieve this, the set-up shown in Figure 4.14 was used. For all the tests, pulleys providing a gearing ratio of 4:3 were selected, so that the speed of the common shaft did not exceed the rated speed of the generator.

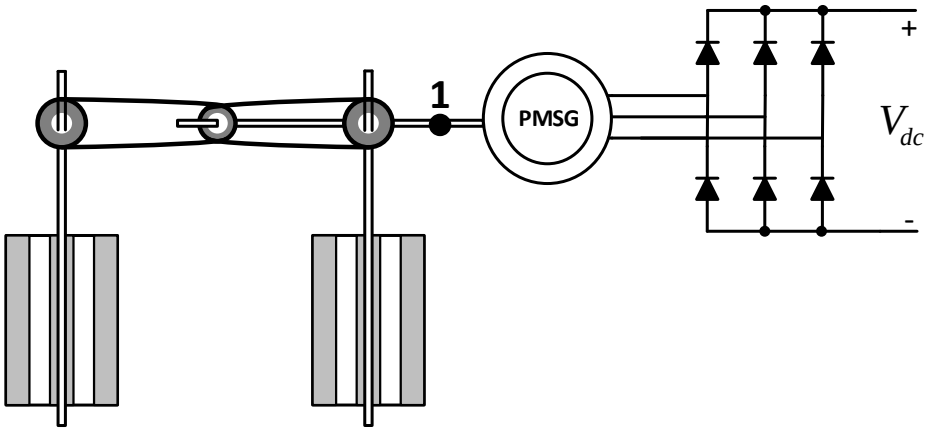

Figure 4.14. Experimental set-up for the no-load test.

For different water speeds, torque and speed measurements were taken from the common shaft (Point 1 in Figure 4.14) and the voltage at the dc side of the rectifier, V_{dc}, was measured. For the measurement of the torque and the rotational speed, LabJack U6-PRO was used. LabJack U6-PRO is a device combining a torque transducer and a speed encoder [111]. For the measurement of the dc voltage of the rectifier an oscilloscope was used.

The common shaft of the turbines was attached to the rotor of the PMSG, and therefore the rotational speed of the common shaft was identical with the rotational speed of the generator. In addition, as shown in Figure 4.14, V_{dc} was basically the voltage at the generator terminal. The results are shown in Figure 4.15.

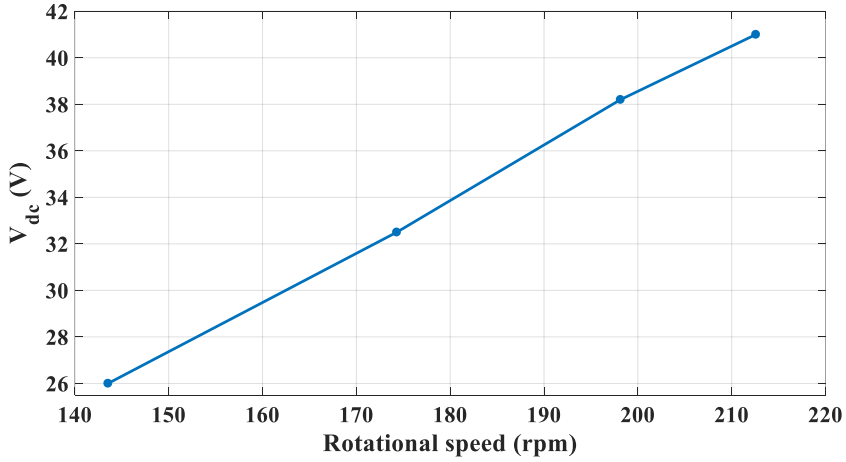

Figure 4.15. No-load characteristic curve of the system.

The experimental results shown in Figure 4.15 show that there is a linear relationship between the rotational speed of the common shaft and the voltage at the dc side of the rectifier. This was expected, since there is a linear relationship between the rotational speed and the terminal voltage of the PMSG [95].

4.2.7 Characteristic curves of the system using a resistive load

A resistive load was connected at the dc side of the rectifier, as shown in Figure 4.16. For different water speeds, the resistive load was varied until the turbines reached their stall condition. Mechanical and electrical measurements were taken so that the characteristic curve of the system is obtained.

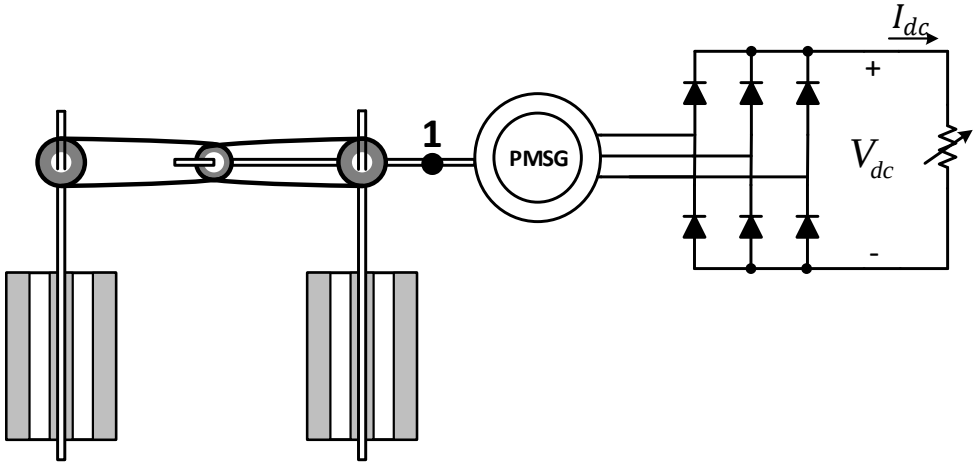

Figure 4.16. Experimental set-up for the test using a resistive load.

Torque and speed measurements were taken from the common shaft (Point 1, Figure 4.17 The frequency of the measurements was 100 Hz. An example is shown in Figure 4.17(a), where the toque and the speed during one revolution of the common shaft for a water speed of 0.72 m/s and a resistive load of 10 Ω are shown. **Error! Reference s ource not found.** 4.17(b), shows the measurements for the torque and the speed of the common shaft for a time interval of one minute. Faulty measurements that deviate extremely from the mean value were isolated.

The mechanical power was calculated using

$$P_m = T_{csh} \cdot \omega_{csh} \tag{4.17}$$

where T_{csh} is the torque (Nm) and ω_{csh} is the rotational speed (rad/s), both measured at the common shaft.

For the calculation of the mechanical power, P_m, torque and speed were obtained from the mean values of the measurements provided for a time interval of one minute.

The voltage across and the current flowing towards the resistor were measured, too. The mean values of the voltage and the current were taken using an oscilloscope. The electrical power consumed by the resistive load was calculated using

$$P_R = V_{dc} \cdot I_{dc} \tag{4.18}$$

Both the mechanical and the electrical measurements for this test are given in Appendix B.

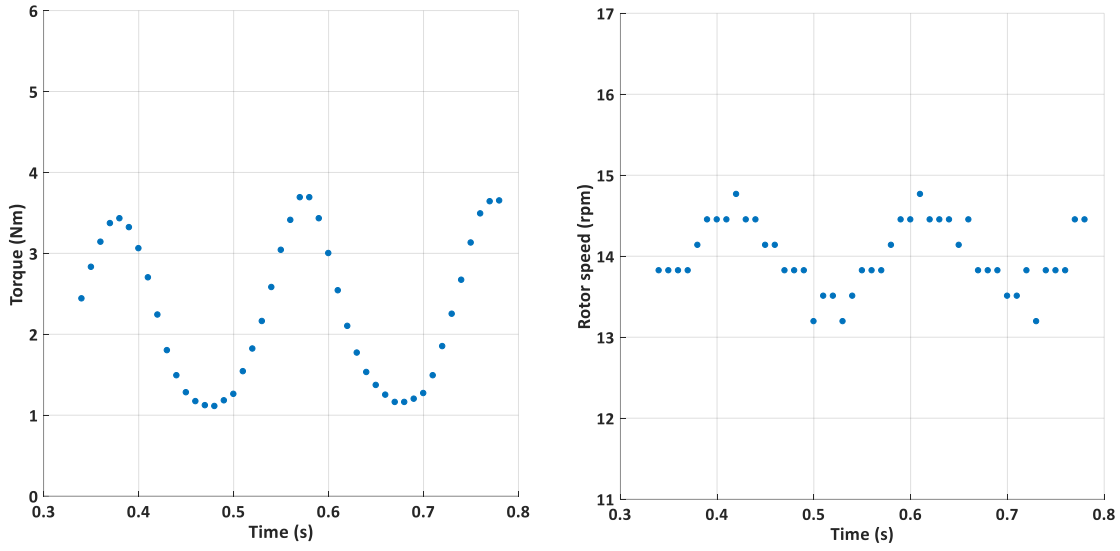

(a)

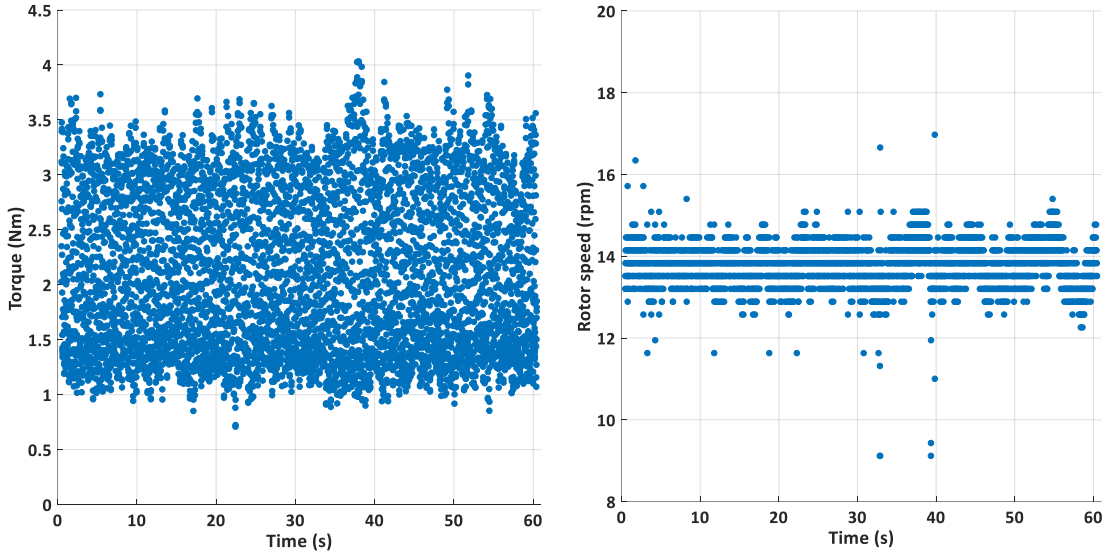

(b)

Figure 4.17. Torque and speed measurements for a resistive load of 10 Ω: (a) during one revolution of the synchronised turbines and (b) for a time interval of one minute.

Assuming that the power available in the flowing water around the turbines is the summation of the power corresponding to each of the turbines (according to the actuator disc theory), the available power in the water was calculated using

$$P_{fl} = \frac{1}{2} \cdot \rho \cdot 2A \cdot {v_{fl}}^3 \tag{4.19}$$

where ρ is the water density (997 kg/m^3), A is the swept area of each turbine and v_{fl} is the water speed.

The power coefficient C_p of the system was calculated using

$$C_p = \frac{P_m}{P_{fl}} \tag{4.20}$$

The tip speed ratio for this system was calculated, referring to one of the two turbines, using

$$\lambda = \frac{\omega_t R}{v_{fl}} \tag{4.21}$$

where ω_t is the rotational speed and R is the radius of each turbine.

Using the gearing ratio provided by the system of the timing belt and the pulleys, the rotational speed of each turbine was calculated using

$$\omega_{csh} = \frac{3}{4}\omega_t \tag{4.22}$$

The characteristic ($C_p - \lambda$) curve of the system using a resistive load is shown in Figure 4.18. It was observed that the turbines stalled shortly after the MPP for every water speed was reached.

Figure 4.19 shows the electrical power produced by the test rig shown in Figure 4.16, for a variable resistive load under different water speeds. It was evidenced that for higher water speeds, the maximum power was produced for higher rotational speeds.

Although the general form of the curves is close to what was theoretically expected, it was noticed that for operational points below the MPP, the turbines stalled. This characteristic is not seen in the $C_p - \lambda$ curves of different types of wind turbines and indicates that a more suitable test should take place.

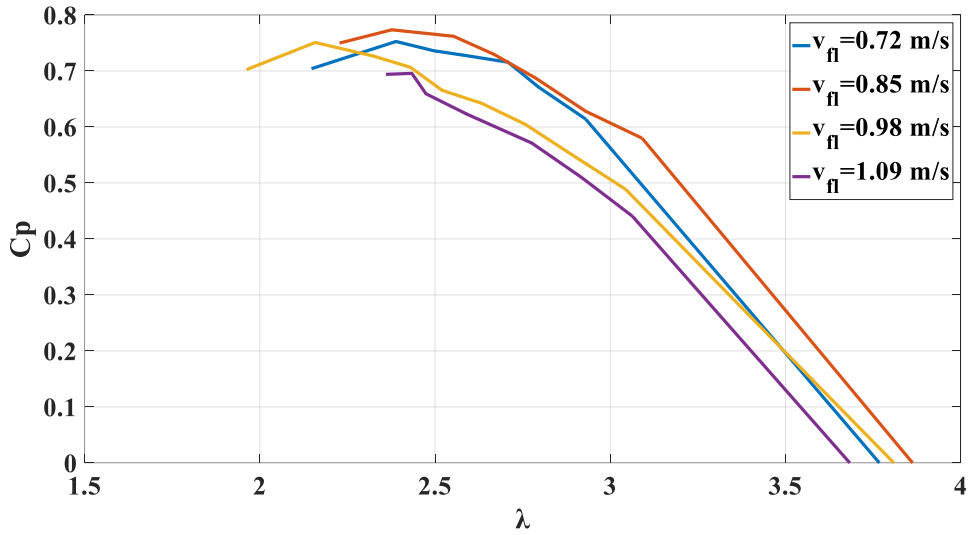

Figure 4.18. The $C_p - \lambda$ curve obtained using a resistive load.

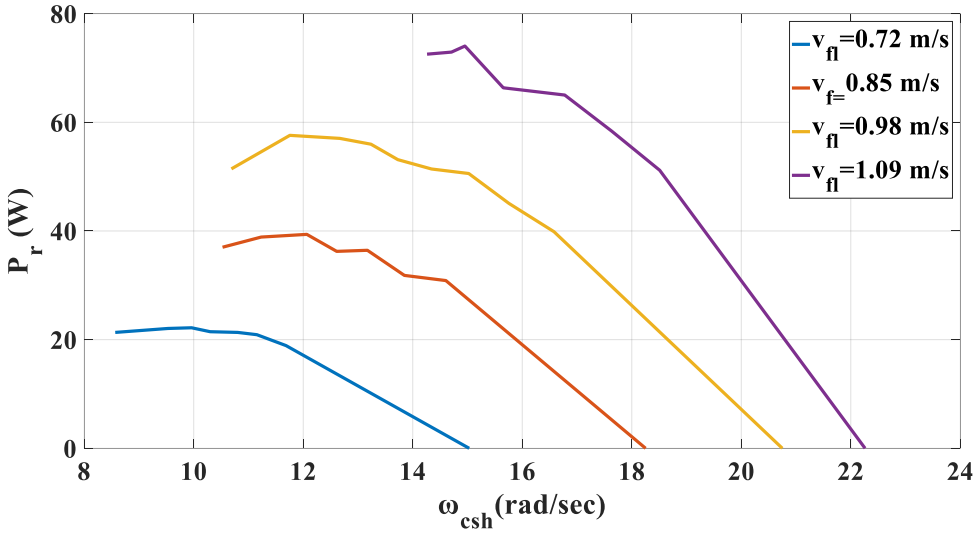

Figure 4.19. Electrical power produced against the rotational speed of the common shaft obtained using a resistive load.

4.3 A dc-dc converter for the control of the hydrokinetic energy conversion system

A dc-dc converter was selected to control the terminal voltage of the generator and batteries were used to store the energy produced as shown in Figure 4.20. The dc-dc converter was purchased, tested and finally connected between the uncontrolled rectifier and the batteries. This way, the voltage at the side of the rectifier, V_{dc}, was variable allowing the control of the generator and the voltage at the side of the batteries, V_b, was fixed. Details of the batteries and the dc-dc converter are given in Appendix B.

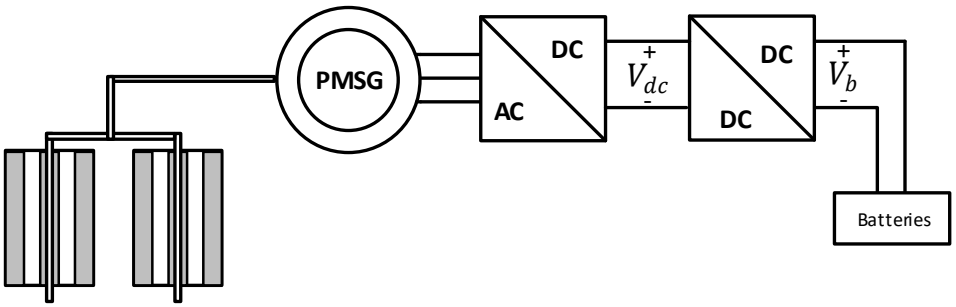

Figure 4.20. A dc-dc converter and batteries for the electrical interface of the hydrokinetic energy conversion system.

Among the available options for dc-dc conversion, an interleaved buck-boost converter was selected, as shown in Figure 4.21. For the continuous conduction mode of the buck-boost converter, the ratio between the voltage V_{dc} and the voltage V_b is given by [54]

$$\frac{V_b}{V_{dc}} = \frac{D}{1-D} \tag{4.23}$$

From (4.23), for buck-boost operation, the voltage across the rectifier gets either higher or lower from the voltage level across the battery terminals, depending on the duty cycle D. Consequently, in the final application, the voltage across the terminals of the PMSG-and thus the rotational speed of the generator- can be varied between the widest possible range. This is the main reason the buck-boost converter was selected.

Interleaved operation is achieved by connecting two or more dc-dc converters in parallel. For this application, two parallel connected buck-boost converters were used, as shown in Figure 4.21. The two switches S_1 and S_2 are operated with a phase shift of 180°. The advantage of this configuration is the current ripple cancellation, the reduction of the size of the inductors and the improved dynamic response [112].

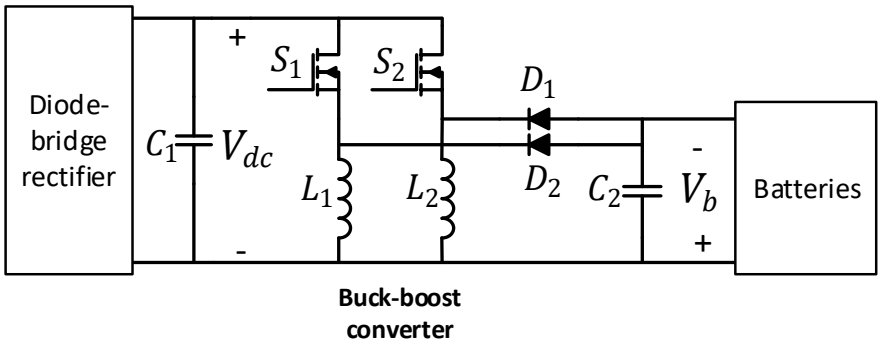

Figure 4.21. Interleaved buck-boost converter.

The dc-dc converter was purchased from Texas Instruments. It was part of the demonstration board for an HV Solar application. The converter was a boost converter. The terminals of the boost converter were rewired properly to form a buck-boost converter, as shown in Figure 4.22. Two 1000 μF capacitors were used, too. Specifications of the converter are included on the diagram given in Appendix D. The diagram can be found in [113].

The TMS320f28035 Piccolo microprocessor was used for the control of the converter. The communication between the computer and the microprocessor was achieved with the use of a USB cable. Code Composer Studio, a piece of software provided by Texas Instruments, was used as a computer interface. The code used in Code Composer Studio was generated using MATLAB/Simulink blocks.

The dc-dc converter was fixed at the bottom of an enclosure along with a diode-bridge rectifier and two aluminium electrolytic capacitors purchased for testing purposes, as shown in Figure 4.22. External power supply of 5 V was provided to the digital signal processing (DSP) card for the operation of the converter.

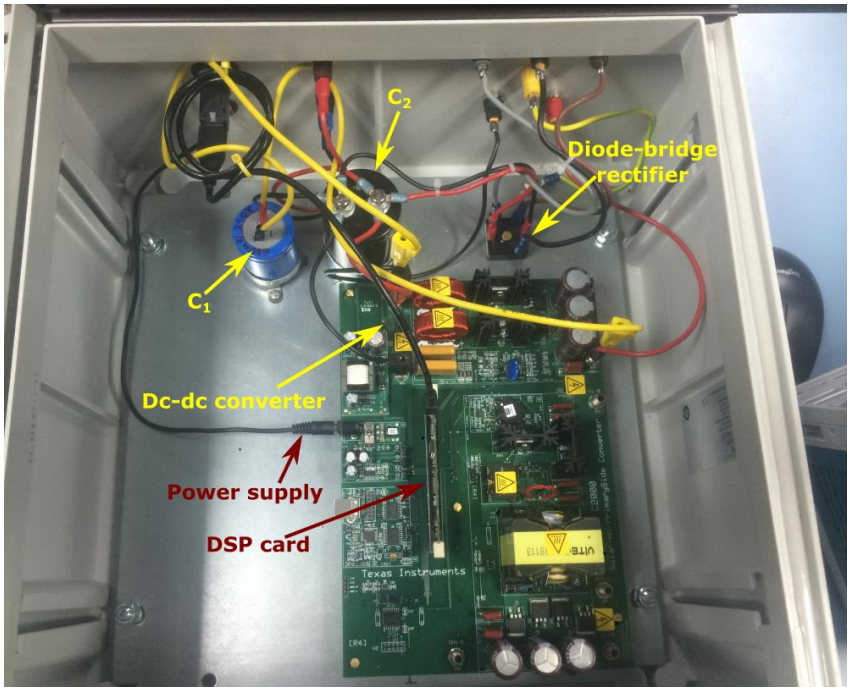

Figure 4.22. Diode-bridge rectifier, dc-dc converter and capacitors fixed on the bottom of an enclosure.

4.3.1 PWM generation

Using the MATLAB/Simulink interface, a code was generated for the implementation of the two PWM signals for the operation of the interleaved dc-dc converter. An oscilloscope was used to measure the PWM signals on the demonstration board. The PWM signals for a duty cycle of 0.4 are shown in Figure 4.23. It is shown that there is a phase difference between the two PWM signals (cyan and blue curve). The time period of both signals was 10 μs and therefore, the switching frequency was 100 kHz.

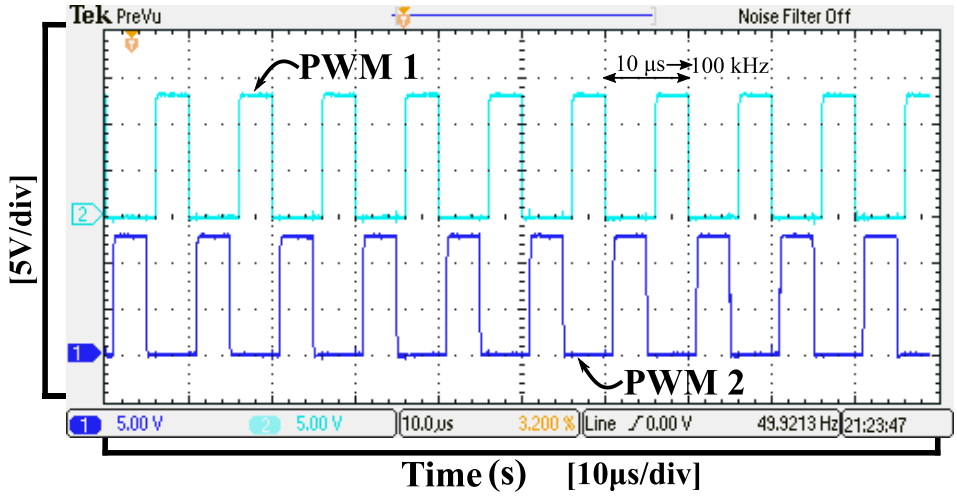

Figure 4.23.. PWM signals for a duty cycle of 0.4.

4.3.2 Analog-to-digital conversion

With the analog-to-digital conversion (ADC), the measured voltages and currents are converted into digital signals. A voltage divider and an operational amplifier-based circuit are used to convert the voltage and the current into low voltage signals. The maximum value for these signals was 3.3V. The low voltage signals are then used as an input to the channels of a microprocessor. Then, the measurements are transmitted as digital data to the computer through a USB connection. The digital signals are used as an input to the Code Composer Studio for control and monitoring purposes.

Figure 4.24 shows how the real values of the voltage and the current were obtained in MATLAB/Simulink. Blocks provided by Texas Instruments were used to obtain the digital value of the voltage and the current. A calibration followed and the offset values (C) were subtracted from the values provided by the Texas Instruments blocks. The output of this stage was multiplied by a constant factor K_c, so that the actual values for the voltage and the current are obtained. Memory blocks were, then, used to store the measured values.

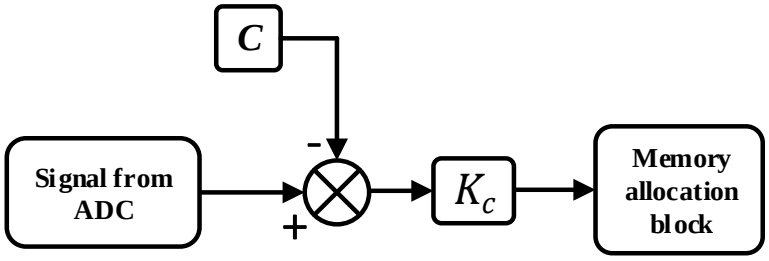

Figure 4.24. Actual values calculated using values from the analog-to-digital conversion.

4.3.3 A laboratory test-rig for the test of the dc-dc converter

Prior to the final application of the converter for the control and the characterisation of the hydrokinetic energy, a test to assess the performance of the converter and its suitability for the final application took place. For this purpose, the test rig shown in Figure 4.25 was set up.

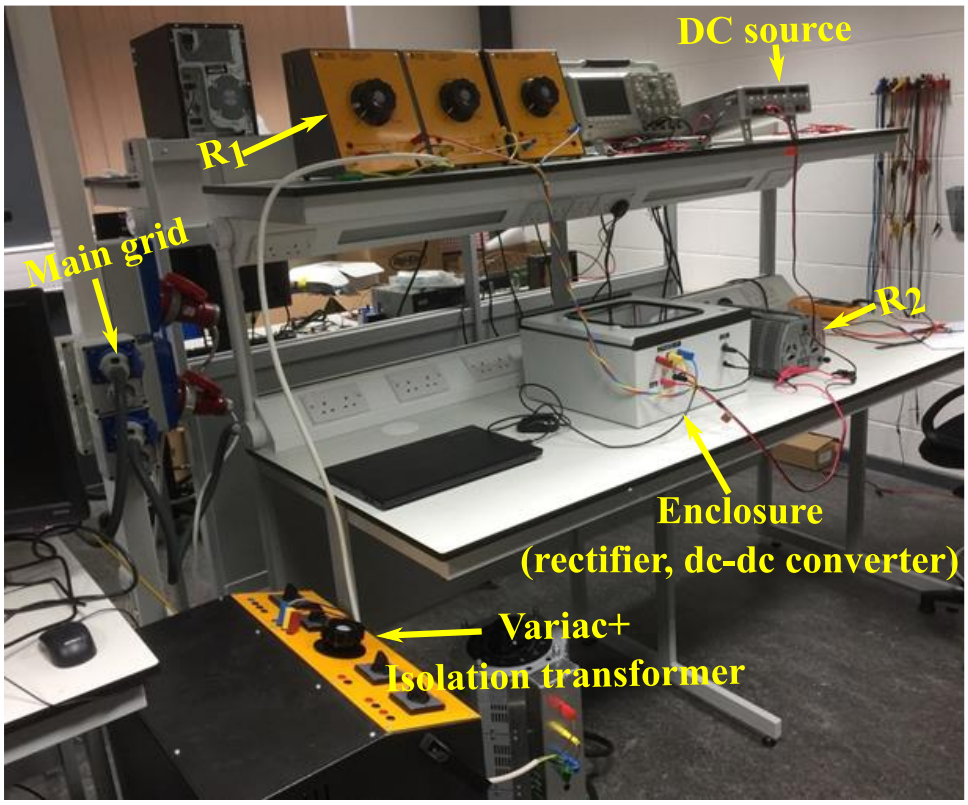

Figure 4.25. Laboratory test-rig for the test of the dc-dc converter.

Figure 4.26 shows the configuration of the test rig. An autotransformer combined with an isolation transformer was connected to the mains to step down the voltage. The output of the autotransformer was connected through resistors to a rectifier to obtain the dc voltage. The input of the dc-dc (buck-boost) converter was connected to the dc side of the rectifier and the output was connected in parallel with a resistor and a dc

source. The dc source in parallel with a resistor was used to represent the batteries proposed for the hydrokinetic energy conversion system.

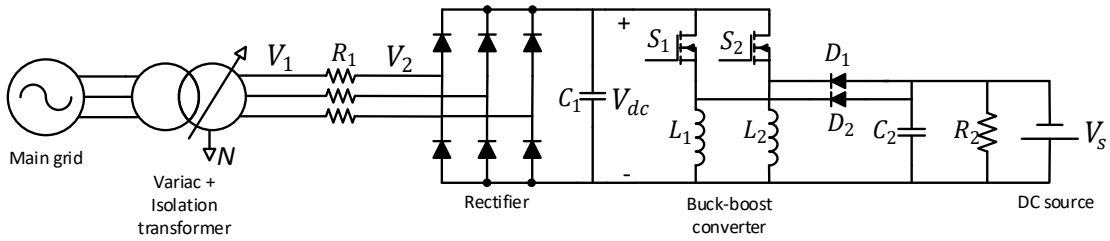

Figure 4.26. Configuration of the test rig for the test of the dc-dc converter.

The voltage at the secondary winding of the autotransformer, V_1, was kept constant. The voltage V_{dc}, and thus, the voltage V_2 was changed by varying the duty cycle of the converter.

The power flow at the point just before the rectifier (voltage V_2) is calculated using [114]

$$P = 3\frac{V_1 - V_2}{R_1}V_2 \tag{4.24}$$

Considering that $V_{LL} = \sqrt{3}V_{LN}$ and using (4.6), (4.24) becomes

$$P = 3\frac{V_1 - \frac{V_{dc}}{2.34}}{R_1}V_{dc} \tag{4.25}$$

For a variable voltage V_{dc} and a resistance $R_1 = 3.6\ \Omega$, the power curves of the system of Figure 4.16**Error! Reference source not found.** for a fixed line-neutral rms v oltage V_1 of 14V and 18V are calculated using (4.9) and are shown in Figure 4.27.

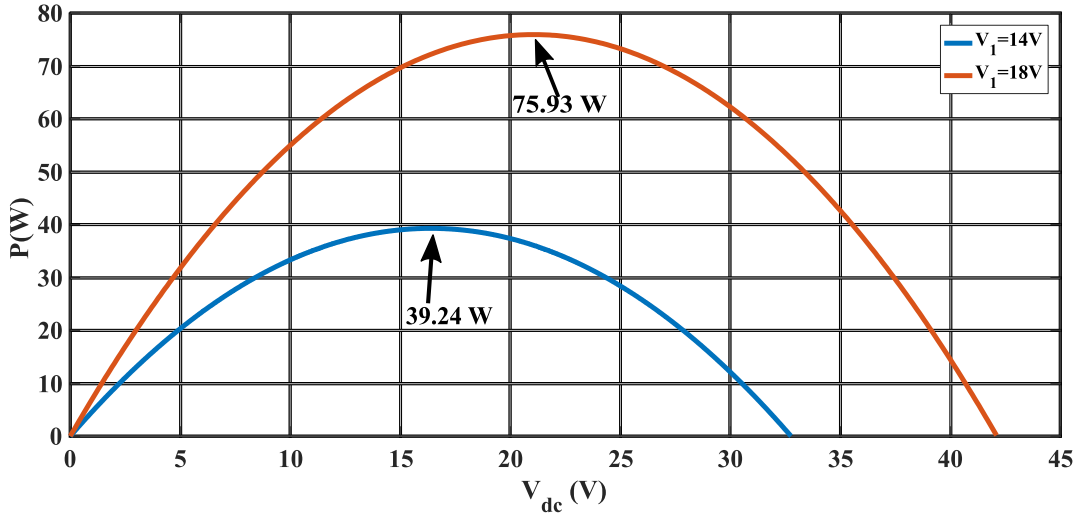

Figure 4.27. Calculated power curves for the test rig.

To validate the calculations graphically presented in Figure 4.27, two experimental tests took place. At first, the autotransformer was regulated so that the voltage V_1 was set to ≅ 14 V. The duty cycle of the converter was varied manually using the Code Composer Studio and different values for the voltage V_{dc} and thus, the voltage V_2 were obtained as shown in Figure 4.28**Error! Reference source not found.**(a). The r esulting power flowing towards the resistor R_2 was measured and is shown in Figure 4.28(b).

The same procedure was followed for a fixed voltage V_1 ≅ 18 V. The results are shown in Figure 4.29. Figure 4.29 shows that for V_1 ≅ 14 V, the maximum power flow (≅ 36 W) occurred when V_{dc} ≅ 17.5 V → V_2 ≅ 6.5 V. **Error! Reference source not f ound.** shows that for V_1 ≅ 18 V, the maximum power (≅ 68 W) was achieved when V_{dc} ≅ 23 V → V_2 ≅ 10 V.

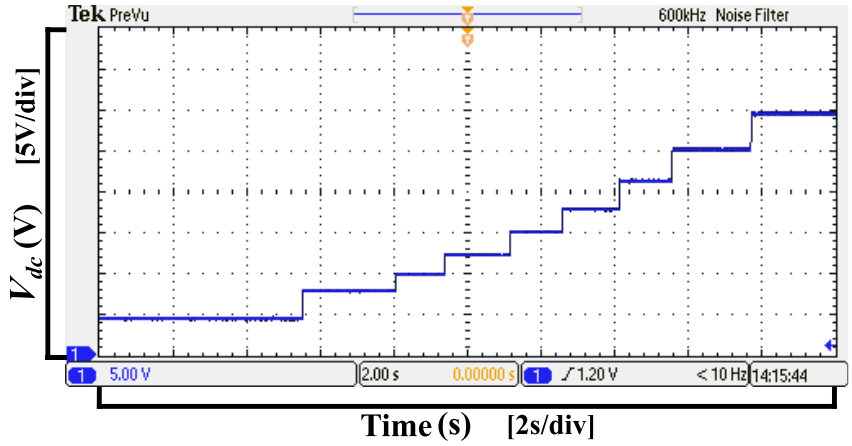

(a)

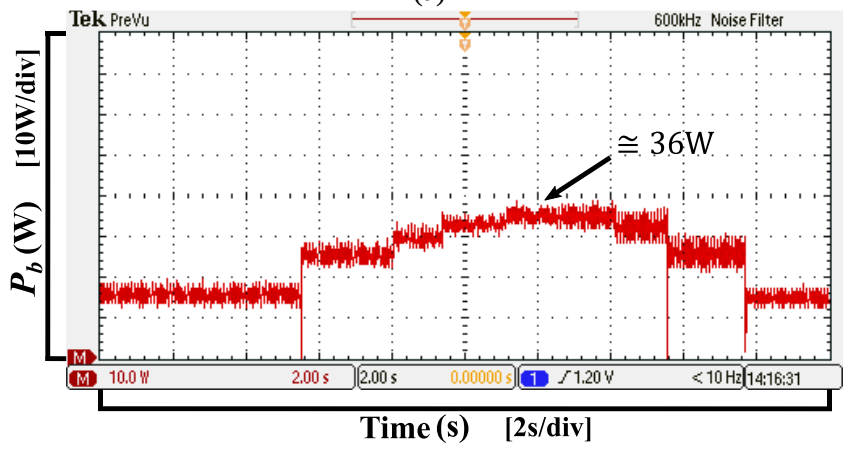

(b)

Figure 4.28. The variation of the voltage V_{dc} (a) and the resulting power flowing towards resistor R_2 (b), for a fixed voltage $V_1 = 14$ V.

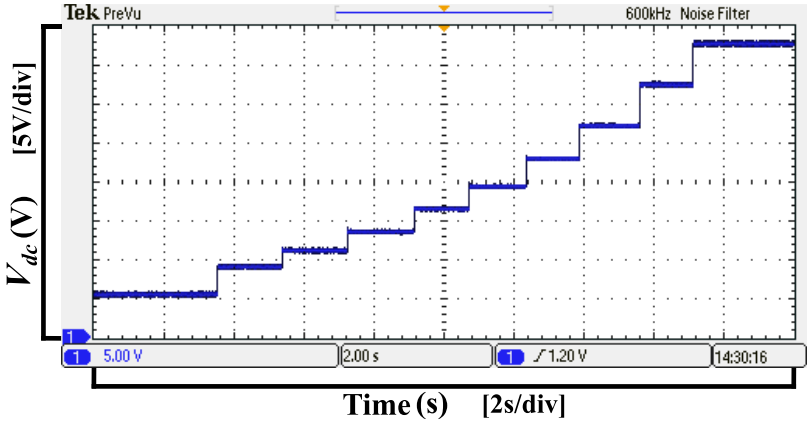

(a)

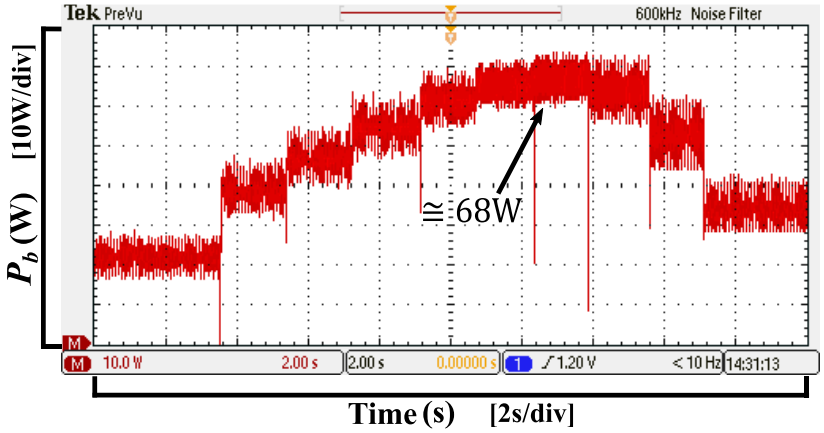

(b)

Figure 4.29. The variation of the voltage V_{dc} (a) and the resulting power flowing towards resistor R_2 (b), for a fixed voltage $V_1 = 18$ V.

In both experiments, the duty cycle was varied manually with a step of 0.1. Due to these rapid changes, spikes were observed in the current and thus, the power, as shown in Figure 4.28 and Figure 4.29. For both cases, the experimental results are close to the theoretical ones. There are differences, though, due to power losses related to the autotransformer windings and the dc-dc converter.

The topology tested with this experiment was proved to be suitable for the final application, as the voltage V_{dc} was varied while the voltage V_s was fixed by the dc source for both the buck and the boost operation of the dc-dc converter.

In this section, the dc-dc converter was used to obtain power curves similar to the power curves of a water turbine for different water speeds. As described in Section 4.2, the turbines used for the hydrokinetic energy conversion system are synchronised and counter-rotating. Thus, the power curves for different water speeds are expected to be similar to the power curves of a hydrokinetic turbine for different water speeds. Furthermore, it was shown that the dc-dc converter was suitable for controlling the

voltage V_{dc}, while the voltage V_s was fixed by the dc source. Consequently, from the experimental procedure described in this section, it is indicated that the dc-dc converter is suitable for the control and the experimental characterisation of the hydrokinetic energy system shown in Figure 4.9.

4.4 Experimental characterisation of the hydrokinetic energy conversion system

4.4.1 Configuration of the system

After the dc-dc converter was tested, the enclosure containing the uncontrolled rectifier and the dc-dc converter was connected to the PMSG of the hydrokinetic energy conversion system, as shown in Figure 4.30. The output of the dc-dc converter was connected to two 12V batteries. Similarly to the previous experiments described in Sections 4.2.6 and 4.2.7, torque and speed measurements were taken at the point of the common shaft, so that the mechanical power was obtained (Point 1 in Figure 4.30). An oscilloscope was used to measure the voltage between the rectifier and the dc-dc converter, V_{dc}. The voltage across the terminals of the batteries, V_b and the current flowing into the batteries I_b (Point 2 in Figure 4.30) were measured in order for the power flowing into the batteries to be calculated.

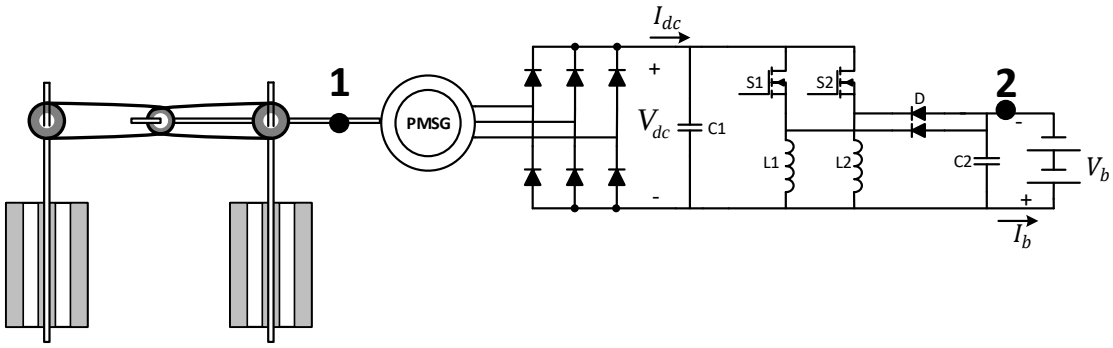

Figure 4.30. Diagram of the experimental set-up for the control of the hydrokinetic energy conversion system.

Figure 4.31 shows the components of the experimental set-up. The water level of the flume, the distance between the shafts of the two identical turbines and the gearing ratio provided by the drive-train were set as in Sections 4.2.6 and 4.2.7.

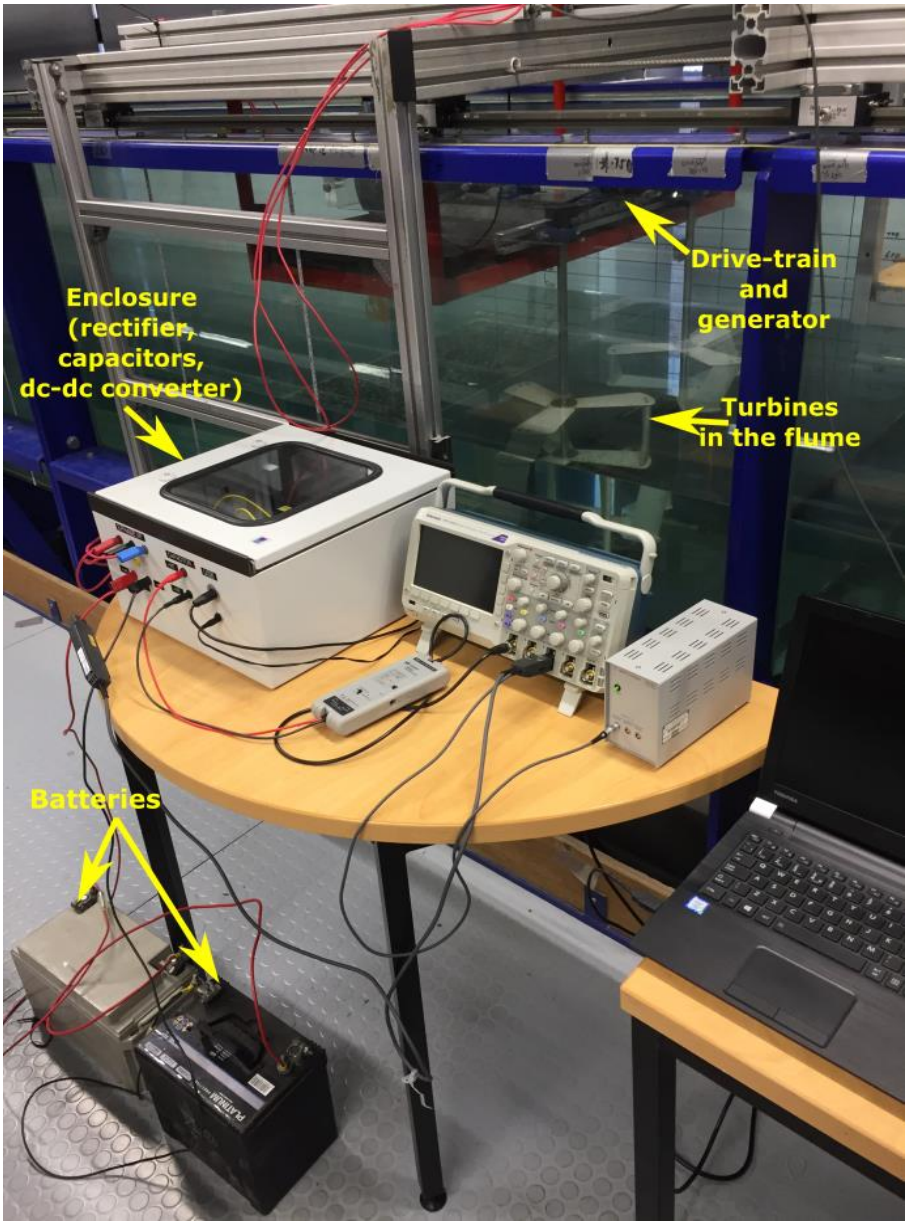

Figure 4.31. The experimental set-up for the control of the hydrokinetic energy conversion system.

4.4.2 Control of the dc-dc converter

The voltage V_b was fixed by the batteries. The dc-dc converter was used to regulate the voltage V_{dc}, and thus, the voltage of the generator terminals. Instead of regulating the voltage V_{dc} by varying the duty cycle *D* of the converter, a PI controller was built to control the voltage V_{dc}, as shown in Figure 4.32. MATLAB/Simulink was used to get the digital signals for the measurements from the ADC part of the converter and built a model for the control of the voltage V_{dc}.

The difference between a reference value for the voltage V_{dc}^* and a measured value V_{dc} was fed into a PI controller. The output of the PI controller was used as an input to the

PWM generator. The gains of the PI controller were carefully selected using the experimental platform, so that the value of the measured voltage follows the reference value.

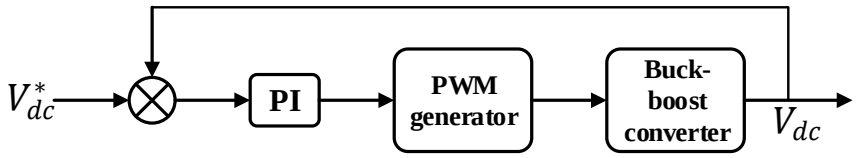

Figure 4.32. Controller for the dc-dc converter.

4.4.3 Experimental results

In order to relate the oscillations observed to the rotation of the turbines, the torque and the speed were recorded and plotted for one minute, for a water speed of 0.72 m/s and a dc voltage $V_{dc} = 13.2$ V and are shown in Figure 4.33(a) and (b). The mean value of the torque measurements was $T_m = 2.191$ Nm and the mean value of the speed of the common shaft was $\omega_{csh} = 12.19$ Nm. Thus, considering a gearing of 4:3, the speed of each turbine was $\omega_{t,mean} = 9.14$ Nm.

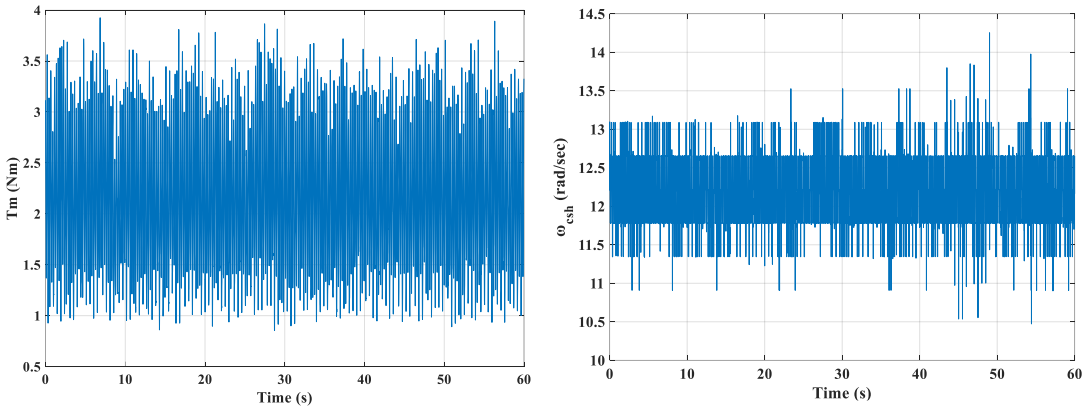

(a) (b)

Figure 4.33. For a water speed of 0.72 m/s and a dc voltage of 13.2 V: (a) torque, (b) rotational speed

Figure 4.34**Error! Reference source not found.**(a) shows the single-sided amplitude s pectrum of the torque T_m, using Fast Fourier Transformation (FFT). In Figure 4.34(b), it is shown that the dominant frequency of the oscillation of the torque is $f_{dom} = 4.366$ Hz. The frequency of the rotation for the example of **Error! Reference source not found.** is given by

$$f_{rot} = \frac{\omega_{t,mean}}{2\pi} = \frac{9.14}{2\pi} = 1.455 \text{ Hz}$$

The ratio between the dominant frequency of the oscillation of the torque and the frequency of rotation is

$$f_{dom} = 4.366\ \text{Hz} = 3 \cdot 1.455\ \text{Hz} = 3 \cdot f_{rot}$$

Therefore, the dominant frequency of the oscillations of the torque is of 3P. This was expected, since the two turbines were synchronised with the use of the timing belt.

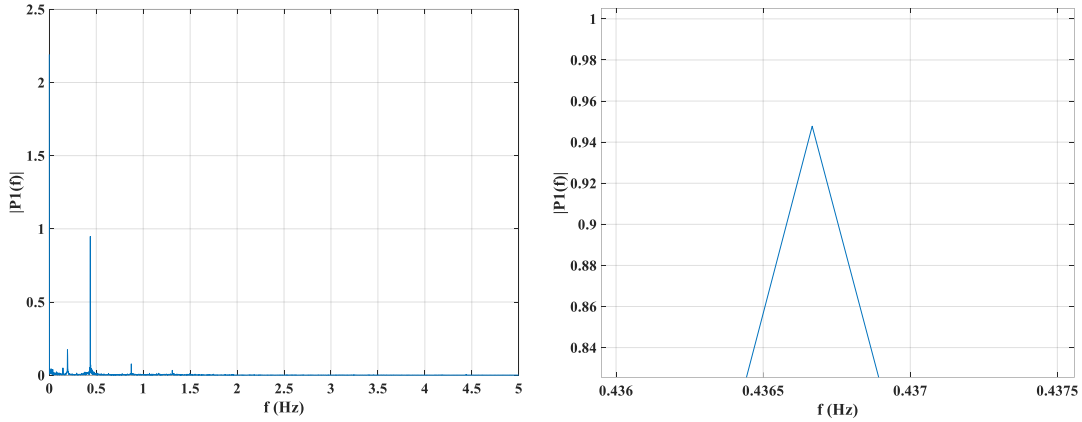

(a) (b)

Figure 4.34. For a water speed of 0.72 m/s and a dc voltage of 13.2 V: (a) single-sided amplitude spectrum of the torque and (b) dominant frequency of oscillations.

For every water speed, the dc voltage was decreased starting from the no-load value down to zero. The step changes were of 1 V and took place every 10 s. Both the mechanical and electrical measurements were quite noisy and the single-sided amplitude spectrum was obtained to spot the frequencies of oscillation using the FFT.

A low-pass filter was used to filter the results and obtain clearer graphs. The transfer function of the first order filter used is given by [115]

$$H(s) = \frac{1}{1 + Ts} \tag{4.11}$$

where T is the time constant of the filter. A time constant of 1 s, corresponding to a frequency of 1 Hz, was selected for the offline filtering of the measurements.

After the filtering and following the calculations described in Section 4.2.7, the $C_p - \lambda$ curve for the system was obtained and is shown in Figure 4.35. Figure 4. shows the power flowing into the batteries versus the rotational speed of the common shaft. For very low voltages (1-4 V) and thus rotational speeds, the system was unstable and no accurate measurements could be taken. Consequently, the $C_p - \lambda$ curves shown in

Error! Reference source not found. are interrupted for very low tip speed ratios and t he power curves shown in Figure 4. are interrupted for very low rotational speeds of the common shaft.

Comparing Figure 4.28 and Figure 4.34, it is concluded that in both tests, the power coefficient exceeded by far the Betz limit (0.593) [116]. The reason was the fact that the turbines used for the test of the hydrokinetic energy conversion system for both tests, were placed into a flume. The flume provided blockage to represent the blockage provided by the canal in real conditions and therefore, the turbines operated under restricted flow conditions. Due to the blockage provided by the flume, high efficiencies were achieved, as shown in **Error! Reference source not found.**.

Figure 4.35. Characteristic curve of the system obtained using the dc-dc converter.

It is shown that compared to the results shown in Figure 4.28, there are no stalling points close to the MPPs for every water speed. The reason this difference is observed is that the results of Figure 4were obtained by varying a resistive load, and thus the current flowing from the generator. The current produced by the PMSG is proportional to the torque. Thus, during the experiment described in Section 4.2.7 the restraining torque provided from the generator to the common shaft of the system of the turbines was constantly increasing. Theoretically, there should not be any stalling points. The resolution of the resistor though was not accurate and the resistive load was changing rapidly for the same physical change after a certain point. As a result, the restraining torque increased rapidly and stalling points occurred.

During the experiment with the dc-dc converter, the dc voltage was controlled and varied, and thus the speed of the PMSG. In conclusion, it was proved that varying the dc voltage using the dc-dc converter is the best method to obtain the characteristic curves.

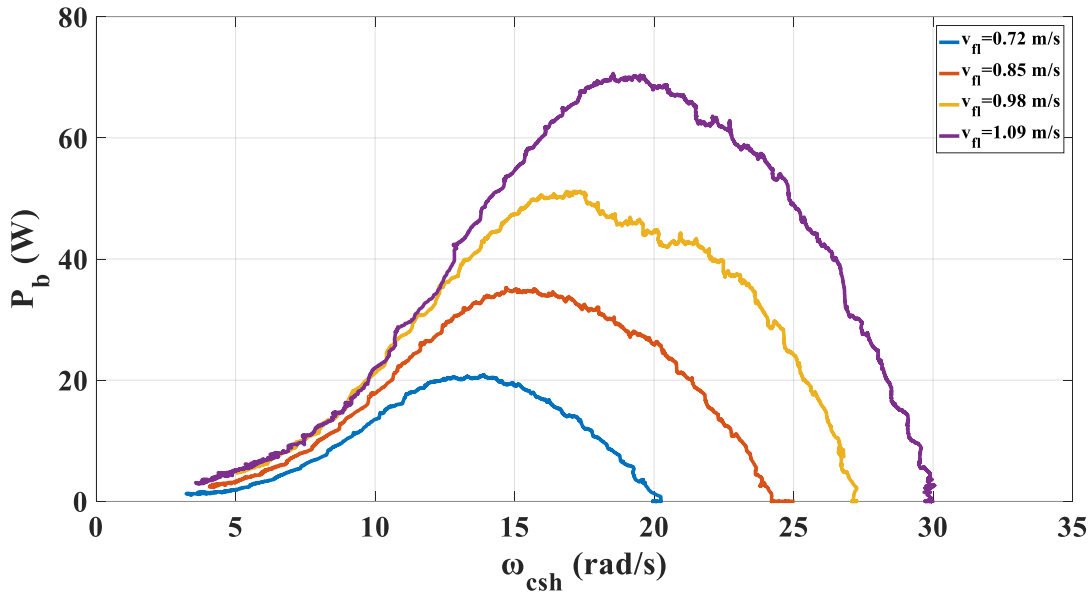

Figure 4.36. Power flowing into the batteries for different water speeds obtained using the dc-dc converter.

4.5 Summary

The electrical subsystem for the control of the laboratory prototype of a hydrokinetic energy conversion system was designed. The hydrokinetic energy conversion system had been previously designed and consists of two synchronised identical vertical-axis turbines driving a PMSG through a common shaft. The output of the PMSG was connected to an uncontrolled rectifier and tests for no-load and resistive load conditions took place. To enable variable-speed operation, a dc-dc converter was proposed for the control of the terminal voltage of the generator and batteries were used to store the energy produced.

The dc-dc converter was purchased from Texas Instruments and a test rig was used to test the converter and evaluate its suitability for the hydrokinetic energy conversion system. The converter was controlled in open loop using MATLAB/Simulink to generate the code for the Code Composer Studio. Power curves were obtained by varying the duty cycle of the converter, and thus, the dc voltage between the rectifier and the buck-boost converter. The ability to control the dc voltage independently from

the voltage fixed by the batteries pointed the suitability of the dc-dc converter for the control of the generator terminal of the hydrokinetic energy conversion system.

After the performance of the converter was tested, a test for the experimental characterisation of the system followed. The dc-dc converter was used to regulate the terminal voltage of the generator and thus, the rotational speed of the common shaft. For this purpose, a PI controller was used. For different water speeds, step changes in the terminal voltage of the generator were applied. This way, the $C_p - \lambda$ curves of the system for different water speeds were obtained. Very high efficiencies were observed due to the blockage provided by the experimental flume.

Chapter 5

Maximum power extraction from the hydrokinetic energy conversion system

Data for the turbines of the laboratory prototype and the full-scale hydrokinetic energy conversion system were provided by Mr Stefan Runge of Cardiff University, School of Engineering, UK.

5.1 Introduction

The use of power electronics for the operation of the hydrokinetic energy conversion system enables the extraction of the maximum power available in the flowing water. Power electronics are used in variable-speed turbines to decouple the generator from the load (storage, grid) and therefore, the MPPT of the device is enabled [12].

The MPPT of turbine-based systems, such as the wind turbines, are most commonly based on a predefined trajectory for the regulation of the torque. However, MPPT algorithms are reported to be used to regulate the electric load applied to the generator [53].

In this chapter, the laboratory prototype of the hydrokinetic energy conversion system for waterways was modelled using data from the experimental results presented in Chapter 4. The maximum power extraction was achieved with the use of a control scheme based on a heuristic algorithm widely used for the MPPT of photovoltaic arrays. Experimental validation of the controller followed. Finally, the full-scale hydrokinetic energy conversion system was modelled and the MPPT procedure was simulated. The impact of the difference in inertia between the laboratory prototype and the full-scale system on the modification of the MPPT algorithm was highlighted.

5.2 Control for the maximum power tracking

5.2.1 Control scheme for the maximum power extraction from the hydrokinetic energy conversion system

Figure 5.1 shows the control scheme for the MPPT of the laboratory prototype. For a constant voltage V_b fixed by the batteries, the dc-dc converter is used for the control of the voltage V_{dc} for the MPPT. No mechanical sensors are needed.

The voltage V_{dc} and the current I_{dc} are measured every 10 μs and low-pass filtering with a time constant T_c (details given in Appendix C) is used to eliminate the 3P oscillations caused by the vertical-axis turbines. Then, the generated power P is calculated and used as an input to the MPPT stage. At the MPPT stage, a reference value for the voltage V_{dc}^* is chosen. The difference between the measured and the reference value of the voltage V_{dc} is fed to a PI controller. The PI controller generates the input signal for the PWM generator for the control of the dc-dc converter. The PI gains are given in Appendix B.

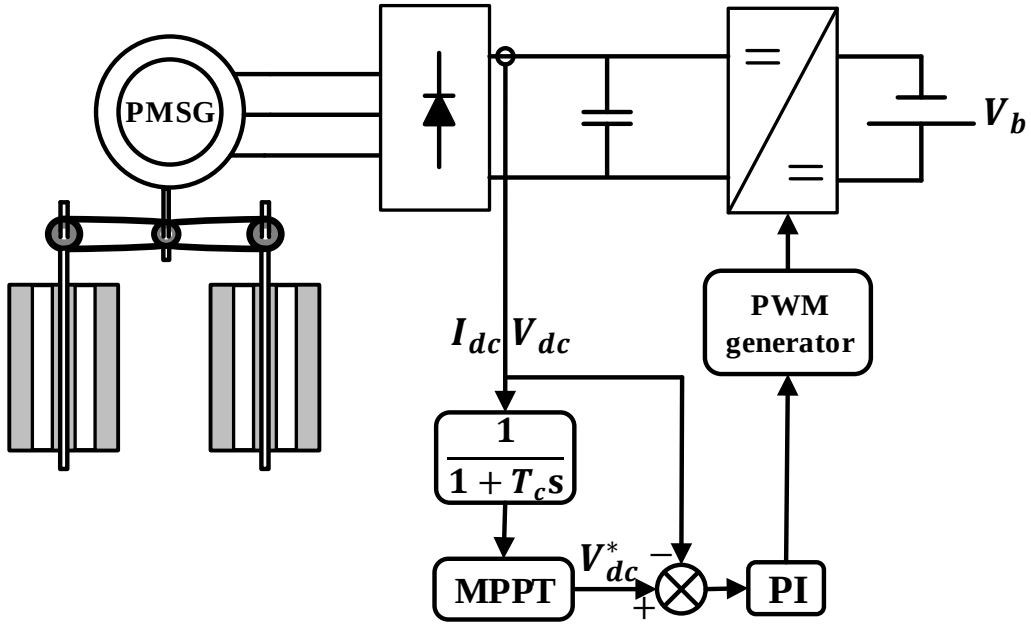

Figure 5.1. Control scheme for the maximum power tracking of the hydrokinetic energy conversion system

5.2.2 Analysis of the 'perturb and observe' algorithm

The perturb and observe (P&O) algorithm is based on the perturbation of one variable and the observation of another. For the hydrokinetic energy conversion system, the

voltage V_{dc} was perturbed and the resulting power was measured. An analytical explanation of the tracking algorithm follows.

Figure 5.2 shows the power curve of the hydrokinetic energy conversion system for a specific water speed.

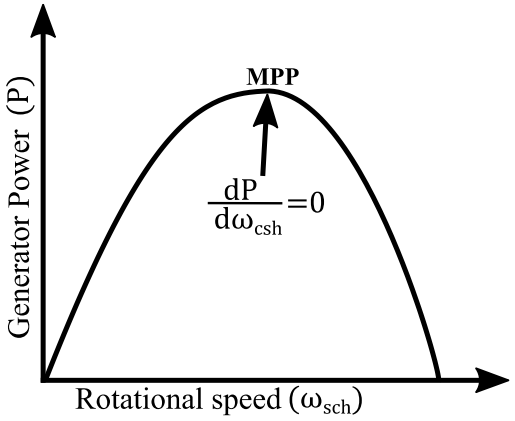

Figure 5.2. Condition at MPP.

It is shown that at the MPP,

$$\frac{dP}{d\omega_{csh}} = 0 \tag{5.1}$$

For vertical-axis turbines with fixed pitch blades, the power coefficient C_p is a function of the tip speed ratio λ. The tip speed ratio is given by

$$\lambda = \frac{\omega_t R}{v_{fl}} \tag{5.2}$$

where ω_t is the rotational speed of each turbine.

Therefore, the power captured by the two turbines of the hydrokinetic energy conversion system is given by

$$P = \frac{1}{2}\rho(2A)v_{fl}^3 C_p(\lambda) \tag{5.3}$$

The two turbines are synchronized and counter rotate with the same rotational speed ω_t. Given a gearing ratio N, the relationship between the rotational speed of each turbine and the rotational speed of the common shaft is given by

$$\omega_t = \frac{\omega_{csh}}{N} \tag{5.4}$$

The common shaft drives the PMSG and thus, the rotational speed of the common shaft ω_{csh} is the same as the rotational speed of the generator. Therefore, the rotational speed of the common shaft is linked to the electrical angular frequency of the generated voltage ω_e by

$$\omega_e = p \cdot \omega_{csh} \tag{5.5}$$

In [117], it is shown that the rectified voltage V_{dc} is a function of the electrical angular frequency ω_e

$$V_{dc} = V_{dc}(\omega_e) \tag{5.6}$$

and

$$\frac{dV_{dc}}{d\omega_e} > 0 \tag{5.7}$$

From (5.3)–(5.6), considering (5.2), it is deduced that

$$P = P(V_{dc}(\omega_e(\omega_{csh}))) \tag{5.8}$$

Therefore, applying the chain rule to (5.3), (5.1) is written as follows

$$\frac{dP}{d\omega_{csh}} = \frac{dP}{dV_{dc}} \cdot \frac{dV_{dc}}{d\omega_e} \cdot \frac{d\omega_e}{d\omega_{csh}} = 0 \tag{5.9}$$

From (5.5), it is concluded that

$$\frac{d\omega_e}{d\omega_{csh}} = p > 0 \tag{5.10}$$

Thus, from (5.1), considering (5.7) and (5.10), at the MPP

$$\frac{dP}{dV_{dc}} = 0 \tag{5.11}$$

Similarly to [77], for the MPPT of the hydrokinetic energy conversion system, a gradient-based method is used with a sampling period T_s

$$V_{dc,k} = V_{dc,k-1} + \int_{\tau=t_{k-1}}^{\tau=t_k} S \cdot \mathrm{sgn}(P_k - P_{k-1}) \cdot \mathrm{sgn}(V_{dc,k} - V_{dc,k-1}) d\tau \tag{5.12}$$

where index *k* denotes successive discrete time points such that $T_s = t_k - t_{k-1}$, $V_{dc,k}$ and P_k are the values of the rectifier voltage and the power at time t_k and S is the convergence speed coefficient.

The flowchart of the P&O algorithm based on (5.20) is shown in Figure 5.3. The voltage V_{dc} and the current I_{dc} are measured and the power is calculated. For a specific perturbation, if the electrical power is increased, then a step change in the voltage of the same direction takes place. Otherwise, the same step change takes place with a reversed sign. If there is no change in the power, the algorithm is terminated.

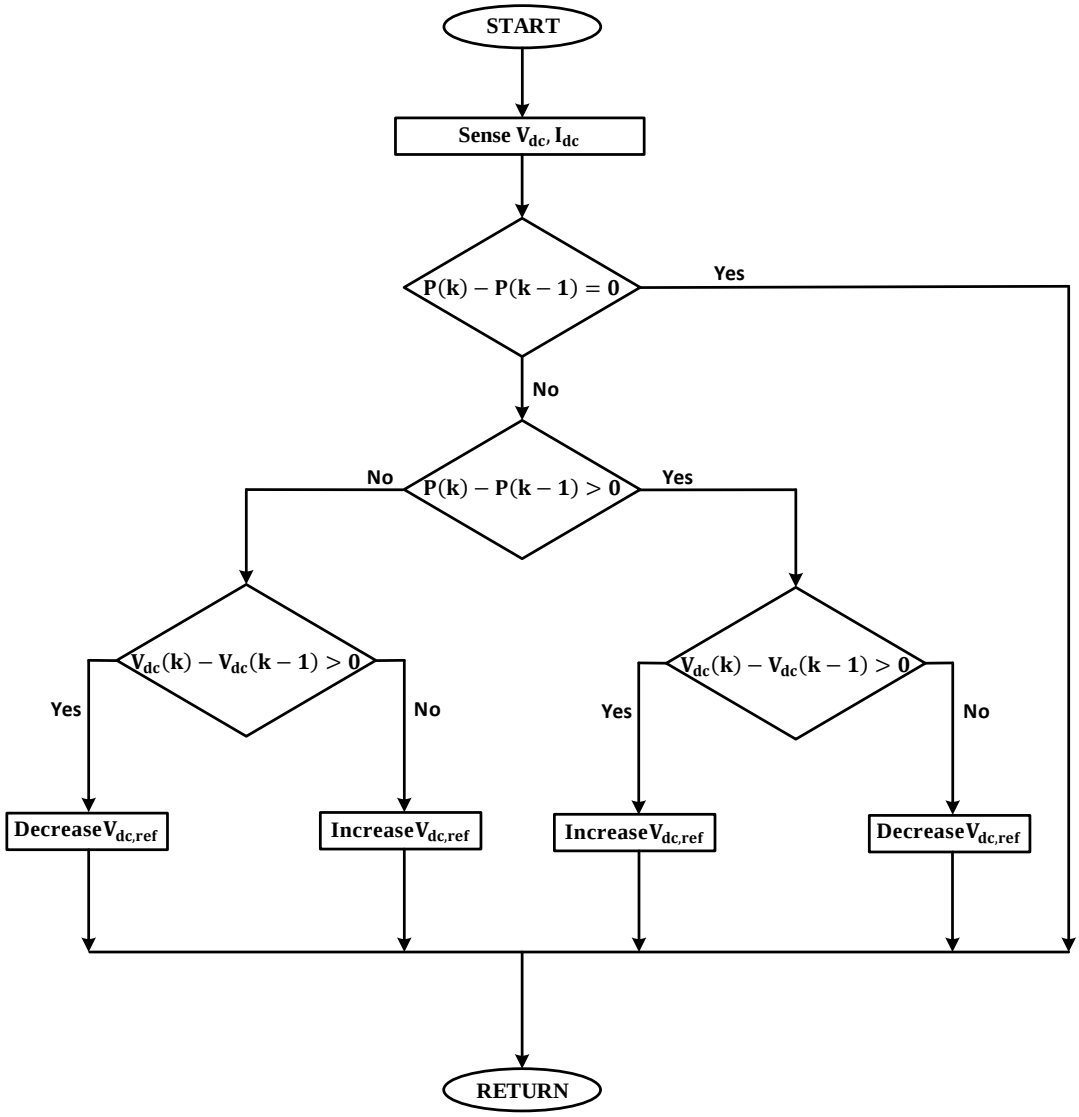

Figure 5.3. The P&O algorithm for the MPPT.

An example of the tracking procedure for a constant water speed is shown in Figure 5.4. The initial voltage is close to its no-load value. Then, the P&O algorithm is activated. For a perturbation of the voltage k, a resulting power of a difference of dP is observed. The voltage is being changed until the maximum power for the specific water speed results. Finally, there is an oscillation around the MPP. The width of this oscillation depends on the speed convergence coefficient, S [76].

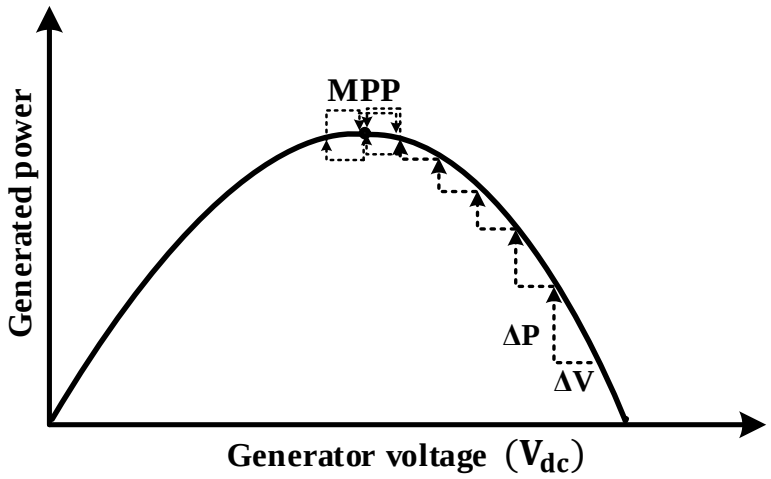

Figure 5.1. Tracking procedure for a constant water speed.

5.3 Simulation of the laboratory prototype

5.3.1 Modelling of the hydrokinetic energy conversion system

The laboratory prototype of the hydrokinetic energy conversion system shown in Figure 5.1 was modelled and simulated using MATLAB/Simulink. A hydrodynamic and a drive-train model were developed using mathematical equations. Blocks provided by MATLAB/Simulink were used for the simulation of the PMSG, the diode-bridge and the batteries.

5.3.1.1 Hydrodynamic model

The hydrodynamic model shown in Figure 5.5 was used to calculate the torque produced by the turbines and measured experimentally at the point of the common shaft. The speed of the common shaft, ω_{csh}, is measured and the rotational speed of each turbine, ω_t, is calculated using the gearing ratio, N. This way the tip speed ratio, λ, is obtained and a look-up table is used to determine the power coefficient C_p. The data for the look-up table used for the calculation of the C_p were obtained from the filtered results of the experimental test described in Section 4.4.4. Then, the power available in the water is calculated using (4.8). Finally, the mechanical torque of the common shaft, τ_{hyd}, is calculated.

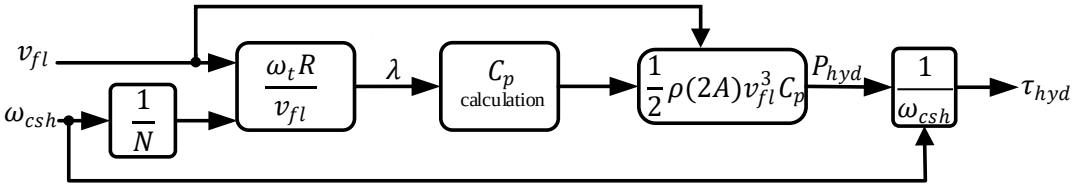

Figure 5.5. Hydrodynamic model of the system of the two identical turbines.

5.3.1.2 Drive-train model

A one-mass (lumped) model was used to simulate the drive-train of the system. The equation that describes the drive-train model is given by [118]

$$\frac{d\omega_{csh}}{dt} = \frac{T_{hyd} - T_{em}}{J_{total}} \tag{5.13}$$

where J_{total} is the total inertia of the rotating mass and T_{em} is the electromagnetic torque of the generator.

In order for (5.13) to be used for the simulation of the drive-train, the total inertia of the system was calculated. It was assumed that the total inertia is the the summation of the inertias of the turbines and the generator. The inertia of the generator is given by the manufacturer specifications in Appendix B.

For the estimation of the inertia of each turbine, the mass of each blade, M_{1b}, was calculated using

$$M_{1b} = V_{blade} \cdot d_{blade} \tag{5.14}$$

where V_{blade} is the volume and d_{blade} is the density of each blade. For the laboratory prototype, data from the design of the blade were used and are given in Appendix B. The mass of each blade was calculated to be 0.252090 Kg.

Assuming that the blade is a point mass rotating in a distance R from the rotor of the vertical-axis turbine, the inertia of each blade was calculated using

$$J_{1b} = M_{1b} \cdot R^2 \tag{5.15}$$

where R is the radius of each turbine.

As shown in Figure 5.1, each turbine consists of three blades. Neglecting the inertia of the spikes and the rotor, the inertia of each turbine is given by

$$J_{1t} = 3J_{1b} \tag{5.16}$$

The total inertia of the two turbines, referring to the LSS shaft, was calculated using

$$J_{2t} = 2J_{1t} \tag{5.17}$$

The timing belt used for the coupling of the two turbines and the common shaft, provided a gearing *N* of 4:3. Therefore, the inertia of the two turbines referring to the common shaft was calculated using

$$J_{2t,csh} = \frac{J_{2t}}{N^2} \tag{5.18}$$

Therefore, the total inertia of the system is given by

$$J_{total} = J_{2t} + J_{gen} \tag{5.19}$$

where J_{gen} is the inertia of the generator.

Using (5.14)–(5.19) the total inertia of the system was calculated 0.08756 Kgm^2.

5.3.1.3 Generator model

The model of the generator provided by Simscape library in MATLAB/Simulink is based on equations (3.6)-(3.8). To simulate the laboratory system, the specifications of the PMSG were provided by the manufacturer and are given in Appendix B. Four parameters were required: the stator phase resistance, the armature inductance, the machine constant (flux linkage established by the magnets, voltage constant or torque constant) and the number of the pole pairs.

The stator resistance was calculated using [119]

$$R_s = \frac{R_{L-L}}{2} \tag{5.20}$$

where R_{L-L} is the line-to-line resistance specified by the manufacturer of the generator.

The flux linkage was calculated using the voltage constant given by the manufacturer specifications as $V_{dc}/krpm$.

$$\lambda_m = \frac{\sqrt{2}}{\sqrt{3}} \frac{V_{L-L,rms}}{p \cdot \omega_m} \tag{5.21}$$

where p is the number of the pole pairs, $V_{L-L,rms}$ is the line-to-line terminal voltage of the generator derived the $V_{dc}/krpm$ value and ω_m is the rotational speed of the rotor of the generator for a generated voltage $V_{L-L,rms}$ (1000 rpm=104.72 rad/sec).

5.3.1.4 Models for the diode-bridge, the buck-boost converter and the batteries

A model of a diode-bridge rectifier from the Simscape library of MATLAB/Simulink was used. Four IGBT/Diode blocks were used to model and simulate the buck-boost converter. Two of the IGBT/Diode blocks were driven by PWM signals and the other two were used as uncontrolled diodes. The forward voltages of the forced-commutated devices and the diodes were ignored. Finally, the batteries were modelled using a dc voltage source in series with a small (internal) resistance.

Figure 5.6 shows the configuration of the model used to simulate the hydrokinetic energy conversion system in comparison with the laboratory prototype. In Figure 5.6, V_{dc} is the dc voltage varied by controlling the dc-dc converter and P_b is the power flowing into the batteries.

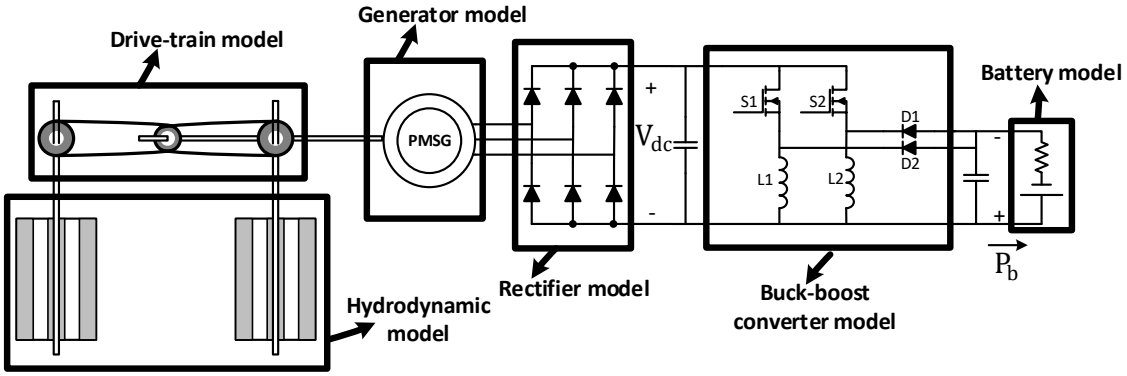

Figure 5.6. Configuration of the model used to simulate the hydrokinetic energy conversion system.

5.3.2 Simulation of the MPPT of the laboratory prototype

The laboratory prototype was simulated in order to validate the performance of the MPPT algorithm prior to the experimental validation.

As described in Section 4.2.4, an interleaved dc-dc converter was used. For the simulation of the interleaved dc-dc converter, two PWM generators were used to generate signals with a phase difference of 180°. The simulation results for a duty cycle of 0.4 are shown in Figure 5.7. The two PWM signals shown in Figure 5.7(a)

and Figure 5.7(b) demonstrate the phase difference of 180^o required for the interleaved operation of the dc-dc converter. Similarly to the PWM signals generated for the experimental test of the dc-dc converter shown in Figure 4.12, the frequency of the PMW signals, and thus the switching frequency of the dc-dc converter was 100kHz.

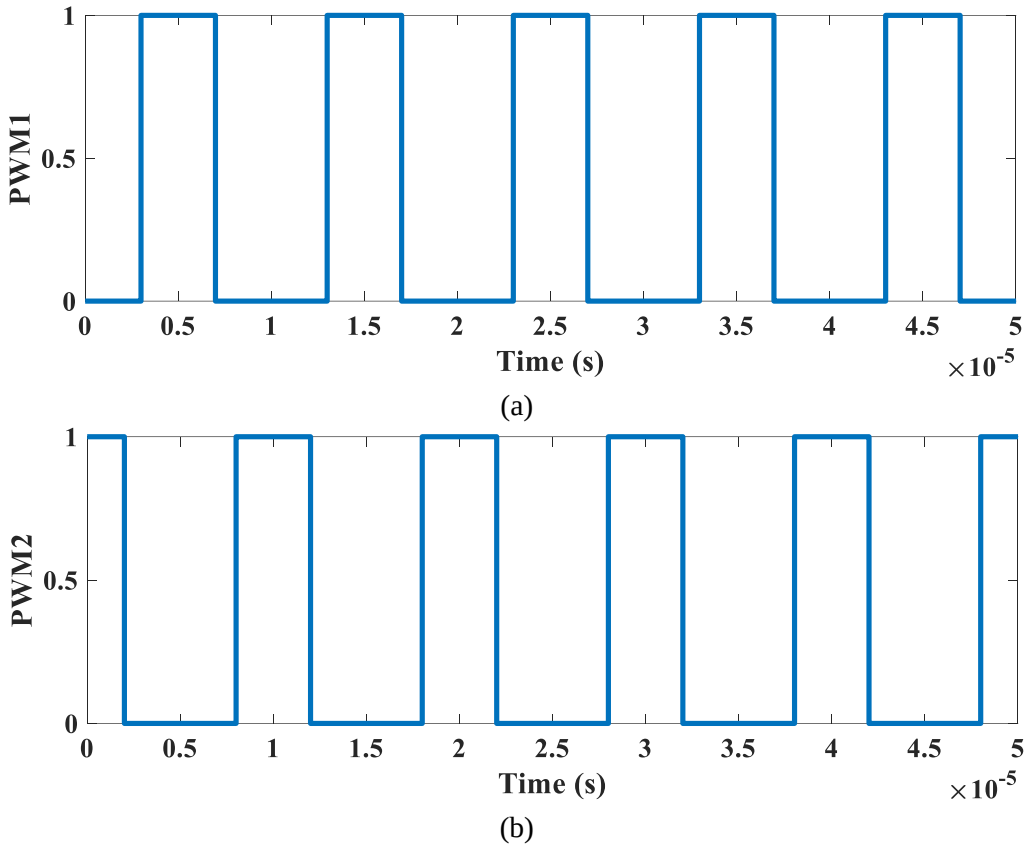

Figure 5.7. Simulation of the PWM signals.

To assess the performance of the PI controller used for the control of the dc-dc converter, step changes in the dc voltage were applied. Figure 5.8 shows the response of the system for step changes in the reference value of the dc voltage. The red line shows the reference value of the voltage and the black line shows the measured dc voltage. It is shown that the measured voltage, V_{dc}, follows the reference value with a small overshooting.

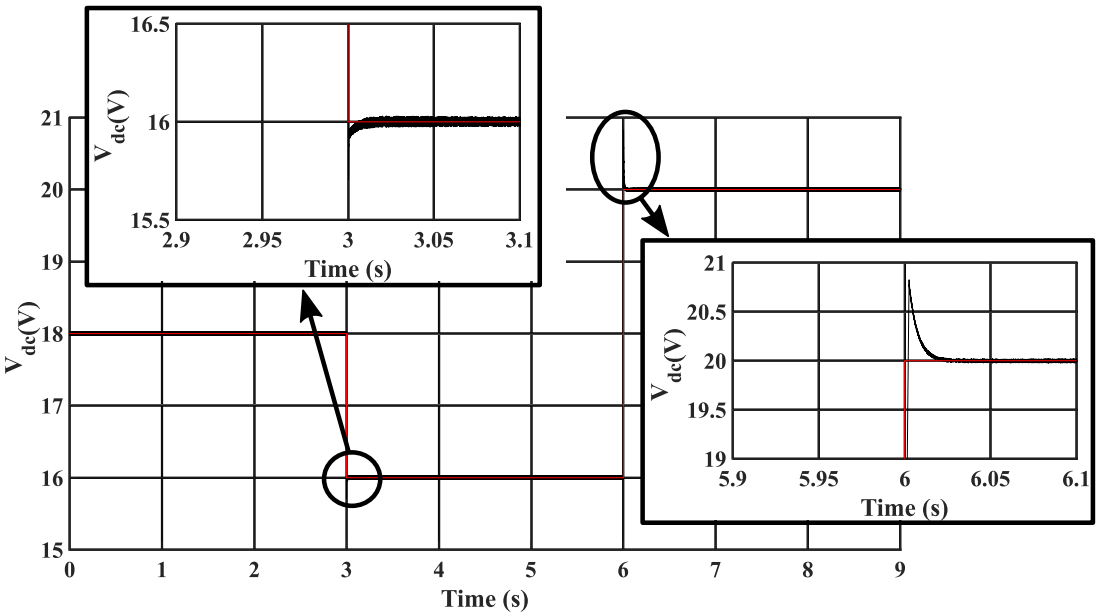

Figure 5.8. Step changes in response to V_{dc} reference.

Figure 5.9 shows the response of the rotational speed of the common shaft of the hydrokinetic energy conversion system, and thus the generator, for a change in V_{dc}. For a constant water speed of 0.98 m/s, a step change in V_{dc} from 17 to 17.2 V was applied at 6 s. It is shown that for the specific inertia calculated for the laboratory system (0.08756 Kgm^2), a time interval of ≅ 0.4 s was needed for the new value of the rotational speed to settle.

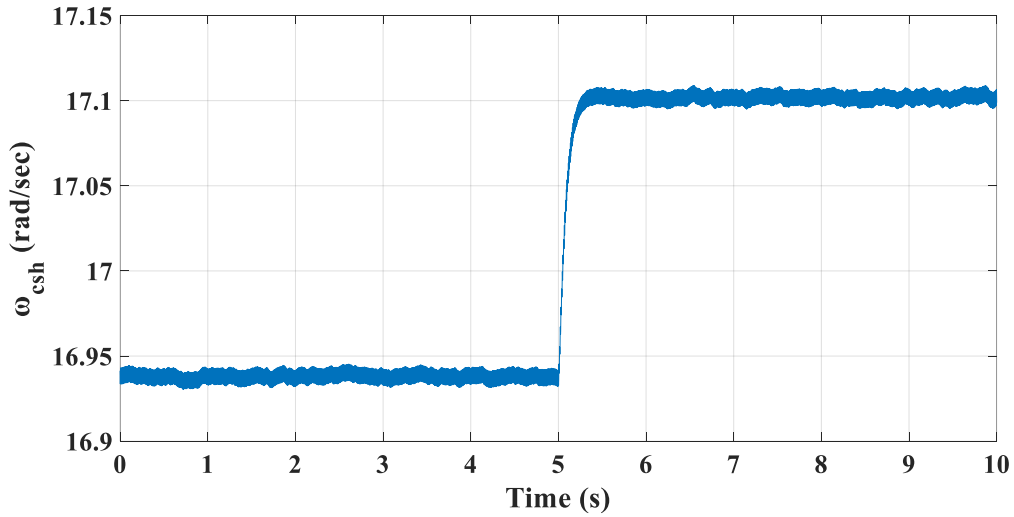

Figure 5.9. Simulation of the laboratory prototype: response of the rotational speed ω_{csh} resulting from a change of 0.2V in V_{dc}.

In order to simulate the MPPT of the hydrokinetic energy conversion system, the control scheme shown in Figure 5.1 was used. A function block provided by MATLAB/Simulink was used to integrate the code for the P&O algorithm into the

simulation. The sampling time T_s of the MPPT algorithm was set to 0.5 s and the convergence speed coefficient S was set to 0.2 V. The water speed was linearly decreased from 0.98 to 0.72 m/s and the results are shown in Figure 5.10.

Figure 5.10(a) shows the change in the water speed. Figure 5.10(b) shows the change in V_{dc} and Figure 5.10(c) shows the change in ω_{csh}. It is shown that after the water speed is settled to its final value, there is an oscillation around specific values of V_{dc} and ω_{csh}, which correspond to the MPP.

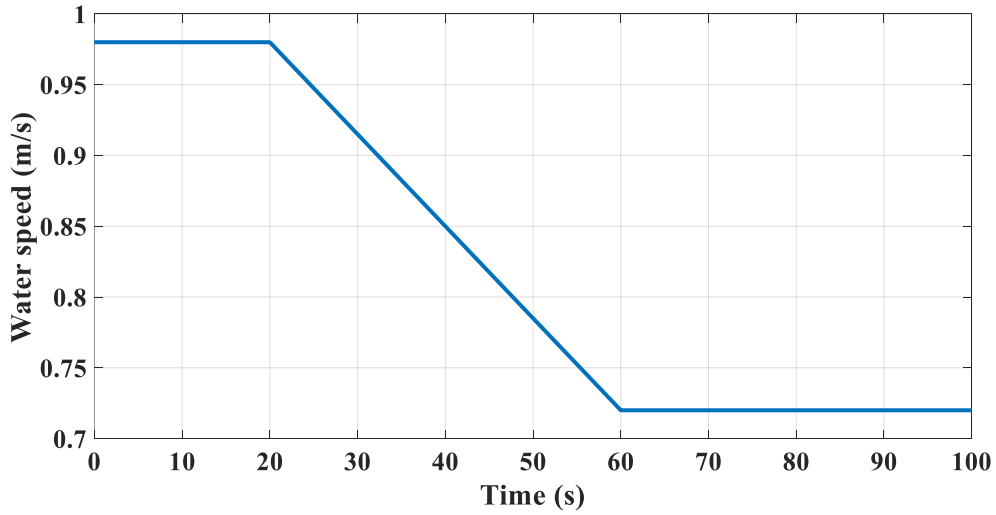

(a)

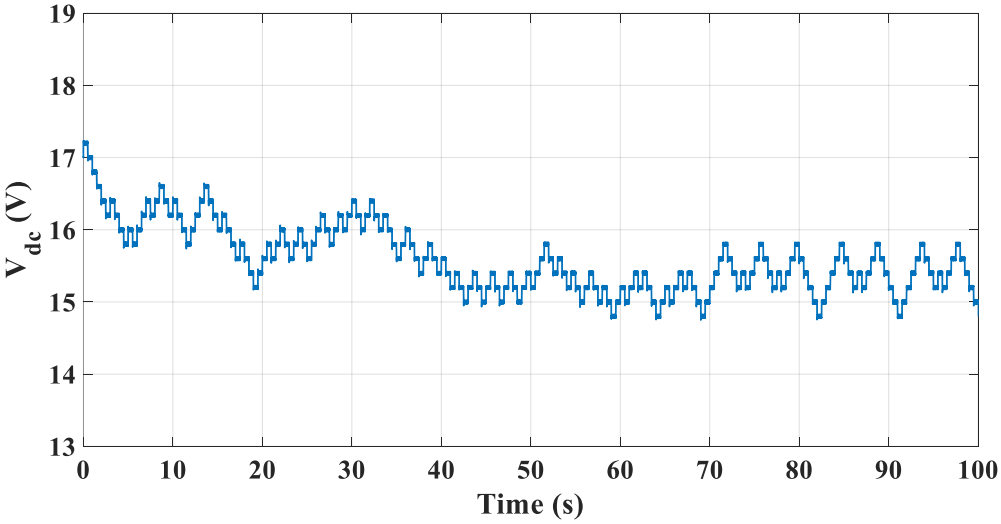

(b)

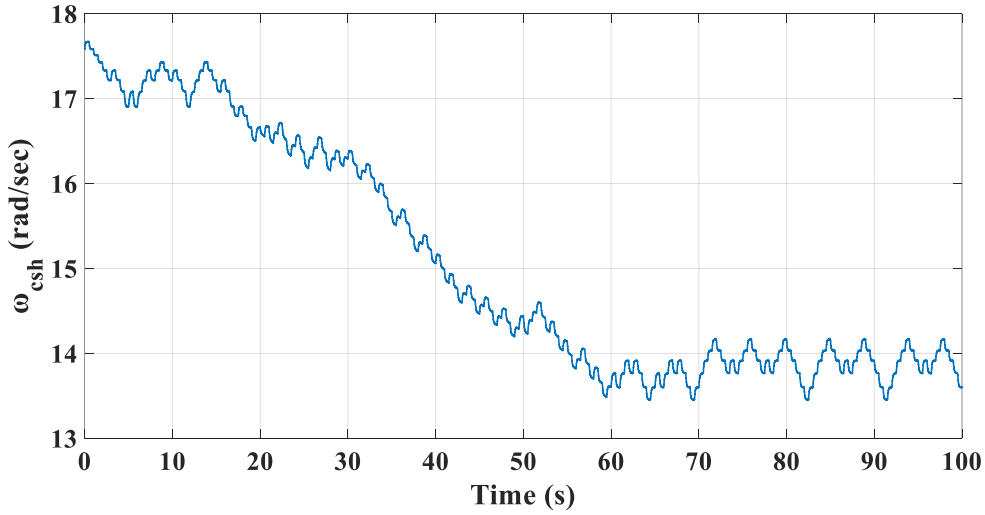

(c)

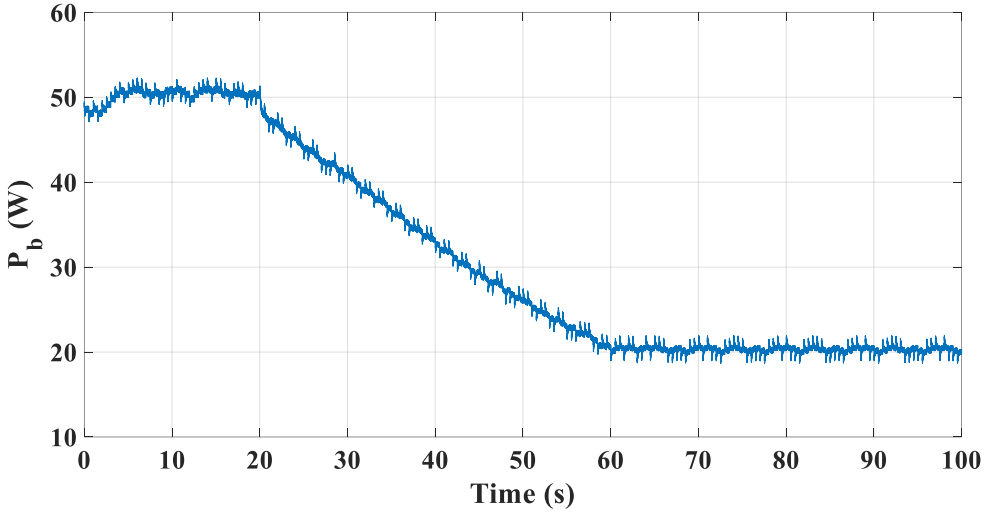

(d)

Figure 5.10/ Results from the simulation of the MPPT of the laboratory prototype ($S = 0.2V$, $T_s = 0.5s$): (a) water speed, (b) dc voltage, (c) rotational speed of the common shaft, (d) power flowing into the batteries.

Figure 5.11 shows the MPPT procedure. The red curve is the power curve of the hydrokinetic energy conversion system for a water speed of 0.98 m/s. The blue curve is the power curve of the hydrokinetic energy conversion system for a water speed of 0.72 m/s. These two power curves were obtained from the results shown in Figure 4.. The green curve shows the simulation of the tracking procedure. Maximum power extraction was achieved for both water speeds and the tracking of the MPP was maintained during the change in the water speed. A small oscillation around the MPP was observed.

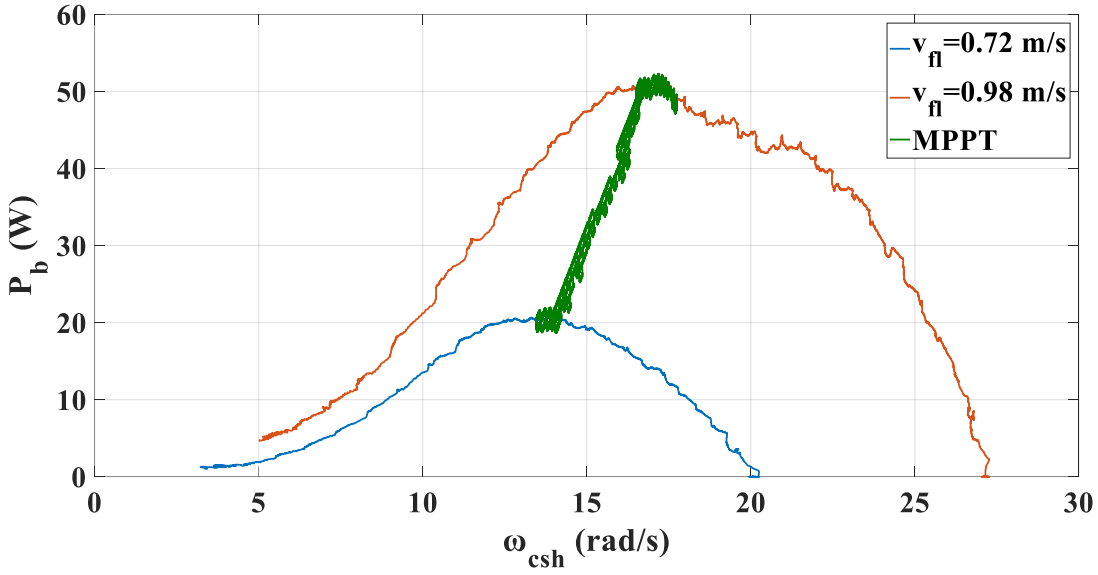

Figure 5.11. Simulation of the MPPT procedure for the laboratory prototype ($S = 0.2V$, $T_s = 0.5s$).

To ensure the selected values for the convergence speed coefficient and the sampling time are the best, two more simulation cases were studied. At first the MPPT of the laboratory scale hydrokinetic energy conversion system was tested for a convergence speed coefficient of 0.4V.

Figure 5.12 shows the results of the simulation of the laboratory prototype with a convergence speed coefficient of 0.4V and a sampling time of 0.5s. It is shown that the MPPT is achieved as in the case of a step change of 0.2V. The step change of 0.4V in the dc voltage, shown in Figure 5.12(a), results in a higher step change in the rotational speed of the generator compared to the case with a step change of 0.2V as shown in Figure 5.12(b). Comparing Figures 5.12(c) and 5.10(d), the level of the power flowing into the batteries is the same. The difference is that there is a larger oscillation around the MPP, as shown in Figure 5.12(d).

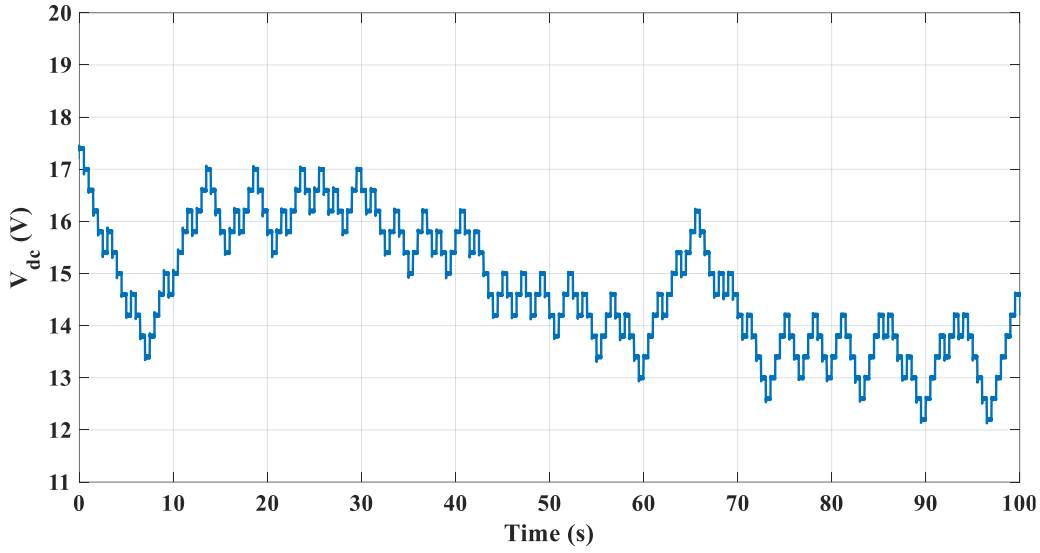

(a)

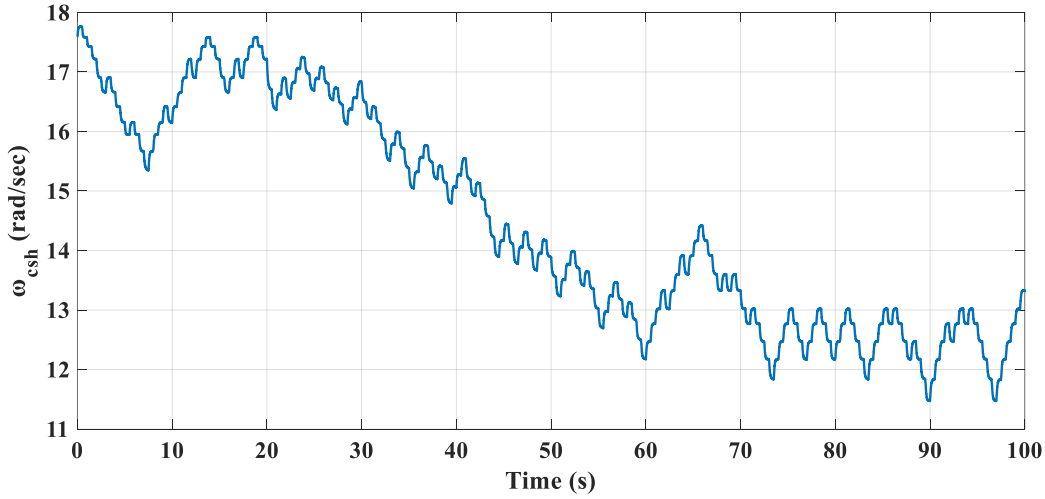

(b)

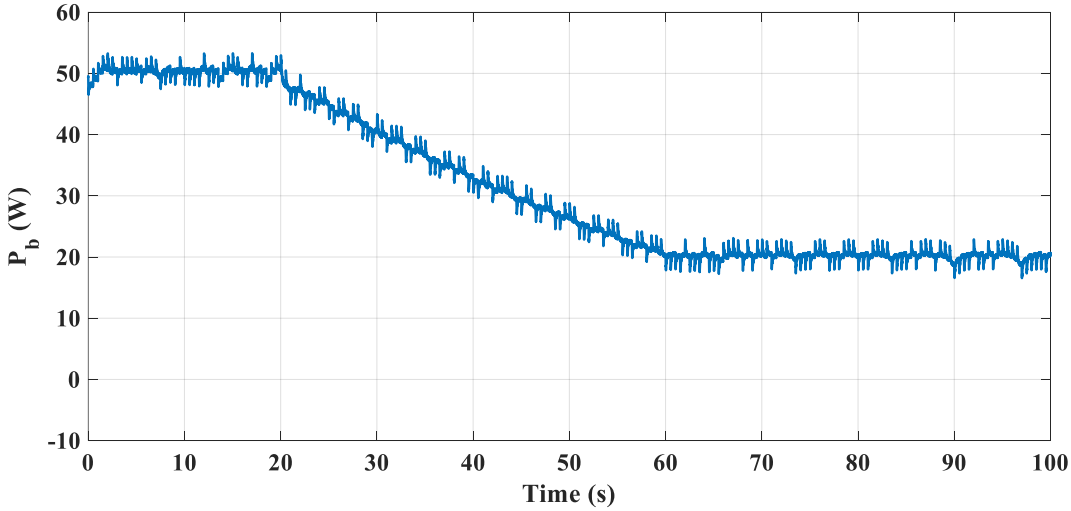

(c)

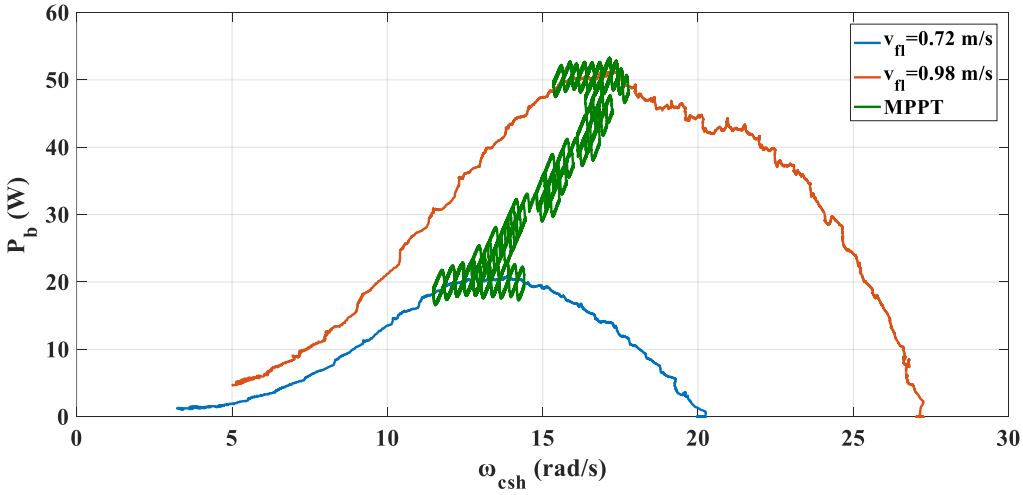

(d)

Figure 5.12. Results from the simulation of the MPPT of the laboratory prototype ($S = 0.4V$, $T_s = 0.5s$): (a) dc voltage, (b) rotational speed of the common shaft, (c) power flowing into the batteries and (d) power flowing into the batteries against the rotational speed of the common shaft.

To demonstrate the effect of a higher convergence speed coefficient (0.4V instead of 0.2V) on the oscillations around the MPP, a graphical representation using the $C_p - \lambda$ curves of the hydrokinetic energy conversion system is used, as shown in Figure 5.13. The $C_p - \lambda$ curves were obtained using the filtered data, as described in Section 4.4.3.

Figure 5.13 shows the impact of the MPPT oscillation on the energy capture. The $C_p - \lambda$ curves shown Figure 5.13(a) shows the impact of the oscillations around the MPP on the $C_p - \lambda$ curve for a convergence speed coefficient of 0.2V and Figure 5.13(b) for a step change of 0.4V. It is shown that the larger oscillations around the MPP that were observed for a larger perturbation of the voltage result in a larger amount of power losses during the MPPT.

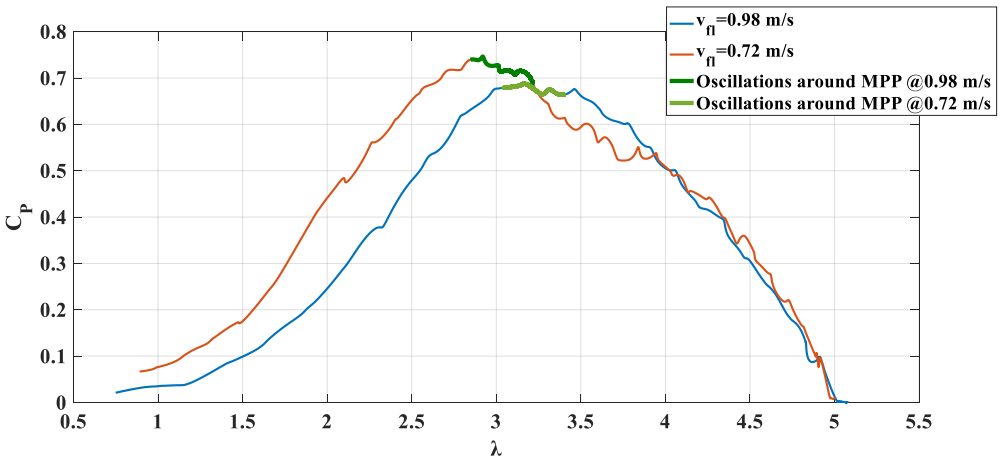

(a)

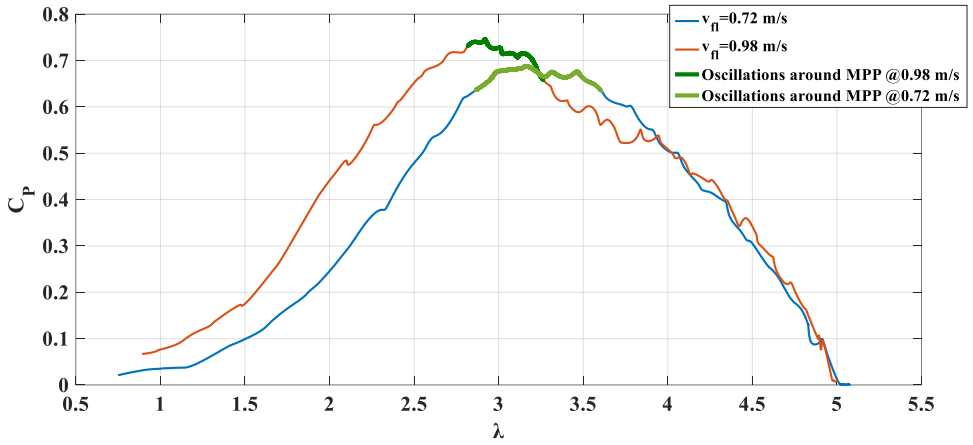

(b)

Figure 5.13. Impact of MPPT oscillation on energy capture for (a) $S = 0.2V$ and (b) $S = 0.4V$.

To investigate the impact of the sampling time of the MPPT algorithm on the tracking time of the MPP, the MPPT of the laboratory prototype was simulated for a sampling time of 0.8s. The results are shown in Figure 5.14. The MPPT is also achieved in this case. However, due to the slow transition from the one water speed to the other, the effect on the tracking time is not obvious.

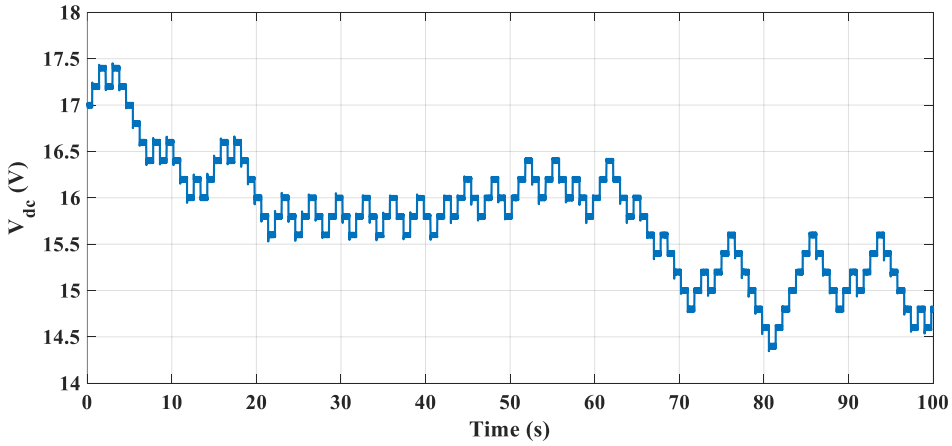

(a)

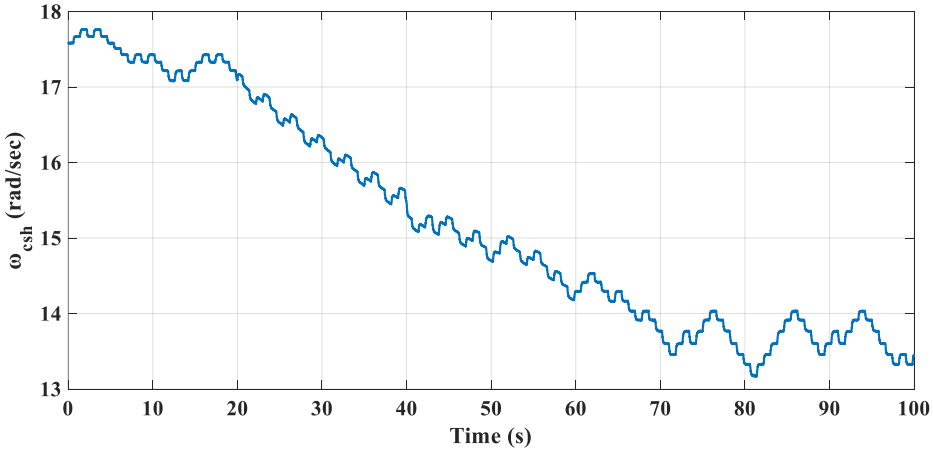

(b)

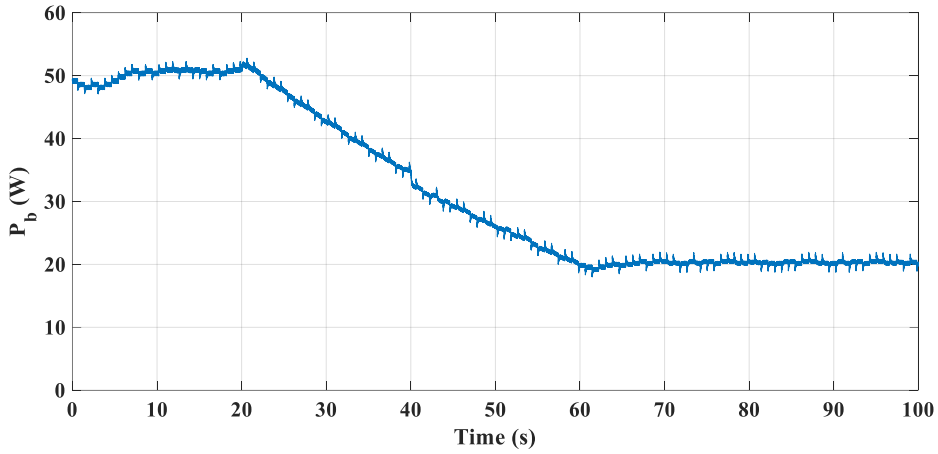

(c)

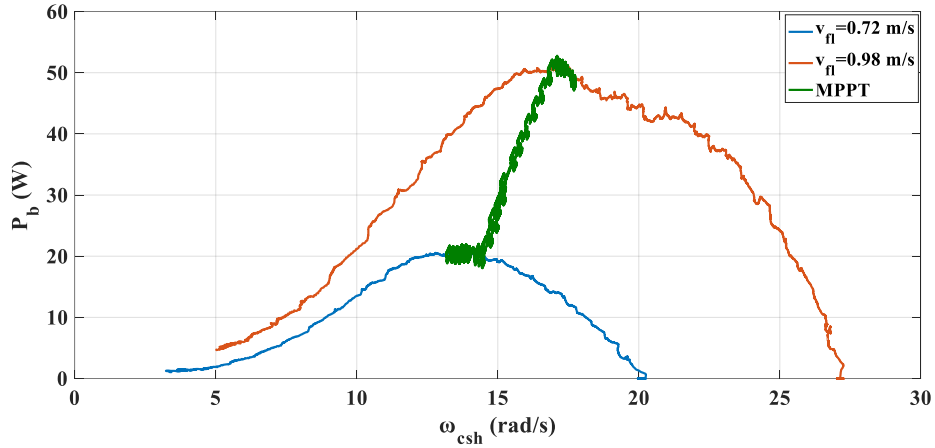

(d)

Figure 5.14. Results from the simulation of the MPPT of the laboratory prototype ($S = 0.2V$, $T_s = 0.8s$): (a) dc voltage, (b) rotational speed of the common shaft, (c) power flowing into the batteries and (d) power flowing into the batteries against the rotational speed of the common shaft.

To demonstrate the effect of the sampling time on the tracking speed of the MPP, a step change in the water speed was assumed, as shown in Figure 5.15(a). The resulting power for a sampling time of 0.5s is shown in Figure 5.15(b) and for a sampling time of 0.8s in Figure 5.15(c). It is shown that more time is needed for the MPP to be reached for a bigger sampling time (0.8s) of the MPPT algorithm rather than a lower one (0.5s). However, even though a lower value of the sampling time leads to a faster track of the MPP, it also leads to more oscillations around the MPP.

The simulation results shown in Figures 5.10-5.15 indicate that the best values of the convergence speed coefficient and the sampling time of the MPPT algorithm are 0.2V and 0.5s, respectively. For the simulation of the laboratory prototype, the step change of 0.2V leads to a step change of ≈0.1 rad/sec in the rotational speed. Therefore, that is the minimum step for the perturbation of the voltage for a reasonable change in the resulting power. In addition, it is shown that the sampling time of the algorithm needs

directly affects the tracking time of the algorithm and the step change in the voltage mainly affects the amplitude of the oscillations around the MPP. However, these two parameters cannot be selected independently, because they affect each other and thus the performance of the algorithm.

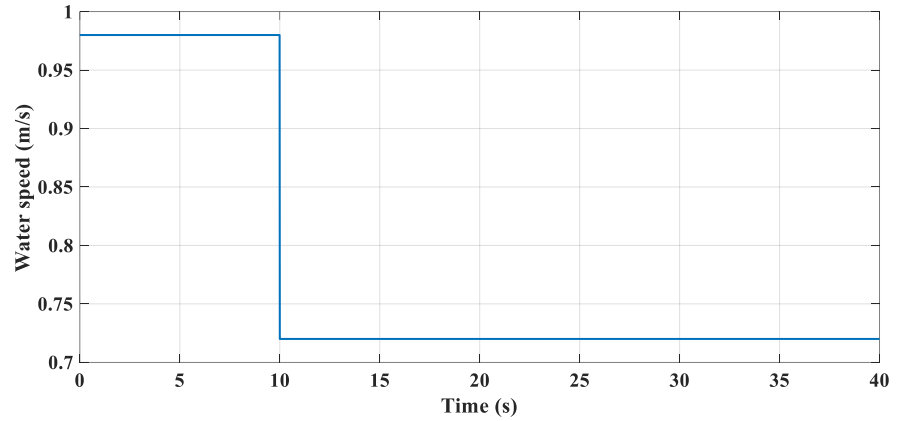

(a)

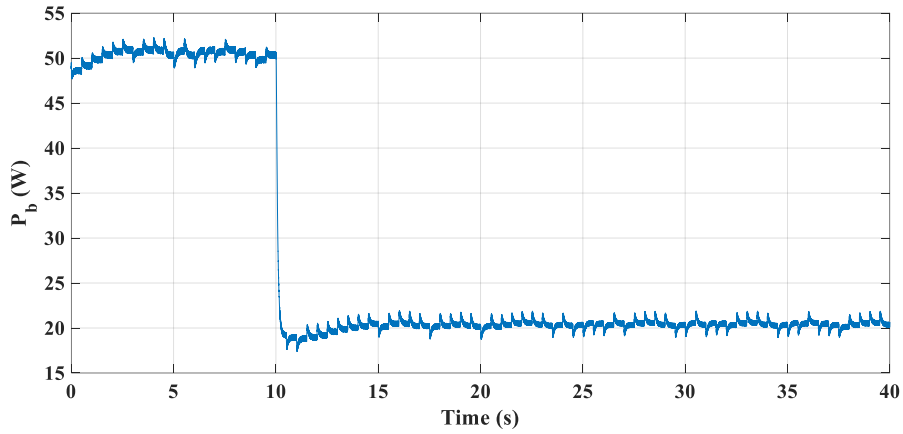

(b)

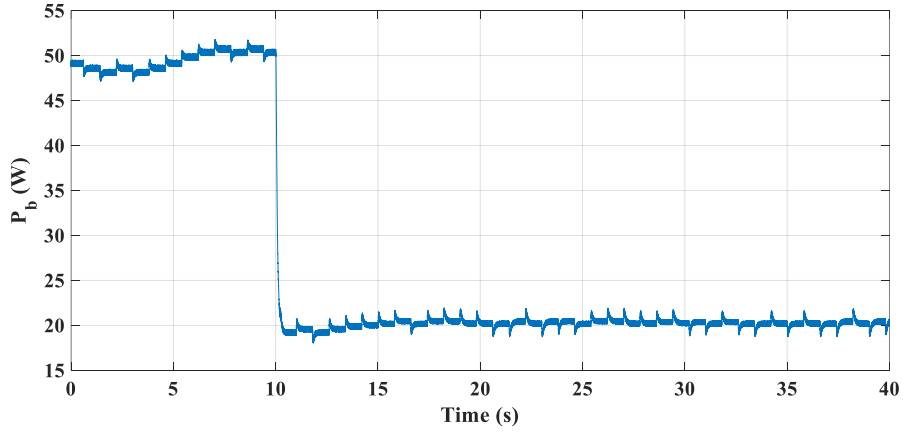

(c)

Figure 5.15. Results from the simulation of the MPPT of the laboratory prototype for a step change in the water speed: (a) water speed, (b) resulting power for $T_s = 0.5s$ and (c) resulting power for $T_s = 0.8s$.

5.4 Experimental validation of the MPPT procedure

The laboratory prototype was used to validate the MPPT control scheme described in Section 5.2.

To validate the estimated value of the inertia of the test system, a step change in the voltage V_{dc} from 36 V to 18 V was applied both in simulation and experimentally. The results are shown in Figure 5.16. It is shown that for the same change in V_{dc}, the time needed for the rotational speed to settle to its new value is approximately the same for both the simulation and the experimental test rig. Steady state oscillations of the rotational speed of the laboratory prototype were observed, due to the 3P oscillations induced by the vertical-axis turbines. This 3P ripple was neglected for the simulation of the laboratory prototype and this is the reason that no oscillation is observed in the simulation results. Consequently, the calculations provided a realistic approximation of the inertia of the laboratory prototype of the hydrokinetic energy conversion system.

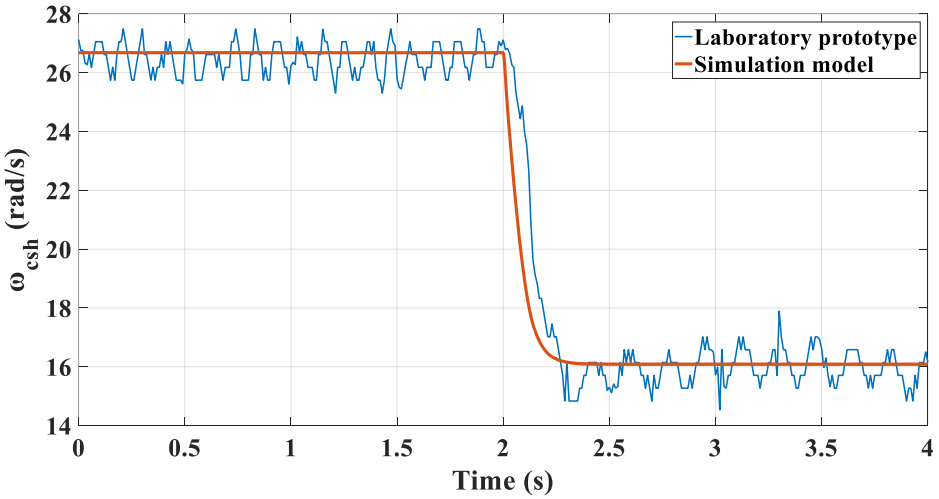

Figure 5.16. The response of the rotational speed of the common shaft for a step change in V_{dc} from 36 to 18 V of the laboratory prototype (blue curve) and of the simulation model (orange curve).

Due to the realistic approximation of the inertia of the hydrokinetic energy conversion system, the sampling time and the convergence speed coefficient selected for the simulation of the MPPT of the laboratory-scale hydrokinetic energy conversion system were used for the experimental validation of the MPPT of the laboratory prototype.

For the experimental procedure, a change in the water speed of the flume was applied from 0.98 to 0.72 m/s similarly to the one shown in Figure 5.10(a). Figure 5.17 shows an oscilloscope screenshot of the power flowing into the batteries. The power was

obtained by measuring the voltage across the terminals of the batteries and the current flowing into the batteries. It is shown that when the change in the water speed took place, the power decreased to a minimum point. Then, it settled and oscillated around a new value due to the new water flow condition.

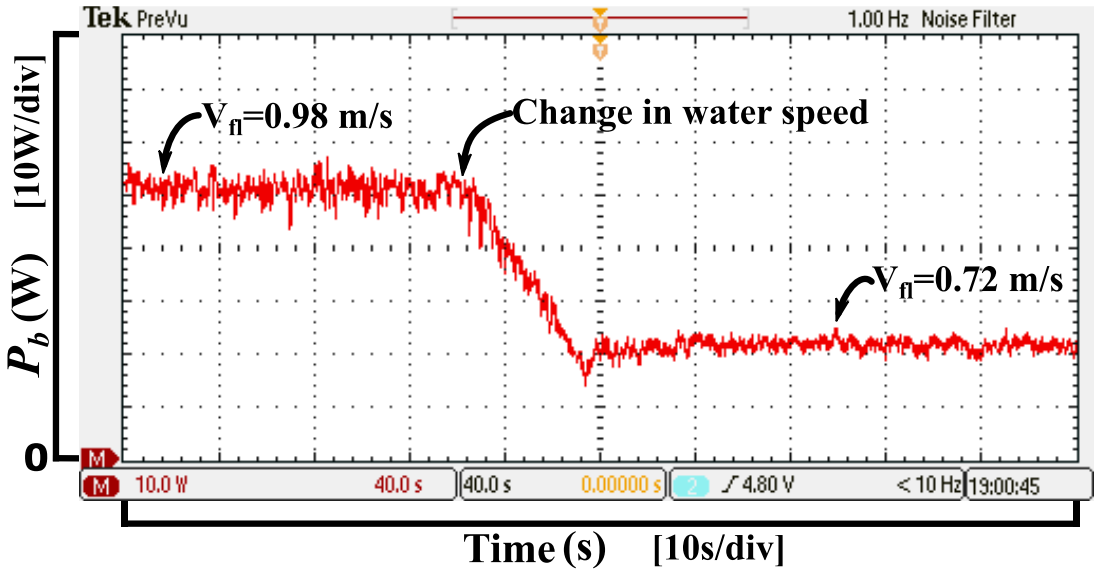

Figure 5.17. MPPT: the power flowing into the batteries for a change in water speed from 0.98 m/s to 0.72 m/s.

To demonstrate the MPPT procedure with respect to the power curves obtained experimentally and shown in Figure 4.36, measurements of the rotational speed were used.

Figure 5.18 shows the experimental results for the MPPT procedure of the laboratory prototype. The red curve is the power curve of the hydrokinetic energy conversion system for a water speed of 0.98 m/s. The blue curve is the power curve of the hydrokinetic energy conversion system for a water speed of 0.72 m/s. These two power curves were taken from the experimental results shown in Figure 4.36. The yellow curve shows the MPPT procedure. The results for the maximum power curve were filtered offline as described in Section 4.4.3.

At first, for a water speed of 0.98 m/s the system was operating around the MPP. When the water speed was decreased to 0.72 m/s, an over-speed occurred. Then the MPP for the new water speed condition was reached and a wider oscillation around the MPP was observed. This is explained by the fact that for a water speed of 0.72 m/s, the ratio

$\frac{dP}{d\omega_{csh}}$ is very small for a wider area of operating points around the new MPP, rather than for a water speed of 0.98 m/s.

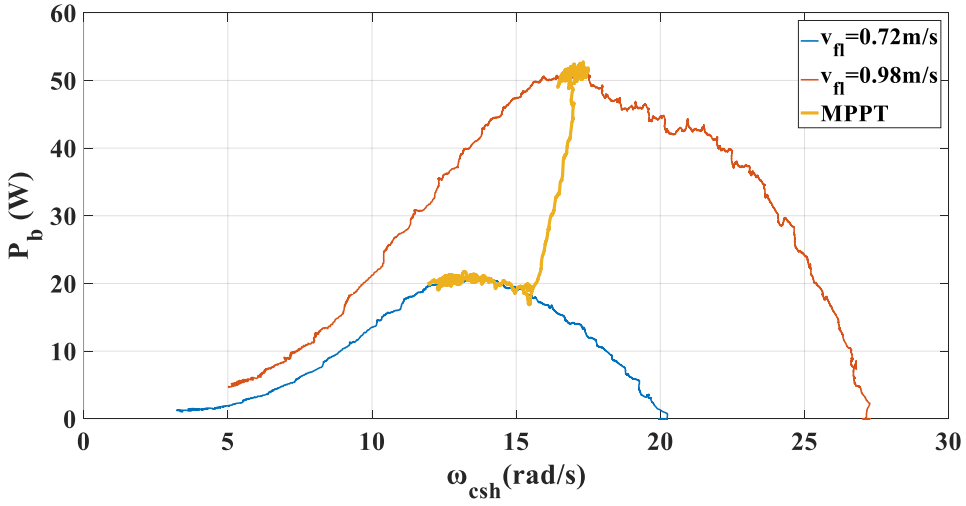

Figure 5.18. Experimental results: MPPT of the laboratory prototype.

Figure 5.11 and Figure 5.18 show that the experimental results were broadly similar to the simulation results. The P&O algorithm was used with the same step change in the perturbation of the voltage and the same sampling time of the algorithm for the simulation of the system and the experimental validation of the MPPT procedure. However, the value of the water speed was obtained in advance, prior to the experimental procedure, as the average speed of several points between the bottom of the flume and the water surface. In addition, because of the manual control of the pump, there was a small time delay between the new set-point of the pump controller and the new water speed. On the contrary, for the simulation of the laboratory prototype of the hydrokinetic energy conversion system, the water speed was assumed to linearly decrease and settle immediately to its new value.

5.5 Simulation of the full-scale hydrokinetic energy conversion system

After the MPPT of the laboratory prototype was tested, a simulation of the full-scale hydrokinetic energy conversion system followed. The anticipated full-scale system is rated at 10 kW. For the simulations, the models described in Chapter 3 were used.

Figure 5.19 shows the configuration of the anticipated full-scale hydrokinetic energy conversion system. Instead of the batteries a VSC is used for the connection to the

grid. The VSC is controlled to fix the voltage V_b, so that the dc-dc converter is used for the control of V_{dc} as in the case of the laboratory prototype.

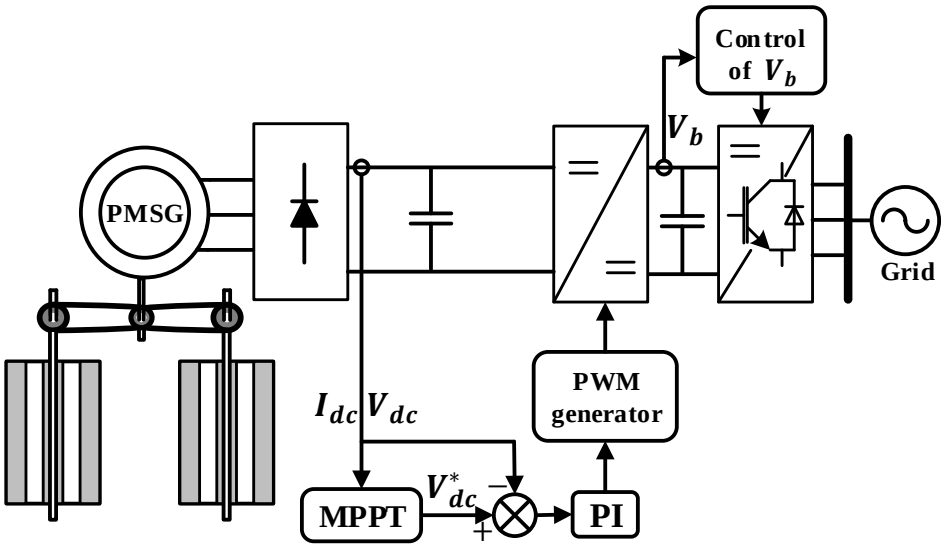

Figure 5.19. Configuration and control scheme for the full scale hydrokinetic energy conversion system.

The turbines used for the full-scale system were of the same type as for the laboratory prototype. To simulate the torque produced by the system of the two turbines, a hydrodynamic model was used. The data for the 10 kW turbine dimensions are given in Appendix B. The data of the $C_p - \lambda$ curve derived experimentally for a water speed of 0.98 m/s were used. It was assumed that this curve was the unique power curve for all the water speeds of the full-scale hydrokinetic energy conversion system.

For the drive-train of the full-scale hydrokinetic energy conversion system, a timing belt was assumed to be used to couple the two turbines with the common shaft, as in the case of the laboratory prototype. Similarly to the modelling of the laboratory prototype, a lumped-mass model was used for the modelling of the drive-train. For the calculation of the inertia, the procedure described in Section 5.3.1 was followed and the inertia of the 10kW system was calculated 9.43 $\text{Kg} \cdot \text{m}^2$.

The generator was assumed to be a PMSG rated at 10 kW, 380 V and 200 rpm. The generator data are given in Appendix B.

For the control of the dc-dc converter new PI gains were tuned and are given in Appendix B. For the control of the grid-side VSC, the control scheme presented in Chapter 3 was used. A phase locked loop was used to measure the frequency of the

grid, an inner loop was used for the control of the current in the *dq* frame and an outer loop is used to control the voltage V_b and fix it at 400V. Details of the grid and the control parameters are give in Appendix B.

At first, a step change in the voltage V_{dc} was applied at 5 s from 380 to 385 V for a constant water speed of 1.8 m/s. The response of the rotational speed of the common shaft is shown in Figure 5.20. For the inertia calculated for the full-scale hydrokinetic energy conversion system (9.43 Kgm^2), a time interval of ≅ 1 s was needed for the new value of the rotational speed to settle.

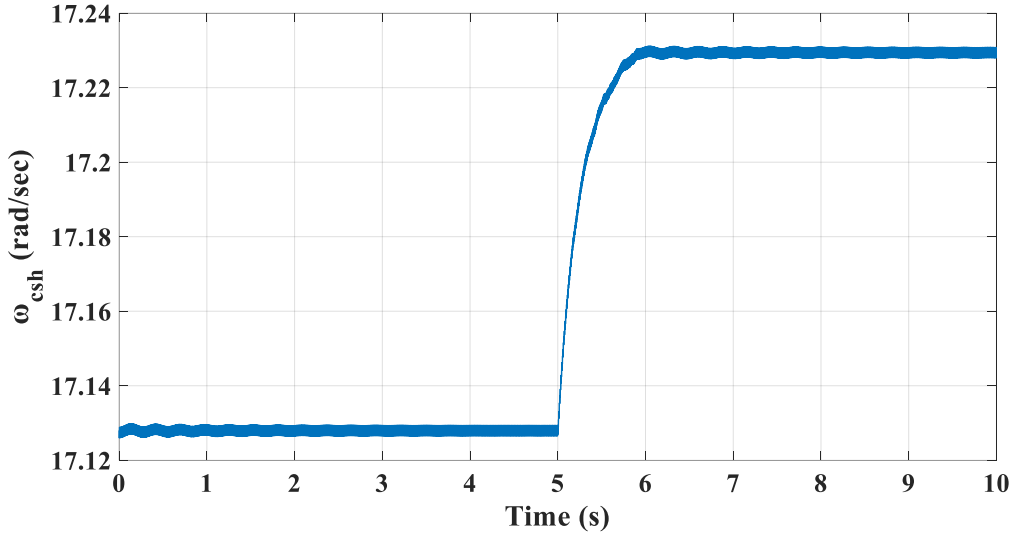

Figure 5.20. Simulation of the full-scale system: response of the rotational speed ω_{csh} for a change of 5 V in V_{dc}.

Due to the higher inertia of the full-scale system than the laboratory prototype, a higher sampling time T_s for the MPPT algorithm was selected. Although the PMSG selected for the full-scale system is rated at 10 kW, its rated speed is the same as the rated speed of the laboratory PMSG rated at 200W. Therefore, the voltage constant of the PMSG of the full-scale system is higher than that of the laboratory prototype, and thus a higher speed coefficient *S* was selected. The sampling time was set to 1 s and the speed coefficient was set to 0.5 V.

For the simulation of the maximum power extraction from the 10 kW system, a change in the water speed from 1.8 to 1.56 m/s was applied, assuming a linear decrease as shown in Figure 5.21(a). The voltage V_b was properly controlled and fixed at 400 V, as shown in Figure 5.21(b). Figure 5.21(c) shows the changes in the voltage V_{dc} during the tracking of the MPP and Figure 5.21(d) shows the changes in the rotational speed

of the generator. Figure 5.21(e) shows the changes in power during the MPPT procedure.

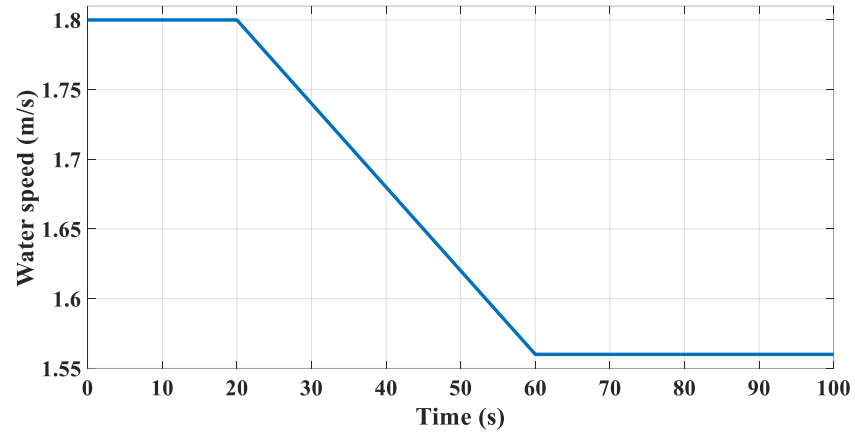

(a)

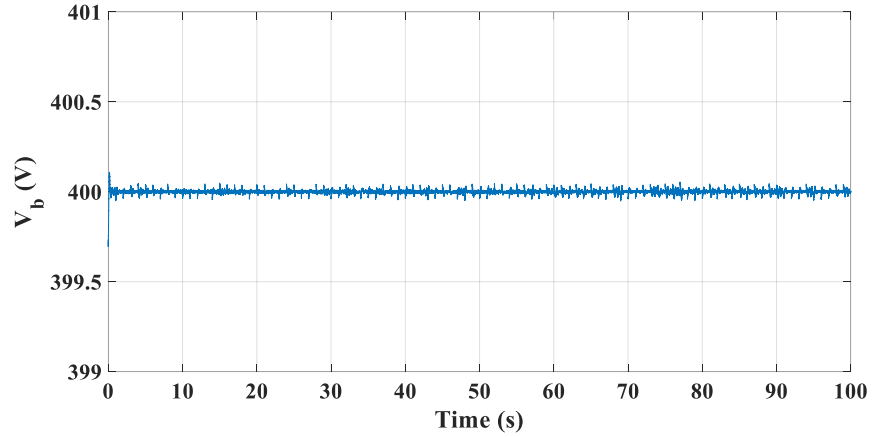

(b)

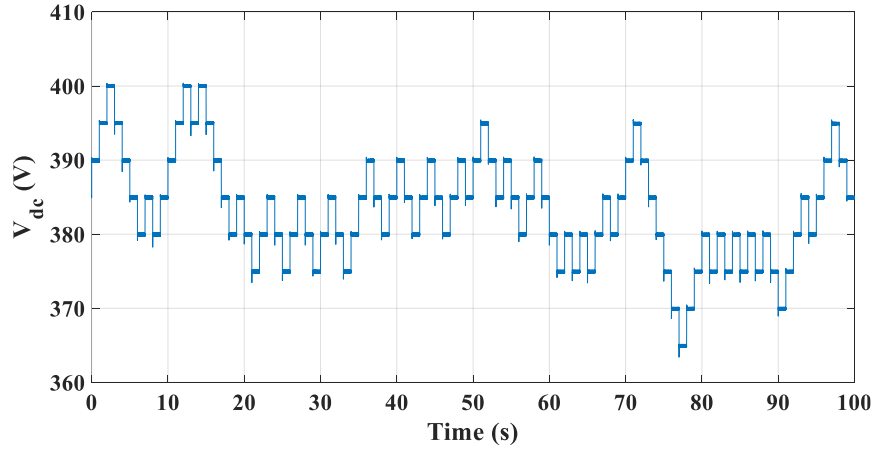

(c)

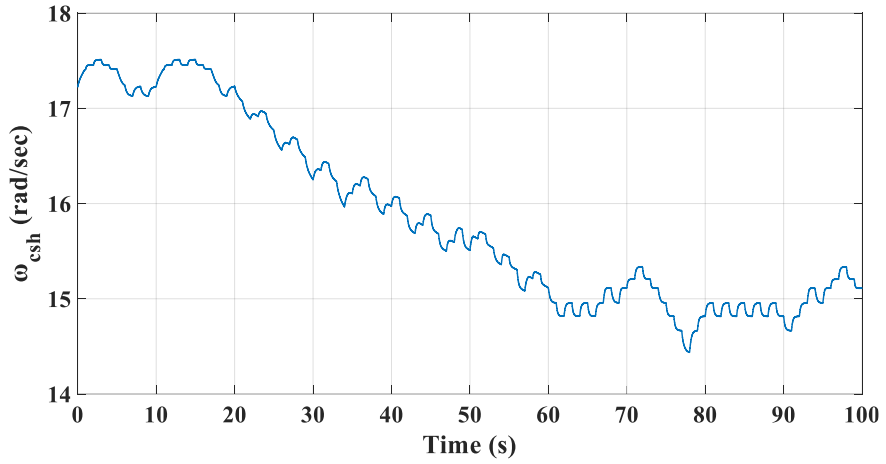

(d)

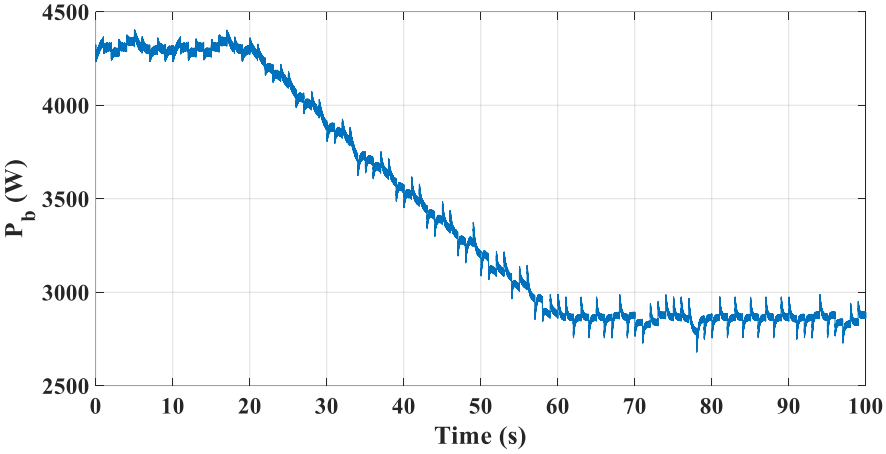

(e)

Figure 5.21. Simulation of the MPPT of the full-scale hydrokinetic energy conversion system: (a) water speed, (b) voltage V_b, (c) voltage V_{dc}, (c) rotational speed of the common shaft, (d) power flowing into the batteries.

The MPPT procedure is shown in Figure 5.22. The blue curve is the power curve of the hydrokinetic energy conversion system for a water speed of 1.56 m/s. The red curve is the power curve of the hydrokinetic energy conversion system for a water speed of 1.8 m/s. The green curve shows the simulation of the tracking procedure. The maximum power was extracted for both water speeds and the tracking of the MPP of the system was maintained after the change in the water speed, as expected.

In real time conditions, the water speed is expected to be changing even slower (several minutes). Therefore, the performance of the MPPT procedure described and used for the laboratory prototype and the simulation of the anticipated full-scale system is expected to be suitable for the final application.

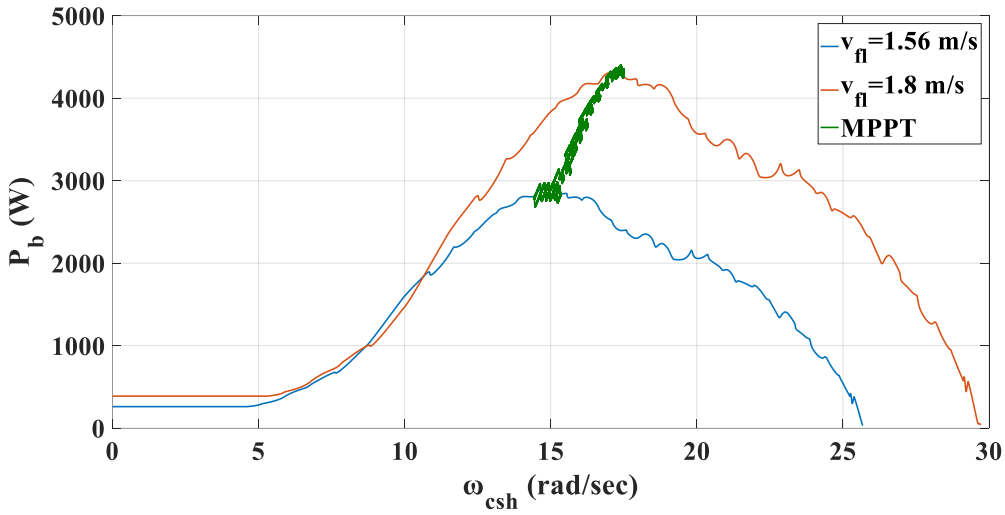

Figure 5.22. Simulation of the MPPT procedure for the full-scale hydrokinetic energy conversion system.

5.6 Summary

A control scheme for the maximum power extraction from the hydrokinetic energy conversion system was designed. The P&O algorithm was used to vary the terminal dc voltage of the generator and observe the resulting power.

The hydrokinetic energy conversion system was modelled and the laboratory prototype was simulated to define the step of the perturbation and the sampling time of the MPPT algorithm. The laboratory prototype was used to validate the simulation results. Both the simulation and the experimental results showed that the maximum power was extracted from the hydrokinetic energy conversion system for a change in the water speed. The system was operating with a small oscillation the MPP for a given water speed. After the water speed was changed, the tracking of the MPP of the system was ensured.

Finally, the full-scale hydrokinetic energy conversion system was modelled and simulated. It was shown that in the case of the full-scale system (higher inertia), more time was needed for the rotational speed of the generator settled to its new value than in the case of the laboratory prototype (lower inertia). Thus, a new step for the change in voltage and a new sample time for the algorithm were used in order to ensure the MPPT of the system.

Chapter 6

Conclusions and Future Work

6.1 Conclusions

Turbine-based energy conversion systems are used to capture the kinetic energy available in renewable energy sources, such as the wind and the water flowing in waterways. Although wind turbines are a mature technology, there are technical challenges associated mainly with their connection to the grid, such as their fault ride-through and inertia response capabilities. On the other hand, hydrokinetic turbines are fairly new and their variable-speed operation is still a technical challenge for their efficient operation. The research work in this thesis investigated the modelling of DIFG and FRC-based variable-speed wind turbines to assess their compliance with Grid Code requirements and the control and MPPT of a hydrokinetic energy conversion system.

6.1.1 Modelling and simulation of wind farms

Modelling and simulation of variable-speed wind turbines is essential for the study of the compliance of wind turbines with the Grid Code requirements. DFIG and FRC PMSG-based wind turbines can be modelled assuming the same aerodynamic and drive-train characteristics. It has been shown that both wind turbine technologies are capable of satisfying the fault ride-through requirements of the Grid Code. However, the impact on the dynamic response of the FRC PMSG-based wind turbine is limited compared to the response of a DFIG-based turbine. This is due to the fact that the power converters fully decouple the wind turbine from the grid.

In addition to the fault ride-through capabilities of the two variable-speed wind turbines, the inertia support capability of FRC-based wind turbines for a drop in the frequency of the grid was investigated. The simulation results show that the wind turbines increase their power output to provide frequency support to the grid, while the dynamic responses remain within acceptable limits. This way, the rate of change of frequency of the grid is limited to a higher value.

The performance of the models for the simulation studies of both wind turbine technologies was good and hence, a similar model was adopted for the simulation of

the variable-speed operation of a turbine-based hydrokinetic energy conversion system.

6.1.2 Control of a hydrokinetic energy conversion system

The electrical subsystem of the laboratory prototype of a hydrokinetic energy conversion system for man-made waterways was designed and developed. Apart from the power take-off capability it offers, it also enables the control and the variable-speed operation of the hydrokinetic energy conversion system. The literature on the electrical interface of hydrokinetic energy conversion systems is limited and consequently knowledge is transferred from the wind industry. The set-up of the power converters of the system is similar to an FRC-based wind turbine. However instead of a controlled rectifier, a diode-bridge and a dc-dc converter are used. Therefore, instead of the torque of the generator, the rectifier voltage is used for the control of the generator.

Experiments were carried out to demonstrate the performance of the laboratory prototype. It has been found that due to the linear relationship between the rectifier voltage and the rotational speed of the generator, the dc-dc converter is suitable for the control and the variable-speed operation of the hydrokinetic energy conversion system.

Another finding is that the use of two identical vertical-axis turbines under restricted flow conditions leads to very high efficiencies. This makes the use of such a system attractive, as the power ratings are small and high efficiencies ensure a profitable operation.

6.1.3 Maximum power extraction from the hydrokinetic energy conversion system

Similarly to wind turbines, the control for the MPPT of the hydrokinetic energy conversion system is essential. This way, the efficiency of the system is maximized and the payback period of the installation costs reduced. Although numerous MPPT techniques are reported in the literature – mainly for wind turbines, the maximum power extraction from the hydrokinetic conversion system is challenging due to the constrained and turbulent water flows.

It has been shown that a simple and effective way to address these challenges is a gradient-based P&O method. This method is based on the perturbation of the rectifier voltage and the observation of the resulting electrical power. However, the implementation of a P&O method comes with technical challenges, such as the selection of the sampling time of the algorithm and the convergence speed coefficient. In addition, the use of vertical-axis turbines induces 3P oscillations and thus, proper filtering is needed so that the performance of the algorithm is good.

Both experimental and simulation results have provided useful information for the control for maximum power extraction. The experimental results show that low-pass filtering is suitable for the mitigation of the 3P oscillations caused by the vertical-axis turbines and the efficient performance of the MPPT algorithm. Simulation results – neglecting the 3P ripples – indicated the dependence of the selection of sampling time of the MPPT algorithm on the inertia of the system. Additionally, the performance of the convergence speed coefficient was directly affected by the voltage constant of the generator used. These findings are particularly important for the future design of heuristic control schemes for the MPPT of similar hydrokinetic energy conversion systems.

6.2 Future work

Following the analysis of simulation and experimental results described in this thesis, a summary of recommended future research objectives is outlined.

6.2.1 Modelling of the 3P ripple of the torque

The use of vertical-axis turbines for a hydrokinetic energy conversion system comes with the presence of 3P oscillations in the torque and the speed of the generator. Consequently, these oscillations are observed in the dc voltage and current. A way to consider this for the design of the MPPT of hydrokinetic energy conversion systems in the future could be the modelling of the 3P ripple of the mechanical torque produced by the vertical-axis turbines. This way, simulation of the MPPT with the use of filters designed for the elimination of the 3P ripple would be possible for systems of any scale.

6.2.2 Design of the control system

In this work, the control of the hydrokinetic energy conversion system was achieved through a dc-dc converter using a conventional PI controller. Future work could focus on further analysis of the system and the design of a robust control system suitable for this hydrokinetic energy conversion system. Measurement uncertainties and delays would be taken into consideration.

6.2.3 Adaptive algorithm for the MPPT

The method for the MPPT of hydrokinetic energy conversion systems described in this thesis is based on a fixed convergence speed coefficient. Future efforts could be made towards the development of an adaptive algorithm to decrease the step size of the perturbations when the system operates closer to the MPP. For the design of the algorithm the turbulent and restricted flow conditions would be taken into account. In addition, the replacement of the diode-bridge rectifier and the dc-dc converter with an IGBT-bridge could be considered for the design of the control scheme for the maximum power extraction.

6.2.4 Connection of hydrokinetic energy conversion systems to the grid

The hydrokinetic energy conversion system described in this thesis is designed for installation in man-made waterways. Thus, several systems are expected to be installed in a certain distance between each other in a canal. Therefore, future work could be conducted on the design of the system for the connection of a number of hydrokinetic energy conversion systems to the grid. The final configuration of the power electronics for the maximum power extraction of each system, the number of the systems connected to an inverter and the impact on the voltage and the power quality of the grid would be considered.

References

[1] "EWEA report on COP21 outcome The Paris agreement," *European Wind Energy Association*, 2015.

[2] https://www.iea.org/weo/ [Accessed June 2018]

[3] https://www.ge.com/renewableenergy/wind-energy/turbines [Accessed June 2018]

[4] http://www.openocean.fr/fr/news/2016/07/26/windturbine-bigger-is-better/ [Accessed June 2018]

[5] M. J. Khan, G. Bhuyan, M. T. Iqbal, and J. E. Quaicoe, "Hydrokinetic energy conversion systems and assessment of horizontal and vertical axis turbines for river and tidal applications: A technology status review," *Applied Energy*, vol. 86, no. 10, pp. 1823–1835, 2009.

[6] http://www.tidalenergy.eu/sea_gen_turbine [Accessed June 2018]

[7] http://www.renewablesfirst.co.uk/hydropower/hydropower-learning-centre/what-is-the-difference-between-micro-mini-and-small-hydro [Accessed June 2018]

[8] T. Burton, D. Sharpe, N. Jenkins, and E. A. Bossanyi, *Wind energy handbook*. John Wiley & Sons, 2011.

[9] James F Manwell, Jon G. McGowan, and Anthony L. Rogers, *Wind energy explained: theory, design and application*. John Wiley & Sons, 2010.

[10] B. Fox, D. Flynn, L. Bryans, N. Jenkins, D. Milborrow, M. O'Malley, R. Watson, and O. Anaya-Lara, 2007. *Wind power integration: connection and system operational aspects. The Institution of Engineering and Technology (IET), London.*

[11] E.A. Bossanyi, 2000. The design of closed loop controllers for wind turbines. *Wind energy*, *3*(3), pp.149-163.

[12] O. Anaya-Lara, N. Jenkins, J. Ekanayake, P. Cartwright, and M. Hughes, *Wind energy generation. Modelling and control.* Hoboken, NJ: Wiley, 2009.

[13] T. Ackermann and L. Söder, "An overview of wind energy-status 2002," Renewable and Sustainable Energy Reviews, vol. 6, no. 1–2, pp. 67–128, 2002.

[14] S. Heier, *Grid integration of Wind Energy Conversion Systems*. Hoboken, NJ: Wiley, 2006.

[15] G.J. Van Bussel, "The science of making more torque from wind: Diffuser experiments and theory revisited", *Journal of Physics: Conference Series* vol. 75, no. 1, 2007.

[16] S. Eriksson, H. Bernhoff, and M. Leijon, "Evaluation of different turbine concepts for wind power", *Renewable and Sustainable Energy Reviews*, vol. 12, no. 5, pp. 1419–1434, 2008.

[17] M. Islam, D. S.–K. Ting, and A. Fartaj, "Aerodynamic models for Darrieus-type straight-bladed vertical axis wind turbines", *Renewable and Sustainable Energy Reviews*, vol. 12, no. 4, pp. 1087–1109, 2008.

[18] Paul Deglaire, "Analytical Aerodynamic Simulation Tools for Vertical Axis Wind Turbines", PhD Thesis, Uppsala University, 2010.

[19] X. Liang, S. Fu, Baoxing Ou, C. Wu, C.Y.H. Chao, K. Pi, "A computational study of the effects of the radius ratio and attachment angle on the performance of a Darrieus-Savonius combined wind turbine," *Renewable Energy*, vol. 113, pp 329-334, 2017.

[20] D. MacPhee and A. Beyene, "Recent Advances in Rotor Design of Vertical Axis Wind Turbines," *Wind Engineering*, vol. 36, no. 6, pp. 647–665, 2012.

[21] R. C. Reuter and M. H. Worstell, "Torque RippIe in a Vertical Axis Wind Turbine,", April 1978. http://citeseerx.ist.psu.edu/viewdoc/download?doi=10.1.1.555.6335&rep=rep1&type=pdf [Accessed June 2018]

[22] O. Ågren, M. Berg, and M. Leijon, "A time-dependent potential flow theory for the aerodynamics of vertical axis wind turbines," *Journal of Applied Physics*, vol. 97, no. 10, 2005.

[23] M. J. Khan, M. T. Iqbal, and J. E. Quaicoe, "River current energy conversion systems: Progress, prospects and challenges," *Renewable and Sustainable Energy Reviews*, vol. 12, no. 8, pp. 2177–2193, 2008.

[24] A. Roberts, B. Thomas, P. Sewell, Z. Khan, S. Balmain, and J. Gillman, "Current tidal power technologies and their suitability for applications in coastal and marine areas," *Journal of Ocean Engineering and Marine Energy*, vol. 2, no. 2, pp. 227–245, 2016.

[25] https://cleantechnica.com/2011/11/14/worlds-largest-tidal-power-array-off-french-coast/ [Accessed: June 2018]

[26] B. Whitby and C. E. Ugalde-Loo, “Performance of pitch and stall regulated tidal stream turbines,” *IEEE Transactions on Sustainable Energy*, vol. 5, no. 1, pp. 64–72, 2014.

[27] http://atlantisresourcesltd.com/turbines/ar-series.html [Accessed: June 2018]

[28] http://www.seageneration.co.uk/ [Accessed: June 2018]

[29] http://voith.com/en/products-services/hydro-power/ocean-energies/tidalcurrent- power-stations-591.html [Accessed: June 2018]

[30] http://www.enerzine.com/7/17093+sabella-implante-la-premiere-hydroliennefrancaise- connectee-au-reseau+.html [Accessed: June 2018]

[31] Z. Zhou, M. Benbouzid, J. F. Charpentier, F. Scuiller, and T. Tang, “Developments in large marine current turbine technologies – A review,”, *Renewable and Sustainable Energy Reviews*, vol. 71, no. December 2016, pp. 852–858, 2017.

[32] Z. Zhou, F. Scuiller, J. F. Charpentier, M. Benbouzid, and T. Tang, “An up-to-date review of large marine tidal current turbine technologies,” *2014 International Power Electronics and Application Conference and Exposition*, Shanghai, 2014, pp. 480–484, 2014.

[33] N. D. Laws and B. P. Epps, “Hydrokinetic energy conversion: Technology, research, and outlook,” *Renewable and Sustainable Energy Reviews*, vol. 57, pp. 1245–1259, 2016.

[34] K. Sornes, “Small-scale Water Current Turbines for River Applications,” *Zero Emission Resource Organisation (ZERO)*, pp. 1–19, 2010

[35] S. Benelghali, M. Benbouzid and J. F. Charpentier, “Turbine Applications Comparison of PMSG and DFIG for Marine Current Turbine Applications,” *The XIX International Conference on Electrical Machines - ICEM 2010,* pp. 1-6, Rome 2010.

[36] J. Zhang, L. Moreau, M. Machmoum, and P. E. Guillerm, “State of the art in tidal current energy extracting technologies,” *2014 First International Conference on Green Energy ICGE 2014*, pp. 1–7, Sfax 2014.

[37] L. Holdsworth, X. G. Wu, J. B. Ekanayake and N. Jenkins, "Comparison of fixed speed and doubly-fed induction wind turbines during power system

disturbances," in *IEE Proceedings - Generation, Transmission and Distribution*, vol. 150, no. 3, pp. 343-352, 13 May 2003.

[38] V. Akhmatov, *Induction generators for wind power*, 2005.

[39] C. E. Ugalde-Loo, J. B. Ekanayake and N. Jenkins, "State-Space Modeling of Wind Turbine Generators for Power System Studies," in *IEEE Transactions on Industry Applications*, vol. 49, no. 1, pp. 223-232, Jan.-Feb. 2013.

[40] R. Pena, J. C. Clare and G. M. Asher, "Doubly fed induction generator using back-to-back PWM converters and its application to variable-speed wind-energy generation," in *IEE Proceedings - Electric Power Applications*, vol. 143, no. 3, pp. 231-241, May 1996.

[41] J. B. Ekanayake, L. Holdsworth, X. Wu and N. Jenkins, "Dynamic modeling of doubly fed induction generator wind turbines," in *IEEE Transactions on Power Systems*, vol. 18, no. 2, pp. 803-809, May 2003.

[42] G. S. Veach, T. J. Lenberg and H. L. Hess, "Wide radius, multi-pole gearless DFIG for in-stream hydroelectric generation," *2017 IEEE International Electric Machines and Drives Conference (IEMDC)*, pp. 1-5, Miami 2017.

[43] M. Liu, W. Li, C. Wang, R. Billinton and J. Yu, "Reliability Evaluation of a Tidal Power Generation System Considering Tidal Current Speeds," in *IEEE Transactions on Power Systems*, vol. 31, no. 4, pp. 3179-3188, July 2016.

[44] M. B. Camara, B. Dakyo, C. Nichita and G. Barakat, "Simulation of a Doubly-Fed Induction Generator with hydro turbine for electrical energy production," *2009 8th International Symposium on Advanced Electromechanical Motion Systems & Electric Drives Joint Symposium*, pp. 1-6, Lille 2009.

[45] Devashish, A. Thakur, S. Panigrahi and R. R. Behera, "A review on wind energy conversion system and enabling technology," *2016 International Conference on Electrical Power and Energy Systems (ICEPES)*, pp. 527-532, Bhopal 2016.

[46] M. A. Vallet, S. Bacha, I. Munteanu, A. I. Bratcu and D. Roye, "Management and Control of Operating Regimes of Cross-Flow Water Turbines," in *IEEE Transactions on Industrial Electronics*, vol. 58, no. 5, pp. 1866-1876, May 2011.

[47] H. Li and Z. Chen, "Overview of different wind generator systems and their comparisons," in *IET Renewable Power Generation*, vol. 2, no. 2, pp. 123-138, June 2008.

[48] L. H. Hansen, L. Helle, F. Blaabjerg, E. Ritchie, H. Bindner, and P. Sørensen, *Conceptual survey of Generators and Power Electronics for Wind Turbines*, December 2001.

[49] Seung-Ho Song, Shin-il Kang and Nyeon-kun Hahm, "Implementation and control of grid connected AC-DC-AC power converter for variable speed wind energy conversion system," *Applied Power Electronics Conference and Exposition, 2003. Eighteenth Annual IEEE*, pp. 154-158 vol.1, Miami Beach, FL, USA, 2003.

[50] M. E. Haque, M. Negnevitsky and K. M. Muttaqi, "A Novel Control Strategy for a Variable-Speed Wind Turbine With a Permanent-Magnet Synchronous Generator," in *IEEE Transactions on Industry Applications*, vol. 46, no. 1, pp. 331-339, Jan.-feb. 2010.

[51] D. Borkowski and T. Węgiel, "Small Hydropower Plant With Integrated Turbine-Generators Working at Variable Speed," in *IEEE Transactions on Energy Conversion*, vol. 28, no. 2, pp. 452-459, June 2013.

[52] K. Tan and S. Islam, "Optimum control strategies in energy conversion of PMSG wind turbine system without mechanical sensors," in *IEEE Transactions on Energy Conversion*, vol. 19, no. 2, pp. 392-399, June 2004.

[53] Q. Wang and L. Chang, "An intelligent maximum power extraction algorithm for inverter-based variable speed wind turbine systems," in *IEEE Transactions on Power Electronics*, vol. 19, no. 5, pp. 1242-1249, Sept. 2004.

[54] N. Mohan, T. Undeland and W. Robbins, *Power Electronics Converters, Application and Design*, J. Wiley & sons, 2003.

[55] R. Ericksson and D. Maksimovic, *Fundamentals of Power Electronics*. Springer Science & Business Media, 2007.

[56] E. Rogers and System Power, "Understanding Buck Power Stages in Switchmode Power Supplies Application Report,"p. 36, 1999. Available at: http://citeseerx.ist.psu.edu/viewdoc/download?doi=10.1.1.202.3288&rep=rep1&type=pdf [Accessed: June 2018]

[57] Huai Wei and I. Batarseh, "Comparison of basic converter topologies for power factor correction," *Southeastcon '98. Proceedings. IEEE*, Orlando, FL, 1998, pp. 348-353.

[58] D. Jovcic and K. Ahmed, *High voltage direct current transmission: converters, systems and DC grids.* John Wiley & Sons, 2015.

[59] D. Van Hertem, O. Gomis-Bellmunt, and J. Liang, *HVDC grids: for offshore and supergrid of the future*. John Wiley & Sons., 2016.

[60] J. Licari, "Control of a Variable-Speed Wind Turbine", Cardiff University, 2013.

[61] B. Whitby, "Control of an Axial Flow Tidal Stream Turbine" PhD Thesis, Cardiff University, 2013.

[62] R. C. Portillo *et al.*, "Modeling Strategy for Back-to-Back Three-Level Converters Applied to High-Power Wind Turbines," in *IEEE Transactions on Industrial Electronics*, vol. 53, no. 5, pp. 1483-1491, Oct. 2006.

[63] P. Hill, "Siemens Debuts HVDC PLUS with San Francisco's Trans Bay Cable", July 2011.https://www.energy.siemens.com/hq/pool/hq/energy-topics/publications/living-energy/pdf/issue-05/Living-Energy-5-HVDC-San-Francisco-Trans-Bay-Cable.pdf [Accessed: June 2018]

[64] D. Das, J. Pan and S. Bala, "HVDC Light for large offshore wind farm integration," *2012 IEEE Power Electronics and Machines in Wind Applications*, pp. 1-7, Denver, CO, 2012.

[65] J. Khan, T. Iqbal and J. Quaicoe, "Power tracking control challenges in Hydrokinetic energy conversion systems," *2011 IEEE Power and Energy Society General Meeting*, pp. 1-6 San Diego, CA, 2011.

[66] M. J. Khan, M. T. Iqbal and J. E. Quaicoe, "Effects of nonlinear efficiency characteristics on the power-tracking control: a case study of hydrokinetic energy conversion system," *2009 IEEE Energy Conversion Congress and Exposition*, pp. 2657-2666, San Jose, CA, 2009.

[67] M. A. Abdullah, A. H. M. Yatim, C. W. Tan, and R. Saidur, "A review of maximum power point tracking algorithms for wind energy systems," *Renewable and Sustainable Energy Reviews*, vol. 16, no. 5, pp. 3220–3227, 2012.

[68] M. Chinchilla, S. Arnaltes and J. C. Burgos, "Control of permanent-magnet generators applied to variable-speed wind-energy systems connected to the grid," in *IEEE Transactions on Energy Conversion*, vol. 21, no. 1, pp. 130-135, March 2006.

[69] A. Tapia, G. Tapia, J. X. Ostolaza and J. R. Saenz, "Modeling and control of a wind turbine driven doubly fed induction generator," in *IEEE Transactions on Energy Conversion*, vol. 18, no. 2, pp. 194-204, June 2003.

[70] B. Shen, B. Mwinyiwiwa, Y. Zhang and B. T. Ooi, "Sensorless Maximum Power Point Tracking of Wind by DFIG Using Rotor Position Phase Lock Loop (PLL)," in *IEEE Transactions on Power Electronics*, vol. 24, no. 4, pp. 942-951, April 2009.

[71] S. M. R. Kazmi, H. Goto, H. J. Guo and O. Ichinokura, "Review and critical analysis of the research papers published till date on maximum power point tracking in wind energy conversion system," *2010 IEEE Energy Conversion Congress and Exposition*, pp. 4075-4082, Atlanta, GA, 2010.

[72] Z. Zhou, F. Scuiller, J. F. Charpentier, M. E. H. Benbouzid and T. Tang, "Power Smoothing Control in a Grid-Connected Marine Current Turbine System for Compensating Swell Effect," in *IEEE Transactions on Sustainable Energy*, vol. 4, no. 3, pp. 816-826, July 2013.

[73] S. M. R. Kazmi, H. Goto, H. J. Guo and O. Ichinokura, "A Novel Algorithm for Fast and Efficient Speed-Sensorless Maximum Power Point Tracking in Wind Energy Conversion Systems," in *IEEE Transactions on Industrial Electronics*, vol. 58, no. 1, pp. 29-36, Jan. 2011.

[74] A. Mirecki, X. Roboam and F. Richardeau, "Architecture Complexity and Energy Efficiency of Small Wind Turbines," in *IEEE Transactions on Industrial Electronics*, vol. 54, no. 1, pp. 660-670, Feb. 2007.

[75] C. N. Bhende, S. Mishra and S. G. Malla, "Permanent Magnet Synchronous Generator-Based Standalone Wind Energy Supply System," in *IEEE Transactions on Sustainable Energy*, vol. 2, no. 4, pp. 361-373, Oct. 2011.

[76] Y. Daili, J.-P. Gaubert, and L. Rahmani, “New control strategy for fast-efficient maximum power point tracking without mechanical sensors applied to small wind energy conversion system,” *Journal of Renewable and Sustainable Energy*, vol. 7, no. 4, p. 43102, 2015.

[77] M. Hauck, A. Rumeau, A. I. Bratcu, S. Bacha, I. Munteanu and d. roye, "Identification and control of a river-current-turbine generator — application to a full-scale prototype," in *IEEE Transactions on Sustainable Energy*, vol. 3029, pp. 1–10, 2017.

[78] E. Koutroulis and K. Kalaitzakis, "Design of a maximum power tracking system for wind-energy-conversion applications," in *IEEE Transactions on Industrial Electronics*, vol. 53, no. 2, pp. 486-494, April 2006.

[79] K. Amei, Y. Takayasu, T. Ohji and M. Sakui, "A maximum power control of wind generator system using a permanent magnet synchronous generator and a boost chopper circuit," *Proceedings of the Power Conversion Conference-Osaka 2002 (Cat. No.02TH8579)*, pp. 1447-1452, vol.3, Osaka, 2002

[80] R. I. Putri, M. Pujiantara, A. Priyadi, T. Ise and M. H. Purnomo, "Maximum power extraction improvement using sensorless controller based on adaptive perturb and observe algorithm for PMSG wind turbine application," in *IET Electric Power Applications*, vol. 12, no. 4, pp. 455-462, 4 2018.

[81] Z. M. Dalala, Z. U. Zahid, W. Yu, Y. Cho and J. S. (. Lai, "Design and Analysis of an MPPT Technique for Small-Scale Wind Energy Conversion Systems," in *IEEE Transactions on Energy Conversion*, vol. 28, no. 3, pp. 756-767, Sept. 2013.

[82] Y. Xia, K. H. Ahmed and B. W. Williams, "A New Maximum Power Point Tracking Technique for Permanent Magnet Synchronous Generator Based Wind Energy Conversion System," in *IEEE Transactions on Power Electronics*, vol. 26, no. 12, pp. 3609-3620, Dec. 2011.

[83] V. Agarwal, R. K. Aggarwal, P. Patidar and C. Patki, "A Novel Scheme for Rapid Tracking of Maximum Power Point in Wind Energy Generation Systems," in *IEEE Transactions on Energy Conversion*, vol. 25, no. 1, pp. 228-236, March 2010.

[84] D. W. Choi, S. I. Byun and Y. H. Cho, "A Study on the Maximum Power Control Method of Switched Reluctance Generator for Wind Turbine," in *IEEE Transactions on Magnetics*, vol. 50, no. 1, pp. 1-4, Jan. 2014.

[85] J. Hussain and M. K. Mishra, "Adaptive Maximum Power Point Tracking Control Algorithm for Wind Energy Conversion Systems," in *IEEE Transactions on Energy Conversion*, vol. 31, no. 2, pp. 697-705, June 2016.

[86] J. C. Y. Hui, A. Bakhshai and P. K. Jain, "A Sensorless Adaptive Maximum Power Point Extraction Method With Voltage Feedback Control for Small Wind Turbines in Off-Grid Applications," in *IEEE Journal of Emerging and Selected Topics in Power Electronics*, vol. 3, no. 3, pp. 817-828, Sept. 2015.

[87] A. Z. Mohamed, M. N. Eskander and F. A. Ghali, "Fuzzy logic control based maximum power tracking of a wind energy system," *Renewable Energy*, vol. 23, no. 2, pp. 235–245, 2001.

[88] Hui Li, K. L. Shi and P. G. McLaren, "Neural-network-based sensorless maximum wind energy capture with compensated power coefficient," in *IEEE Transactions on Industry Applications*, vol. 41, no. 6, pp. 1548-1556, Nov.-Dec. 2005.

[89] Anees, Ahmed Sharique. "Grid integration of renewable energy sources: Challenges, issues and possible solutions." In *Power Electronics (IICPE), 2012 IEEE 5th India International Conference on*, pp. 1-6. IEEE, 2012.

[90] National Grid, 'Future Energy Scenarios', 2015

[91] National Grid, 'The Grid Code', Rev 14, vol 14, no 5, 2015

[92] 'Local authority CO2 emissions estimates 2006, Stat. Summ., 2018

[93] I. A. Erinmez, D. O. Bickers, G. F. Wood and W. W. Hung, "NGC experience with frequency control in England and Wales-provision of frequency response by generators," *IEEE Power Engineering Society. 1999 Winter Meeting (Cat. No.99CH36233)*, New York, NY, 1999, pp. 590-596 vol.1.

[94] J. Licari, C. E. Ugalde-Loo, J. B. Ekanayake and N. Jenkins, "Damping of Torsional Vibrations in a Variable-Speed Wind Turbine," in *IEEE Transactions on Energy Conversion*, vol. 28, no. 1, pp. 172-180, March 2013.

[95] R. Krishnan. *Permanent magnet synchronous and brushless DC motor drives*. CRC press, 2009.

[96] C. E. Ugalde-Loo, L. A. Amézquita-Brooks, E. Licéaga-Castro and J. Licéaga-Castro, "Analysis and efficient control design for generator-side converters of PMSG-based wind and tidal stream turbines," *2014 Power Systems Computation Conference*, Wroclaw, 2014, pp. 1-7.

[97] John Licari, Carlos E. Ugalde-Loo, Jun Liang, Janaka Ekanayake, and Nick Jenkins. "Torsional damping considering both shaft and blade flexibilities." *Wind Engineering* 36, no. 2 (2012): 181-195.

[98] G. Ramtharan, J. B. Ekanayake and N. Jenkins, "Frequency support from doubly fed induction generator wind turbines," in *IET Renewable Power Generation*, vol. 1, no. 1, pp. 3-9, March 2007.

[99] J. F. Conroy and R. Watson, "Frequency Response Capability of Full Converter Wind Turbine Generators in Comparison to Conventional Generation," in *IEEE Transactions on Power Systems*, vol. 23, no. 2, pp. 649-656, May 2008.

[100] M. Kayikci and J. V. Milanovic, "Dynamic Contribution of DFIG-Based Wind Plants to System Frequency Disturbances," in *IEEE Transactions on Power Systems*, vol. 24, no. 2, pp. 859-867, May 2009.

[101] N. R. Ullah, T. Thiringer and D. Karlsson, "Temporary Primary Frequency Control Support by Variable Speed Wind Turbines— Potential and Applications," in *IEEE Transactions on Power Systems*, vol. 23, no. 2, pp. 601-612, May 2008.

[102] V. F. Mendes, C. V. de Sousa, S. R. Silva, B. C. Rabelo, Jr., and W. Hofmann, "Modeling and Ride-Through Control of Doubly Fed Induction Generators During Symmetrical Voltage Sags," *IEEE Transactions on. Energy Conversion*, vol. 26, no. 4, pp. 1161–1171, 2011.

[103] G. Pannell, D. J. Atkinson, and B. Zahawi, "Analytical study of grid-fault response of wind turbine doubly fed induction generator," *IEEE Transactions on Energy Conversion*, vol. 25, no. 4, pp. 1081–1091, 2010.

[104] J. Morren and S. W. H. de Haan, "Ridethrough of wind turbines with doubly-fed induction generator during a voltage dip," *IEEE Transactions on Energy Conversion*, vol. 20, no. 2, pp. 435–441, 2005.

[105] M. E. Elshiekh, D. A. Mansour, and A. M. Azmy, "Improving Fault Ride-Through Capability of DFIG-Based Wind Turbine Using Superconducting Fault Current Limiter," *IEEE Transactions on Applied Superconductivity*, vol. 23, no. 3, pp. 5601204–5601204, 2013.

[106] L. Chen, C. Deng, F. Zheng, S. Li, Y. Liu, and Y. Liao, "Fault ride-through capability enhancement of DFIG-based wind turbine with a flux-coupling-type SFCL employed at different locations," *IEEE Transactions on Applied Superconductivity*, vol. 25, no. 3, 2015.

[107] A. M. S. Yunus, M. A. S. Masoum, and A. Abu-Siada, “Application of SMES to enhance the dynamic performance of DFIG during voltage sag and swell,” *IEEE Transactions on Applied Superconductivity*, vol. 22, no. 4, 2012.

[108] Y. Mu, J. Wu, J. Ekanayake, N. Jenkins and H. Jia, "Primary Frequency Response From Electric Vehicles in the Great Britain Power System," in *IEEE Transactions on Smart Grid*, vol. 4, no. 2, pp. 1142-1150, June 2013.

[109] J. Ekanayake, N. Jenkins, and G. Strbac. ‘Frequency response from wind turbines.’ *Wind Engineering* 32, no. 6, 2008, 573-586.

[110] M. Sander, G. van Kuik, and G. J. W. Van Bussel, “Performance of an H-Darrieus in the skewed flow on a roof,” *Journal of Solar Energy Engineering*, vol. 4, pp. 433–440, 2003.

[111] https://labjack.com/products/u6 [Accessed June 2018]

[112] H. Wu, V. Pickert, D. Giaouris and B. Ji, "Nonlinear Analysis and Control of Interleaved Boost Converter Using Real-Time Cycle to Cycle Variable Slope Compensation," in *IEEE Transactions on Power Electronics*, vol. 32, no. 9, pp. 7256-7270, Sept. 2017.

[113] http://www.ti.com/lit/ug/tidu404/tidu404.pdf [Accessed June 2018]

[114] J. Grainger, and William D. Stevenson. *Power system analysis*. Vol. 621. New York: McGraw-Hill, 1994.

[115] Richard C. Dorf and Robert H. Bishop. *Modern control systems*. Pearson, 2011.

[116] A. Betz, *Wind-energie und ihre ausnutzung durch windmühlen*. Vandenhoeck, 1926.

[117] A. M. Knight and G. E. Peters, "Simple wind energy controller for an expanded operating range," in *IEEE Transactions on Energy Conversion*, vol. 20, no. 2, pp. 459-466, June 2005.

[118] S. M. Muyeen, Junji Tamura, and Toshiaki Murata. *Stability augmentation of a grid-connected wind farm*. Springer Science & Business Media, 2008.

[119] https://uk.mathworks.com/help/physmod/sps/powersys/ref/power_pmsynchronousmachineparams.html [Accessed June 2018]

Appendix A

Parameters of DFIG and PMSG-based wind turbines

Table A-1: Parameters for the modelling of DFIG and PMSG-based wind turbines.

Wind turbine		*Three-mass model*	
Rated power	2 MW	J_1	2.227×10^6 kg·m^2
Rated speed	18 r/min	J_2	3.801×10^6 kg·m^2
Rotor diameter	40 m	J_3	416633 kg·m^2
Number of blades	3	K_1	573.18×10^6 N·m/rad
DFIG		K_2	1.6×10^8 N·m/rad
V_b	690 V	D_1	0
S_b	2 MVA	D_2	0
f_b	50 Hz	N	83.33
ω_b	50 Hz	*PMSG*	
$\overline{R}_s$	0.00488 pu	Poles	4
$\overline{R}_r$	0.00549 pu	f	50 Hz
$\overline{R}_d$	0.2696 pu	R_s	4.523 mΩ
$\overline{X}_{tr}$	0.05 pu	L_d, L_q	322 Mh
$\overline{X}_{ls}$	0.09241 pu	*Converters*	
$\overline{X}_{lr}$	0.09955 pu	DC link capacitor	90,000 µF
$\overline{X}_{ld}$	0.0453 pu	V_{dc}	1400 V
$\overline{X}_m$	3.95279 pu	f_s	3 kHz
$\overline{X}_{rm}$	0.02 pu	*Grid*	
DFIG rotor side controller		V_{LL}	690 V
K_{p1}, K_{p2}	0.02	L_g	500 µH
K_{i1}, K_{i2}	10	R_g	0.4 mΩ
Inertia controller		*PMSG machine side controller*	
K_1	5000	K_{p1}, K_{p2}	0.476
K_2	3000	K_{i1}, K_{i2}	280

Appendix B

Parameters of the hydrokinetic energy conversion system

Table B-1: Parameters for the modelling and experimental validation of the hydrokinetic energy conversion system.

Variable	Experimental prototype	Prototype simulation	Full-scale system simulation
T_s (s)	0.5 s	0.5 s	1 s
S (V)	0.2 V	0.2 V	5 V
K_p	0.01	0.2	1
K_i	100	40	100
T_c (s)	0.45 s	–	–
DC-dc converter switching frequency (kHz)	100	100	100
Estimated inertia (kg·m^2)	–	0.0876	9.43
V_{dc}/k_{rpm} f	190	190	3460
Number of poles	16	16	24
PMSG rated power of PMSG (kW)	0.2	0.2	10
Rated speed of PMSG (rpm)	200	200	200
R_{L-L}@20℃ (Ω)	0.8	0.8	3.53
L_{L-L}@20℃ (mH)	7.4	7.4	78.2
Batteries (V)	12	12	–
Grid	–	–	$V_{L-L,rms} = 200$ V, $f_g = 50$Hz
Turbine dimensions	0.3x0.18 m	0.3x0.18 m	0.8x1.36 m
Gearing ratio	4:3	4:3	3:1
Volume of the blade (mm^3)	271064.5	271064.5	3391389
Density of the blade (g/cm^3)	0.93	0.93	2.7
Mass of the blade (kg)	0.287	0.287	17.3

Appendix C

Design of the low-pass filter

The range of the rotational speed of the common shaft is: **10 – 25 ras/s**

Taking into account the gearing ratio, the range of the rotational speed of the each turbine is: **7.5–18.75 rad/s**

Thus, the range of the rotational frequency of each turbine is: **1.19–2.98 Hz**

The range of oscillations of the speed/torque **(3P)** is: **3.57–8.94 Hz**

A low-pass filter is needed to "cut" the frequencies above 3.57 Hz. Thus, a cutoff frequency of 0.35 Hz is chosen.

$$f_c = 0.357\text{Hz} \rightarrow \omega_c = 2.243\frac{\text{rad}}{\text{s}} \rightarrow \tau_c = \frac{1}{\omega_c} = 0.45\text{s}$$

Therefore, the transfer function of the filter is $G(s) = \frac{1}{1+0.45s}$

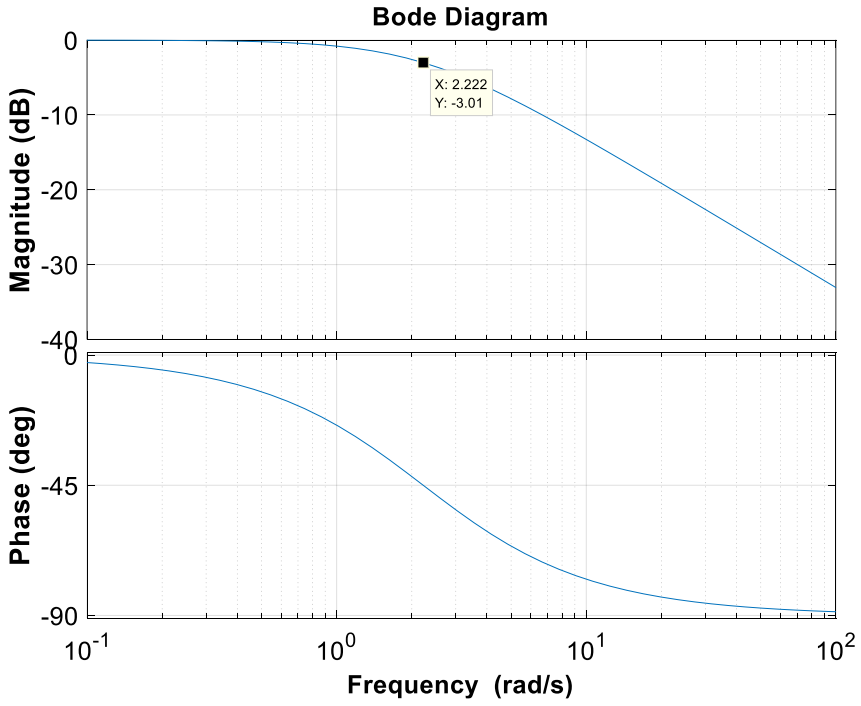

Figure C.1. Bode diagram of the transfer function of the low-pass filter

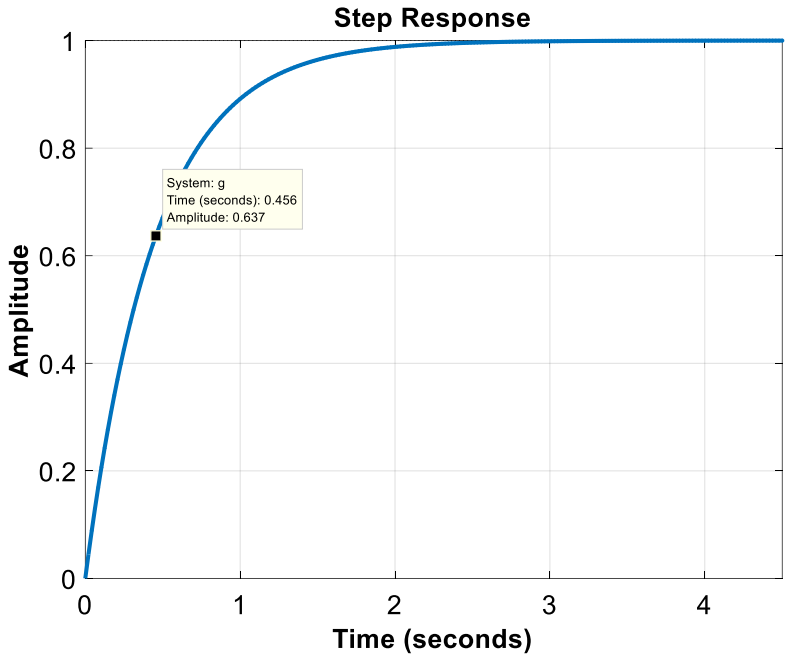

Figure C.2. Step response of the transfer function of the low-pass filter

Appendix D

Diagram of the dc-dc converter used for the experiments

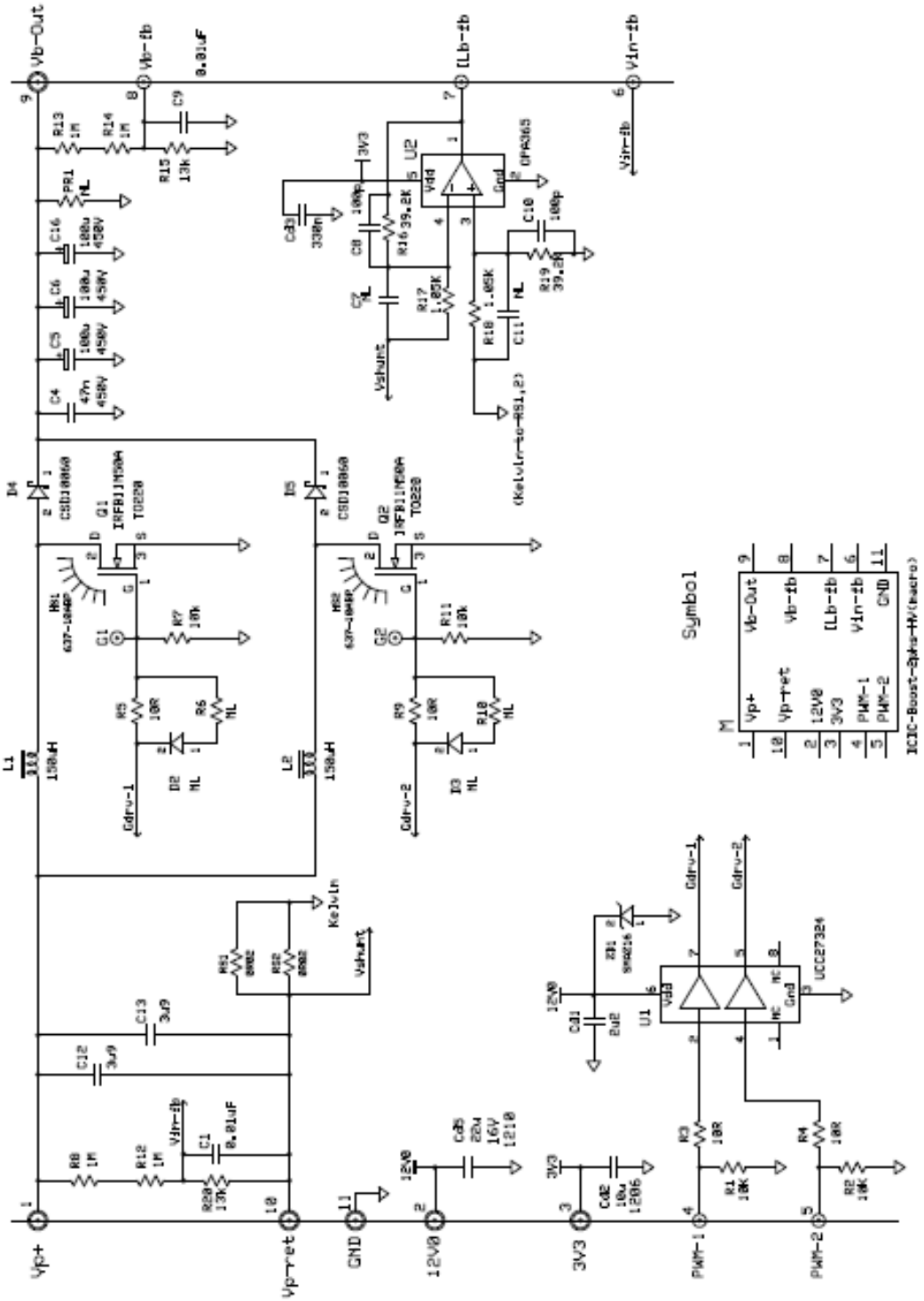

Figure D.1. Diagram and specifications of the dc-dc converter purchased for the experimental procedure.

Appendix E

Park's transformation

In this section, Park's transformation is applied to the stator variables of a synchronous machine.

$$\boldsymbol{v}_p = P\boldsymbol{v}_T$$

$$\boldsymbol{\psi}_p = P\boldsymbol{\psi}_T$$

$$\boldsymbol{i}_p = P\boldsymbol{i}_T$$

Where

$$P = \sqrt{\frac{2}{3}}\begin{bmatrix} \cos\theta_e & \cos(\theta_e - \frac{2\pi}{3}) & \cos(\theta_e + \frac{2\pi}{3}) \\ \sin\theta_e & \sin\left(\theta_e - \frac{2\pi}{3}\right) & \sin\left(\theta_e + \frac{2\pi}{3}\right) \\ \sqrt{\frac{1}{2}} & \sqrt{\frac{1}{2}} & \sqrt{\frac{1}{2}} \end{bmatrix}$$

And

$$\theta_e = n_{pp}\theta_r$$

where θ_r is the rotor angle (rad).

$$\boldsymbol{v}_p = \begin{bmatrix} v_d & v_q & v_0 \end{bmatrix}^T$$

$$\boldsymbol{\psi}_p = \begin{bmatrix} \psi_d & \psi_q & \psi_0 \end{bmatrix}^T$$

$$\boldsymbol{i}_p = \begin{bmatrix} i_d & i_q & i_0 \end{bmatrix}^T$$